

Electron Paramagnetic Resonance of Process-Induced Defects in Silicon

VOM FACHBEREICH PHYSIK DER UNIVERSITÄT PADERBORN
ZUR ERLANGUNG DES AKADEMISCHEN GRADES EINES
DOKTORS DER NATURWISSENSCHAFTEN
(DR. RER. NAT.)
GENEHMIGTE DISSERTATION

VON

BERTRAM LANGHANKI

1. GUTACHTER: PROF. DR. J.-M. SPAETH
2. GUTACHTER: PROF. DR. H. OVERHOF

TAG DER EINREICHUNG: 08.02.2001
TAG DER MÜNDLICHEN PRÜFUNG: 21.03.2001

Table of Contents

Introduction	1
1 Fundamentals of the measurement techniques	3
1.1 Theoretical fundamentals of EPR and ENDOR	3
1.1.1 The spin Hamiltonian	4
1.1.2 Analysis of EPR spectra	6
1.1.3 Analysis of ENDOR spectra.....	7
1.2 Experimental measurement method and setup for EPR and ENDOR.....	7
1.3 Electrically Detected EPR	11
1.3.1 On the mechanisms of EDEPR	11
1.3.2 Experimental setup for EDEPR	16
1.4 Fourier Transform Infrared Absorption (FTIR)	17
2 Advances in EDEPR technology	21
2.1 EDEPR with microwave power modulation	21
2.2 EDEPR with high microwave frequencies	26
3 EDEPR investigation of implanted and heat-treated silicon	31
3.1 Motivation for Mo-implantation into silicon samples.....	32
3.2 EPR of Mo-implanted and annealed FZ-silicon	33
3.3 EDEPR of Mo- and Si-implanted and annealed FZ-silicon	34

4	Oxygen related defects in silicon	47
4.1	Oxygen in silicon – an introduction	48
4.2	Thermal Double Donors.....	49
4.3	Shallow Thermal Donors	53
4.4	Radiation defects with participation of oxygen	54
5	Magnetical and optical studies of shallow thermal donors in hydrogenated Cz-Si crystals	57
5.1	Introduction.....	58
5.2	Electronic properties of the shallow donors D1–D3.....	60
5.3	EPR investigation of the shallow donors D1–D3	64
5.4	EDEPR investigation of the shallow donor D2	69
5.5	EPR investigation of shallow donor interaction with ^{29}Si nuclei	71
5.6	ENDOR investigation of the shallow donors D1 and D2	75
5.7	Discussion	82
5.8	Conclusions	91
6	On the mechanism of EDEPR	93
6.1	Investigation of Cz-silicon after heat-treatment at 470°C	93
6.1.1	Preparation and FTIR-characterisation of TDD	94
6.1.2	EDEPR of Cz-Si heat treated at 470°C	96
6.2	Presentation of further EDEPR experiments	98
6.3	On the impact of electron-irradiation on the EDEPR signal.....	100
6.4	On the mechanism responsible for the EDEPR detection of P_{ba} and P_{bb}	105
6.5	Peculiarities of EDEPR	107
6.6	Conclusions	108
Summary		111
References		115

Introduction

In this work the class of Si/SiO₂ interface defects is studied with the method of Electrically Detected Electron-Paramagnetic Resonance (EDEPR). The interface defects, called “dangling bond” defects or P_b-centres, are subject of considerable scientific as well as technological interest. Their importance is easily explained regarding the interface formation during oxidation processes and the improvement of metal-oxide semiconductor (MOS) devices. Since semiconductor devices are fabricated with Very Large Scale Integration (VLSI), the impact of surface and interface defects on the device performance has increased significantly. The EDEPR investigation of (100)-oriented Si/SiO₂ interfaces reveals an unknown dangling bond centre at the interface and yields the precise symmetry of a further P_b-centre below the interface.

In the realm of state-of-the art semiconductor device production, annealing procedures have to be carried out especially after implantation of doping elements. Since oxygen is the dominant contamination in silicon crystals grown by the Czochralski(Cz)-method, which is used for the majority of semiconductor devices, the annealing procedures cause the growth of oxygen precipitates. The defect centres are most efficiently created at temperatures around (300–500)°C and are called Thermal Donors (TD) in general. Several subsets of TDs with similar features are known, each subset consisting of certain number of species which form subsequently upon annealing. The shallow donor character of the TDs is responsible for severe changes in the conductivity of the silicon crystals, which explains the technological interest in the formation of these defects. Apart from the economic aspect the scientific interest has remained high over the last four decades due to the fact that in spite of intense investigations the detailed structure of the TDs has persisted unclear.

A procedure to most efficiently create a subset of the TDs, the so-called Shallow Thermal Donors (STD), had been developed recently. The method enables the selective preparation of the first species of a family of STDs incorporating hydrogen (STD(H)).

These are studied by means of Fourier Transform Infrared Absorption (FTIR), Electron-Paramagnetic Resonance (EPR) and Electron-Nuclear Double Resonance and their formation next to the electronic and structural properties are analysed. A defect, which is supposed to represent the very first species of the STD(H), is measured for the first time. The results reveal the incorporation of one hydrogen atom and one silicon atom in the defect core. Our experimental results support an atomic model for the STD(H), which was previously calculated to be a shallow donor. According to this model in addition to two interstitial oxygen atoms, the core structure of the STD(H) is composed of a silicon atom and an interstitial carbon atom to which a hydrogen atom is bonded also. The addition of the hydrogen atom renders the defect shallower according to the theory. The atomic structure of further families of STDs is also discussed.

Furthermore the results from various experiments with EDEPR are summarised with the intention to gain more knowledge about the applicability of the method. Although EDEPR has been successfully applied to investigate various defects recently, an equal number of attempts to detect EDEPR signals of other defects failed. Due to the fact that the mechanism responsible for the detection of EDEPR has not been understood completely yet, the success of EDEPR experiments was not always predictable. The results obtained in the final chapter support a donor-acceptor pair recombination mechanism for EDEPR that was suggested earlier in this group. EDEPR spectra from samples which had been irradiated with electrons were recorded with very high signal-to-noise ratios. An “amplification” of signals occurring with weak intensities prior to irradiation is observed and the mechanism of it is revealed.

When studying the dangling bond centres variations of the modulation technique for the detection of the EDEPR signal have been introduced and the use of high microwave frequencies up to 72GHz has been realised. The “active” measurement layer is limited to only a few μm of depth from the sample surface for EDEPR in contrast to the whole sample volume in conventional EPR. However, the limitation can be of significant advantage when surface or surface-near defects have to be studied. The greatest benefit of EDEPR in comparison to EPR is the increased sensitivity regarding low defect concentrations in the samples.

Chapter 1

Fundamentals of the measurement techniques

Experimental methods used to analyse defects in semiconductors are manifold. When being concerned with the atomic and geometrical nature of the defect in question, Electron Paramagnetic Resonance (EPR) and its extension Electron Nuclear Double Resonance (ENDOR) are used. Both methods have been modified by the electrical detection of the magnetic resonance and have been called EDEPR and EDENDOR, respectively. The advantage of electrical detection over the conventional method can be found in a possible increased sensitivity regarding the defect concentration. In the following only a brief description of the methods is given. For further details the reader is referred to e.g. [Spaeth 1992][Stich 1995].

Next to the magnetic resonance techniques Fourier Transform Infrared Absorption (FTIR) was applied. This optical method was used to investigate the concentration and energy levels of certain defects. The basics of the infrared absorption and the benefits of the Fourier transformation method are explained briefly. The reader is referred to e.g. [Kuzmany 1989] for a detailed description.

1.1 Theoretical fundamentals of EPR and ENDOR

1.1.1 The spin Hamiltonian

When conventional EPR is applied to investigate a paramagnetic defect in a solid the transition $\Delta m_s = \pm 1$ of an unpaired electron in a static magnetic field \vec{B}_0 is directly detected via the absorption of microwave power. The energy levels contributing to the transition can be described by the spin Hamiltonian operator \mathcal{H} . This operator contains only energy terms that are related to the spin of electrons and nuclei involved in the resonant process. For a given system with $S = 1/2$ and $I \geq 1$ the spin Hamiltonian reads as follows:

$$\mathcal{H} = \mu_B \vec{S} \cdot \underline{\underline{g}} \cdot \vec{B}_0 + \sum_i \vec{I}_i \cdot \underline{\underline{A}_i} \cdot \vec{S} - \sum_i g_{n,i} \mu_n \vec{I}_i \cdot \vec{B}_0 + \sum_i \vec{I}_i \cdot \underline{\underline{Q}_i} \cdot \vec{I}_i \quad (1.1)$$

with μ_B the Bohr magneton \vec{S} electron spin operator

g electron g tensor \vec{B}_0 magnetic field

\vec{I}_i nuclear spin operator of the nucleus i

A_i hyperfine or superhyperfine structure tensor of the nucleus i

$g_{n,i}$ nuclear g factor of the nucleus i

μ_n nuclear magneton

\underline{Q}_i quadrupole tensor of the nucleus i .

The electron Zeeman operator \mathcal{H}_{EZ} describes the magnetic interaction between the spin \vec{S} of an unpaired electron and the external magnetic field \vec{B}_0 whereas the corresponding one of a nuclear spin \vec{I}_i is given by the nuclear Zeeman operator \mathcal{H}_{NZ} . The interaction between the electron spin \vec{S} and the nuclear spin \vec{I}_i of the central nucleus or a neighbour nucleus is given by the hyperfine (hf) or superhyperfine (shf) term $\mathcal{H}_{HF/SHF}$. The quadrupole term \mathcal{H}_Q contains the interaction between the nuclear quadrupole moment of a nucleus having $I > 1/2$ and the electric field gradient at its site.

The hf or shf tensor $\underline{\underline{A}}$ can be split into an isotropic part a and a traceless anisotropic part $\underline{\underline{B}}$.

$$\underline{\underline{A}} = a \cdot \underline{\underline{1}} + \underline{\underline{B}}. \quad (1.2)$$

where $\underline{\underline{1}}$ is the 3×3 unit matrix. Since the trace of the anisotropic hf or shf tensor is zero, the tensor can be described in its principal axes system by two independent interaction parameters

$$b = \frac{B_{zz}}{2} \quad (1.3)$$

and $b' = \frac{B_{xx} - B_{yy}}{2}$.

The scalar a , the so-called Fermi contact interaction constant, is proportional to the unpaired spin density at the site of a nucleus in a one-particle approximation for the centre wave function [Slichter 1989].

$$a = \frac{2}{3} \mu_0 g_e \mu_B g_n \mu_n \cdot |\Psi(0)|^2 \quad (1.4)$$

where μ_0 is the permeability of a vacuum.

The matrix elements of the anisotropic part $\underline{\underline{B}}$ are given by [Slichter 1989]

$$B_{ik} = \frac{1}{4\pi} \mu_0 g_e \mu_B g_n \mu_n \int \left\{ \frac{3x_i x_k}{r^5} - \frac{\delta_{ik}}{r^3} \right\} |\Psi(r)|^2 d\vec{r} \quad (1.5)$$

The quadrupole tensor $\underline{\underline{Q}_i}$, which does not vanish for nuclei with spin $I > 1/2$, is defined by

$$Q_{ik} = \frac{eQ}{2I(2I-1)} \cdot \frac{\partial^2 V}{\partial x_i \partial x_j} \quad (1.6)$$

with e elementary charge,

Q quadrupole moment of a nucleus,

V electric potential at the site of a nucleus.

The quadrupole tensor $\underline{\underline{Q}_i}$ is also traceless and can be described analogously to the anisotropic hf or shf tensor in its principal axes system by the two parameters

$$q = \frac{Q_{z'z'}}{2} \quad (1.7)$$

and $q' = \frac{Q_{x'x'} - Q_{y'y'}}{2}$

The z axis of the hf, shf or quadrupole tensor's principal axes system is to be aligned along the direction of the largest interaction by definition. Consequently, b and q yield the axially symmetric parts of each tensor, whereas b' and q' describe the deviation from axial symmetry.

The exact determination of the energy levels of a spin system requires a full diagonalisation of the appropriate spin Hamiltonian. For a rough estimation perturbation theory of first or second order is often helpful, provided that one term of the Hamiltonian dominates. For example if $\mathcal{H}_{EZ} \gg \mathcal{H}_{SHF}$ the interaction for a simple $S=1/2$ system with isotropic electronic and nuclear g -factors and one neighbour nucleus is given in first order perturbation theory by

$$E = m_S g \mu_B B_0 + m_S m_I W_{SHF} - m_I g_n \mu_n B_0 + \frac{1}{2} W_Q \left(m_I^2 - I(I+1)/3 \right) \quad (1.8)$$

with $W_{HF} = a + b(3 \cos^2 \vartheta - 1) + b' \sin^2 \vartheta \cos(2\phi)$ (1.9)

and $W_Q = 3q(3 \cos^2 \vartheta' - 1) + 3q' \sin^2 \vartheta' \cos(2\phi')$. (1.10)

ϑ and ϑ' are the angles between the z axis of the respective principal axes system and the magnetic field vector, ϕ and ϕ' the angles between the x axis and the projection of the magnetic field vector into the xy plane of the respective principal axes system (see e.g., [Spaeth 1992]).

1.1.2 Analysis of EPR spectra

EPR spectra are analysed by determining the energy differences between the levels between which transitions obeying the selection rules $\Delta m_S = \pm 1$ and $\Delta m_I = 0$ occur. For a $S=1/2$ system equation (1.8) yields the energy positions of the allowed EPR transitions according to first order perturbation theory.

$$\hbar \nu_{EPR} = g \mu_B B + m_I W_{SHF} \quad (1.11)$$

In an EPR experiment the microwave frequency is fixed while the magnetic field is swept. Thus equation (1.11) has to be solved for the corresponding resonant magnetic fields. The interaction matrices can be obtained by rotating the magnetic field in two perpendicular planes (or rotating the crystal relative to the fixed magnetic field). The angular dependencies usually yield much more resonances than needed for the determination of the spin Hamiltonian parameters. Therefore, the interaction tensors are adjusted to the observed resonances in an iterative procedure where the deviation squares of the measured and the calculated resonances are minimised.

1.1.3 Analysis of ENDOR spectra

ENDOR transitions obey the selection rules $\Delta m_S = 0$ and $\Delta m_I = \pm 1$. According to equation (1.8) first order theory yields

$$\hbar\nu_{\text{ENDOR}} = \left| m_S W_{\text{SHF}} - g_n \mu_n B + m_Q W_Q \right| \quad (1.12)$$

with $m_Q = (m_I + m_I')/2$.

m_I and m_I' represent the nuclear spin states between which the ENDOR transition occurs. Similar to the EPR analysis the corresponding interaction matrices are obtained by recording ENDOR angular dependencies for a rotation of the magnetic field vector in two perpendicular planes and fitting the interaction parameters to the experimental data. According to their separation from the defect centre, neighbouring nuclei are classified in different shells. The symmetry of a shell is determined by symmetry elements which transform the shell's nuclei into each other. The origin of each symmetry operation is the point group symmetry of the defect. For example a centre of inversion is determined by the Laue class of the centre (site). Each nucleus of a shell leads to a certain number of ENDOR lines depending on the nuclear spin and electron spin and thus to several ENDOR branches in the angular dependence [Spaeth 1992].

1.2 Experimental measurement method and setup for EPR and ENDOR

In contrast to electrically detected EPR, the EPR transitions in conventional experiments are detected via a microwave absorption. The nuclear magnetic resonance

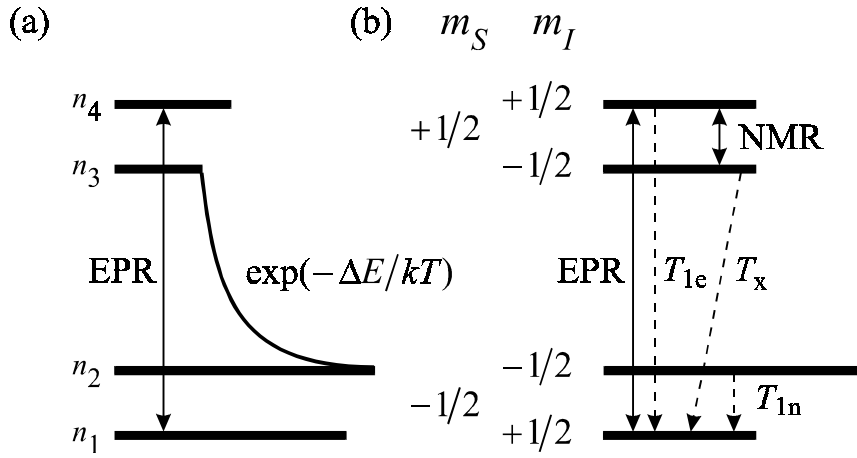


Figure 1.1 Schematic diagram explaining the EPR and ENDOR effect of a simple system having $S = 1/2$ and $I = 1/2$. The relative occupation of levels 1-4 is marked by their lengths considering a non-saturated EPR transition (figure 1.1a) and the stationary occupation for saturated EPR and NMR transitions, including possible relaxation mechanisms (figure 1.1b).

(NMR) transitions are monitored via a change of the EPR effect. To observe this ENDOR effect, the EPR transition has to be saturated partly by applying sufficiently high microwave power. The rf-induced NMR transition leads to a partial desaturation of the EPR, which is compensated by an increased microwave absorption (figure 1.1). The latter is detected (see e.g., [Spaeth 1992]). In stationary ENDOR experiments [Seidel 1961] one can make use of a cross-relaxation probability T_x^{-1} , which allows the stationary observation of the rf-induced desaturation of the EPR transition.

Figure 1.2 shows the schematic setup of a conventional X-band EPR-/ENDOR spectrometer, working as homodyne system in a reflex arrangement [Poole 1983]. A small part of the 100 mW microwave power generated by a YIG-oscillator (1) is branched off by a directional coupler (2) to a frequency counter. The main part is divided into the main and the reference arm by a second directional coupler (2). A phase shifter (4) allows to adjust the phase of microwave in the reference arm with respect to that of the main branch. Afterwards a 90°-hybrid (7) divides the microwave into two branches which are 90° phase-shifted against one another. Each branch is guided to the input of a mixer. The microwave power of the main branch is adjustable by an attenuator (3). Via a 3-gate-circulator (5) the microwave gets into a waveguide which ends in a TE_{011} microwave resonator (17). The coupling is done by a small hole at one side of the resonator. An adjustable antenna in front of the hole allows to adapt the wave resistance of the

resonator to that of the waveguide. In case of ideal adjustment no microwave power is reflected by the cavity. An absorbing medium in the resonator causes an unbalanced condition of the microwave bridge. The signal reflected in this case reaches a microwave amplifier (6) via the 3-gate-circulator, is amplified and guided via a power divider, both outputs having the same phase, into the respective second input of the two mixers. Each mixer multiplies the input signals. The output voltage U_{out} of the two mixers is [e.g. Spaeth 1992]

$$U_{\text{out}} = \sqrt{P_{\text{MW}}} \cdot a \cdot \cos \phi, \quad (1.13)$$

where P_{MW} is the microwave power reflected by the resonator, a is a device specific constant and ϕ the phase difference between both input signals. In case of identical phases equation (1.13) yields a positive dc voltage, whereas in case of $\phi = 90^\circ$ the dc voltage part equals zero. Using the phase shifter (4) the relative phase is adjusted in a way that the input signals of the mixer on the right have identical phases at the resonance frequency of the microwave cavity. An incomplete coupling into the resonator leads to a dc voltage at the mixers output, which is used to adjust the coupling plate accordingly (not depicted in figure 1.2). This automatic control loop makes a steady coupling possible, even though e.g. a temperature drift changes the position of the coupling plate or the resonance frequency of the cavity.

The automatic frequency control (AFC) is done by the mixer on the left. If the frequency of the YIG-oscillator (1) deviates from the resonance frequency of the cavity, the signal reflected by the resonator is phase-shifted with respect to the reference branch. This leads to a dc voltage at the output of the left mixer (9), which is used for the adjustment of the YIG-oscillator frequency.

The resonance absorption of the paramagnetic sample causes the balanced microwave bridge to deviate from the balance. The reflected microwave power changes and leads to a change in the dc voltage (eqn. (1.13)) at the output of the mixer on the right. This voltage is the final signal (10). To improve the sensitivity the lock-in technique with modulation of the magnetic field is used.

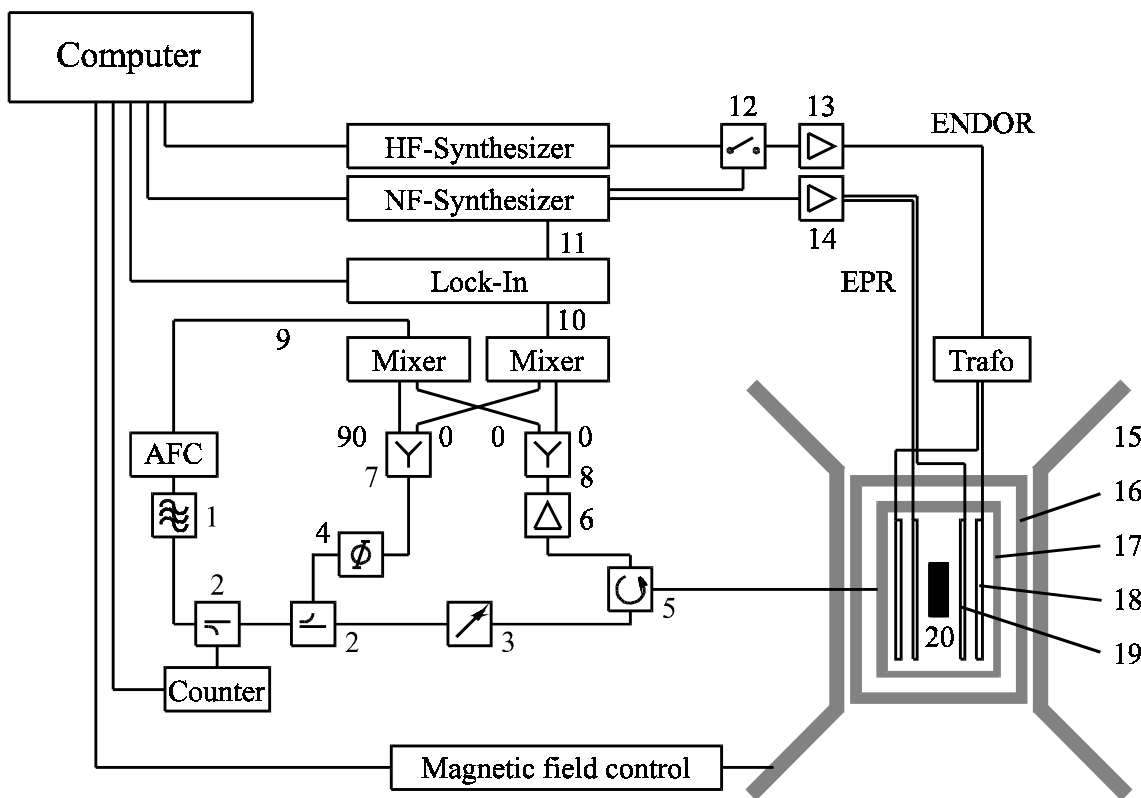


Fig. 1.2 Schematic diagram of an EPR/ENDOR spectrometer: (1) YIG-oscillator, (2) directional coupler, (3) attenuator, (4) phase shifter, (5) 3-gate-circulator, (6) microwave amplifier, (7) 90°-hybrid, (8) power divider, (9) dispersion signal, (10) absorption signal, (11) reference signal, (12) HF-switch, (13) HF-amplifier, (14) NF-amplifier, (15) magnet, (16) cryostat, (17) resonator, (18) ENDOR rods, (19) EPR rods, and (20) sample.

The resonator (17), into which the sample is placed, is part of a helium flux cryostat (16) such that temperatures down to 4.2K can be achieved. The temperature is stabilised by a resistor heater at the helium vaporiser and by a helium flux control. The microwave resonator (17) is situated in the homogeneous field region of a conventional electromagnet (15). The magnetic field modulation required for the lock-in detection of EPR measurements is generated by “EPR rods” (19), the radio frequency additionally required for ENDOR measurements by ENDOR rods (18). Both, EPR and ENDOR rods are placed in Helmholtz arrangement.

1.3 Electrically Detected EPR

The method of Electrically Detected EPR (EDEPR) was established in the group of Prof. Dr. J.-M. Spaeth only a few years ago and will explained in a more detailed fashion therefore. When performing EPR measurements a conductivity change of the sample can be monitored using electrical contacts on the sample surface. At first the method was called Spin-Dependent Recombination (SDR) or Spin-Dependent Photoconductivity (SDPC) (when used with excitation light), but rarely used to identify defects in semiconductors until the beginning of the 1990's. The method gained attraction after several publications by Stich et al. and the name Electrically Detected EPR (EDEPR) was established by these [Stich 1993]. Mainly two reasons can explain the previous neglect of this sensitive method. First, the majority of experiments using EDEPR were performed at room temperature, yielding only broadened and isotropic resonance lines at $g \approx 2$, e.g. [Solomon 1976]. No structural information could be derived from this spectra. Secondly, no suitable model explaining the phenomenon of EDEPR was presented, that could have given useful information under which conditions this method would work best. With each new defect to investigate the experimentalist had to test whether EDEPR would work or not.

In recent years an increased number of publications dealing with EDEPR can be found, e.g. [Bayerl 1998, Carlos 1997, Maier 1996]. The sensitivity gain regarding the defect concentration and the lower costs of EDEPR, both compared to conventional EPR, and the frequency independence of the EDEPR effect can be seen as one reason. Even stronger though the possibility to investigate small and integrated semiconductor devices and epitaxial layers has promoted the application of this method.

1.3.1 On the mechanisms of EDEPR

Several models explaining the EDEPR effect have been suggested in the past, yet no final theory could be presented until now. However, there is strong evidence that a spin-dependent recombination takes place between weakly exchange coupled donors and acceptors [Greulich-Weber 1995]. With the EDEPR models presented by Lépine and Kaplan two of the recent theories are presented in the following. For a further discussion of the models the reader is referred to the original literature or to [Stich 1997].

After measurements of the recombination at surface defects on crystalline silicon Lépine et al. proposed a model explaining the spin dependent conductivity [Lépine 1970, Lépine 1972]. It is based on the Shockley/Read/Hall-model (SRH), describing the capture and recombination of an electron and a hole at one defect [Shockley 1952, Hall 1952]. According to Lépine the recombination centre may be considered to have an unpaired electron spin, thus being paramagnetic prior to the capture of an electron. The Pauli principle only allows the occupation of one state by two electrons when having different spin orientations. Thus, the recombination is spin dependent, as the values for the capture cross section for the recombination centre are different for parallel and anti-parallel orientation of the conduction electron spin. Consequently, the recombination rate is strongly dependent on the spin orientation of the charge carriers and the recombination centres.

In an external magnetic field the spins align parallel to the magnetic field, a reduction of the recombination rate is the consequence. An increase of the recombination rate can be achieved if the degree of spin polarisation is lowered by a saturation of EPR transitions at the paramagnetic recombination centres. As a consequence, the EPR transitions lead to a decrease of the conductivity of the crystal.

Characteristic for the Lépine model is the dependence on the polarisation of the recombination centres and the conduction electrons. The value $\Delta\sigma$, representing the conductivity change of the crystal upon total saturation of the EPR transitions, is given as follows:

$$\Delta\sigma \propto p_e \cdot P_r \quad (1.14)$$

with

p_e : polarisation of the conduction electrons

P_r : polarisation of the unpaired hole at the recombination centre.

Several studies proved the proposed dependence of the conductivity from the polarisation of the recombination centres to be wrong [Kaplan 1978, Mima 1980, Vlasenko 1986, Barklie 1994]. A major deficiency of the Lépine model is the predicted low EDEPR conductivity change of only $\Delta\sigma/\sigma = 10^{-6}$ [Lépine 1972] whereas one of $\Delta\sigma/\sigma = 10^{-3}$ is observed in many experiments [Stich 1997]. Several variations to the model of Lépine have been presented [Wojsinski 1977, White 1977]. Nevertheless, it

has to be noticed that all models based on the spin-polarisation caused by an external magnetic field can not explain the magnitude of the detected spin-dependent effect. The first model to explain the process sufficiently was presented by Kaplan, Solomon and Mott and is called the KSM model [Kaplan 1978].

In contrast to the model presented by Lépine the KSM model is based on the assumption that electrons and holes are captured spin-independently, forming electron-hole-pairs subsequently. Two possibilities for this process were suggested. First, the electron-hole-pairs could be created at one defect, leading to an exciton-like recombination. Secondly, the pairs of electrons and holes could be trapped by donors and acceptors, respectively, preceding a donor-acceptor-recombination.

Following the KSM model the spin-dependence of the recombination can be explained by the fact, that with the recombination of the electron-hole-pairs a compensation of both spin and charge takes place, leading to a diamagnetic ground-state. Therefore the recombination of electron-hole-pairs is allowed for anti-parallel spins but forbidden for parallel spin conditions. In the case of an applied magnetic field the spins will turn into parallel orientation, making the recombination of electrons and holes impossible. When EPR transitions of the electrons and holes are induced, electron-hole-pairs will be shifted from parallel to anti-parallel spin orientation, thus leading to an increased recombination rate. It has to be noticed that in this model only the spin-correlation-effect of the electrons and holes within the electron-hole-pairs has an influence on the recombination rate. The latter is not dependent on the magnitude of an external magnetic field and hence the polarisation of electrons and holes.

Characteristic for EDEPR explained by the donor-acceptor-recombination mechanism is the microwave power dependence of the recorded signal. In contrast to EPR a different saturation of the signal is observed. For small microwave power the signal increases proportional with increasing power until it converges asymptotically a maximal signal.

According to Stich the power dependence of the EDEPR signal of the spin-dependent recombination of donor-acceptor-pairs can be written as follows:

$$S_{\text{EDEPR}} = C \frac{W_{\text{EPR}} T_R}{1 + W_{\text{EPR}} T_R} \quad (1.15)$$

with

W_{EPR} :EPR transition probability ($W_{\text{EPR}} \propto P_{\text{MW}}$)

The amplitude- (C) and “curve”-parameters (T_R) are given by

$$C = c/a \quad (1.16)$$

$$T_R = b/a. \quad (1.17)$$

The parameters a, b and c are composed of terms describing the generation and dissociation rates and the recombination probability of the donor-acceptor-pairs. Since the rates and the probability are positive, both parameters C and T_R are positive as well. It is implicit that for high microwave power the term ($W_{EPR} \cdot T_R \gg 1$) determines the maximum EDEPR signal. For a detailed explanation of the formula the reader is referred to [Stich 1997].

The power dependence of an EPR signal can be calculated as follows:

$$S_{EPR} = C_1 \left(\frac{1}{1 + C_2 P_{MW}} \right)^{\frac{3}{2}} \sqrt{P_{MW}} \quad (1.18)$$

with

C_1 : proportional constant

C_2 : “curve”-parameter of the conventional EPR

P_{MW} : microwave power.

The EPR signal grows proportionally to the microwave power at first. Yet, for relative low P_{MW} the signal reaches its maximum and decreases hyperbolically proportional to $1/P_{MW}$ with further increasing microwave power. Compared to the EDEPR signal a totally different microwave power dependence is detected for the EPR signal. The power dependence of an EPR and an EDEPR signal is illustrated in figure 1.3.

An further, important difference between EPR and EDEPR is the “active” measurement volume of the sample. For EPR defects in the whole (“bulk”) sample contributes to the recorded signal. According to investigations by Stich only a layer with a depth of approx. $5\mu\text{m}$ from the surface is measured [Stich 1997]. The measurement layer thickness is limited by the penetration depth of the above-band-gap light needed for the creation of excess charge carriers in the sample at low temperatures.

To determine the lowest number of spins detectable with EDEPR Stich performed measurements of phosphorous donors in a Cz-Si sample [Stich 1997]. The results

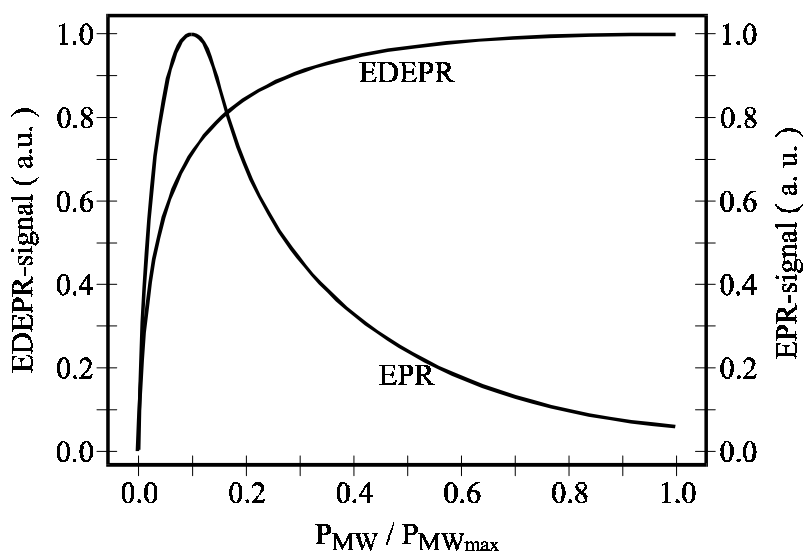


Fig. 1.3 Schematic illustration of the EPR and EDEPR signal dependence on the microwave power. For the EDEPR signal a donor-acceptor-pair recombination according to Stich is assumed [Stich 1997]. The max. microwave power is $P_{\text{MW}_{\text{max}}} = 400\text{mW}$.

yielded an absolute number of $N = 4 \cdot 10^7$ spins. A comparison with the theoretical lower limit of spins detectable in EPR of $N = 10^{11}$ spins (assuming 1cm^3 sample volume)[Spaeth 1992] reveals the significantly higher sensitivity with respect to the defect concentration of EDEPR over EPR.

Several different defect systems have been studied with EDEPR in the group of Prof. Dr. J.-M. Spaeth and the mechanism of the method has been investigated as well. For example it was found that the donor-acceptor recombination rate R_0 is correlated with the EPR transition probability W_{EPR} according to $R_0 \propto W_{\text{EPR}}$ [Stich 1997]. Further, the EDEPR signal intensity is dependent on the recombination rate R_0 . This donor-acceptor-recombination model established by Stich was developed for middle to low defect concentrations ($10^{16}\text{--}10^{13}\text{ cm}^{-3}$). For samples with high defect concentrations ($>10^{18}\text{ cm}^{-3}$) a high vicinity between the defect centres (donors and/or acceptors) appears. A different conduction mechanism is found which is described as hopping conductivity. The mechanism responsible for the spin dependent charge transport at high defect concentrations was studied by Grasa-Molina [Grasa-Molina 2000]. As an important result an *increase* of the conductivity, $\Delta\sigma/\sigma > 0$, was observed for EDEPR in the range of hopping conductivity.

As an important result of the studies it is noted that no quantitative analysis of defect concentrations can be performed on the basis of EDEPR measurements, even though a few publications have stated otherwise. In the final chapter of this work results of EDEPR measurements of several samples containing relative low defect concentrations (10^{11} – 10^{15})cm⁻³ are presented. The results are discussed in order to reveal the mechanism of the spin-dependent process. The findings indicate that a donor-acceptor-pair recombination as proposed by Stich gives rise to the recorded magnetic resonances [Stich 1997].

1.3.2 Experimental setup for EDEPR

In contrast to the setup for conventional EPR no sensitive devices for the detection of the absorbed microwave quanta is needed. Instead, the EPR effect is detected via the change of conductivity of the sample. Therefore a voltage is applied across the sample in a manner, that the resulting current through the sample is constant. The sample voltage is amplified and analysed using a lock-in amplifier combined with modulation of either magnetic field, microwave power amplitude or microwave frequency. Thus, the conductivity change can be detected easily. Except for samples with a very high concentration of defects an illumination of the specimen is necessary in order to create excess charge carriers. This is usually done with above-band-gap light by using a halogen or Hg-high-pressure lamp.

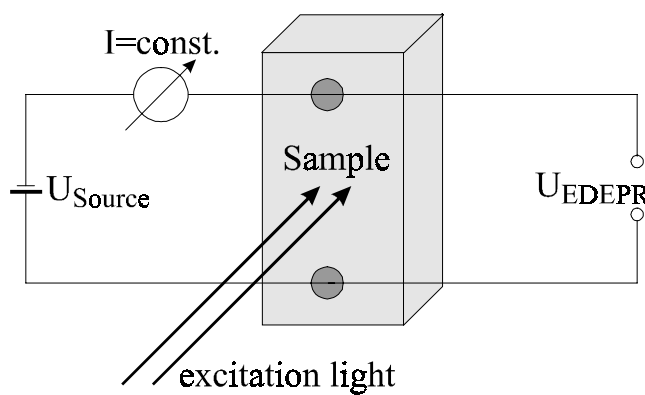


Fig. 1.4 Schematic diagram of the setup for detection of a conductivity change via current-voltage measurement. Above-band-gap light is needed at low temperature to create excess charge carriers.

A simple setup for this purpose is outlined in figure 1.4. In the case of a sample consisting of a p/n junction the conductivity change can also be detected by measuring the voltage across a resistor being attached to the sample contacts. For the latter method above-band-gap excitation light is needed to generate the photo-voltage.

Electrical contacts on the sample surface are needed. These should show an Ohmic I/U characteristic and a low contact resistance even at low temperatures. The preparation of the contacts can be carried out either by evaporation of a suitable metal (Al, Pb or Ti for n-type-silicon and Pt for p-type silicon) onto the cleaned surface or by applying aluminium to the sample mechanically [Langhanki 1996].

1.4 Fourier Transform Infrared Spectroscopy (FTIR)

To determine the concentration of defects in solids the method of infrared absorption spectroscopy is used often. Several disadvantages of the conventional, dispersive method in the infrared spectral range have led to the development of the Fourier Transform Infrared Spectroscopy (FTIR). The basis of this method and its setup are described briefly below.

When performing infrared absorption measurements to characterise defects in semiconductors two absorption processes have to be distinguished: whether they are caused by phonons or electrons. The phonon absorption (vibration of atoms or molecules) was used to determine the concentration of interstitial oxygen and substitutional carbon in silicon in this work. The electronic absorption lines arising from the transition of an electron from ground to an excited state, for example, give information about the concentration of certain defects investigated in this work (Thermal Donors, TD and Shallow Thermal donors, STD).

In the case of light being transmitted through a material with the thickness dx its intensity I is reduced by

$$dI = -\alpha dx I. \quad (1.19)$$

The absorption coefficient α is depending on the material and is of the dimension of m^{-1} . Upon integration the intensity decrease by a thickness of the material of x results in

$$I(x) = I(0) \cdot \exp(-\alpha x). \quad (1.20)$$

The transmission T is given by the fraction of the transmitted light as follows

$$T = \frac{I(x)}{I(0)}. \quad (1.21)$$

Consequently, prior to recording the IR spectrum of the sample a background spectrum with an empty sample holder has to be recorded.

The value of the noise level appearing between the absorption lines in the spectrum is usually lower than a value T_{\max} given for a certain material. Therefore a constant value for the background absorption $\alpha_B(v)$ has to be subtracted from the measured spectrum in order to gain the absorption $\alpha_T(v)$ caused by the defects.

$$\alpha_T(v) = \alpha(v) - \alpha_B(v) \quad (1.22)$$

In the case of a known capture cross section σ_{opt} for the absorption process the concentration N_T of the defect can be derived as follows:

$$N_T = \frac{\alpha_T(v)}{\sigma_{\text{opt}}(v)} = \alpha_T(v) \cdot K. \quad (1.23)$$

In literature, the calibration factor K is often given instead of the optical capture cross section, being the inverse of the latter.

The method of Fourier Transform IR measurement makes use of the interference of two light beams in an interferometer. The light from a special broad band IR source is reflected and transmitted with 50% each at a beamsplitter. After reflection of the beam at mirror M1 (fixed) and mirror M2 (movable) an interference pattern occurs at the IR detector. The intensity $I(x)$ of the interference pattern depends on the position of the mirror M2. A schematic setup for FTIR is given in figure 1.5. With the help of Fourier transform, the desired spectrum $S(v)$ can be derived from the interference function $I(x)$. As the whole spectral range is recorded in the measurement process simultaneously, the total measurement time is reduced greatly ("multiplex-advantage").

To investigate the above mentioned defects the existing Bruker IFS28 FTIR spectrometer had to be modified to enable measurements at low temperatures. A Leybold cryostat for continuous helium flow was used, allowing temperatures down to $T=6\text{K}$. Special care had to be taken selecting the cryostat windows as these have to transmit in the infrared spectral region, thus ZnS material was chosen.

The spectral range of the instrument is limited to $(7500\text{--}500)\text{cm}^{-1}$, due to the window material (ZnS) of the implemented cryostat, with a spectral resolution of 1cm^{-1} . KBr with a multilayer coating is used as the beamsplitter. The temperature available is between 6K and 400K and controlled by an Oxford DTC2. For measurements in which the absorption lines of water vapour in the air could superimpose the desired signals the whole measurement chamber and light path can be evacuated. A special feature of the used FTIR spectrometer can be found in a second interferometer implemented in the apparatus, used to determine the position of the moveable mirror M2 precisely ($\Delta x \approx 5\text{nm}$) and reproducibly. This feature is called “Connes-advantage”.

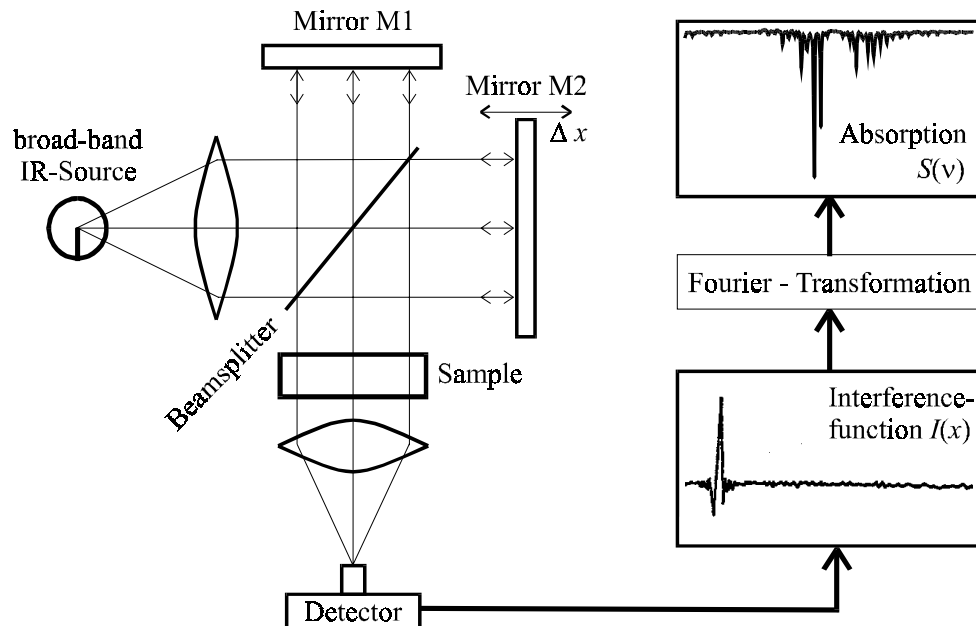


Fig. 1.5 Simplified block diagram of the setup for a Fourier Transform Infrared Absorption spectrometer FTIR.

Chapter 2

Advances in EDEPR technology

The electrical detection of EPR has been discovered over three decades ago as outlined in chapter 1.3. Nevertheless, little attention has been paid to this method for a long time and consequently the development of special features in this context, making use of the advantages of the electrical detection, has been neglected. Only few studies have been published dealing with different approaches to EDEPR [Woisinski 1976, Szkielko 1978]. In this work the attempt has been made to combine recent developments in EPR, like the application of high microwave frequencies, with EDEPR. It will be shown that apart from these adaptations further extensions have been developed leading to new set-ups for the electrical detection of EPR.

2.1 EDEPR with microwave power modulation

In the majority of studies with conventional EPR or EDEPR the static magnetic field \vec{B} is modulated in order to allow the use of a lock-in amplifier. Typical modulation frequencies are 100kHz for EPR and 5kHz for EDEPR, respectively. The use of magnetic field modulation requires either metallic rods inside the microwave cavity or solenoids outside the cavity walls. In the first case the quality factor Q is lowered. In the case of solenoids, more space is needed inside the cryostat, that has to be placed in the limited gap between the coils of the electro-magnet. In any case heat is transferred to the resonator from outside by the electrical connections.

Using microwave amplitude modulation these problems can be avoided as neither the rods nor the solenoids for modulation are needed. Further, when spectra consisting of

several overlapping EPR lines have to be examined, the determination of the individual line positions can be simplified.

It is noted that all spectra presented in this chapter have been measured using white light illumination of the sample by a halogen lamp in order to generate excess charge carriers for the spin dependent recombination process. Further, all spectra have been recorded at 10K. The spectra are shown as examples in order to illustrate the developed EDEPR features. A detailed study of the samples presented in figures 2.(1–3) and 2.(4–6) is given in chapter 3 and chapter 6, respectively.

In figure 2.1 two EDEPR spectra of a silicon sample with surface defects due to the implantation of Si- and Mo-atoms are shown. For spectrum (a) conventional sinusoidal magnetic field modulation is used. The number of derivative lines overlapping in the centre of the spectrum can hardly be estimated, let alone the position of the zero line

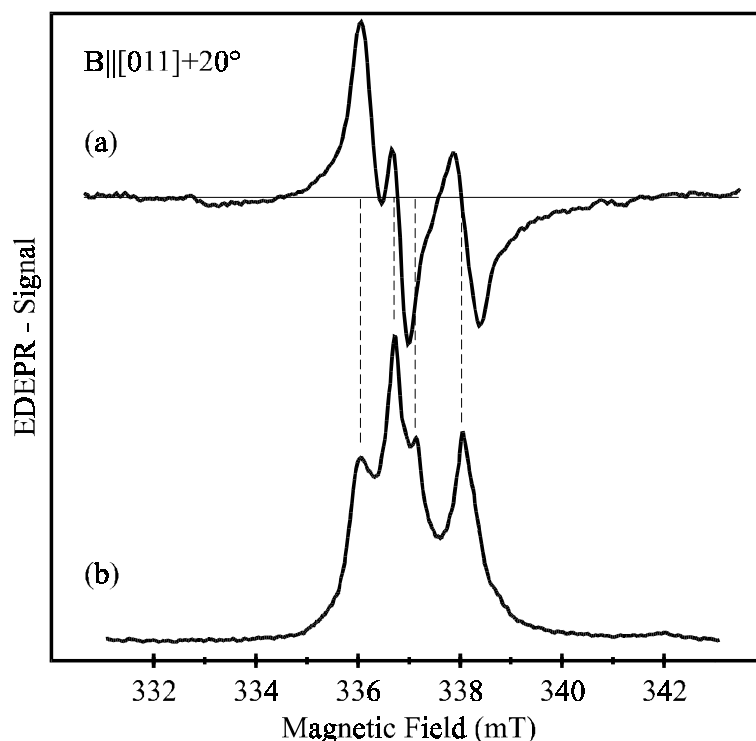


Fig. 2.1 X-band EDEPR spectra of a silicon sample with surface defects due to implantation of Si- and Mo-atoms using (a) sinusoidal modulation of the magnetic field with 5kHz/0.1mT and (b) square-wave microwave amplitude modulation with 0.7kHz/30dB.

crossing of the individual lines. The spectrum in part (b) is recorded applying microwave amplitude modulation with a maximal attenuation of 30dB. The amplitude was square wave (“on–off”) modulated and therefore an integrated EDEPR signal is obtained. At least four lines can be separated and their peak position determined precisely.

In general the method of effect modulation (for example magnetic field modulation) resulting in a differential signal is supposed to be superior for spectral resolution to one yielding an integrative signal [e.g. Poole 1983]. However, the present case reveals an exception from this rule.

For spectra with several resonance lines the question occurs whether the individual lines belong to one or several defects. In a first attempt this question can be answered by analysing the microwave power dependence of the individual lines. If the lines behave in a similar manner it can be assumed that their origin is the same. When regarding the spectrum in figure 2.1(a) the investigation of the power dependence will not give any answers about the individual signal behaviour as the lines can not be separated. Again

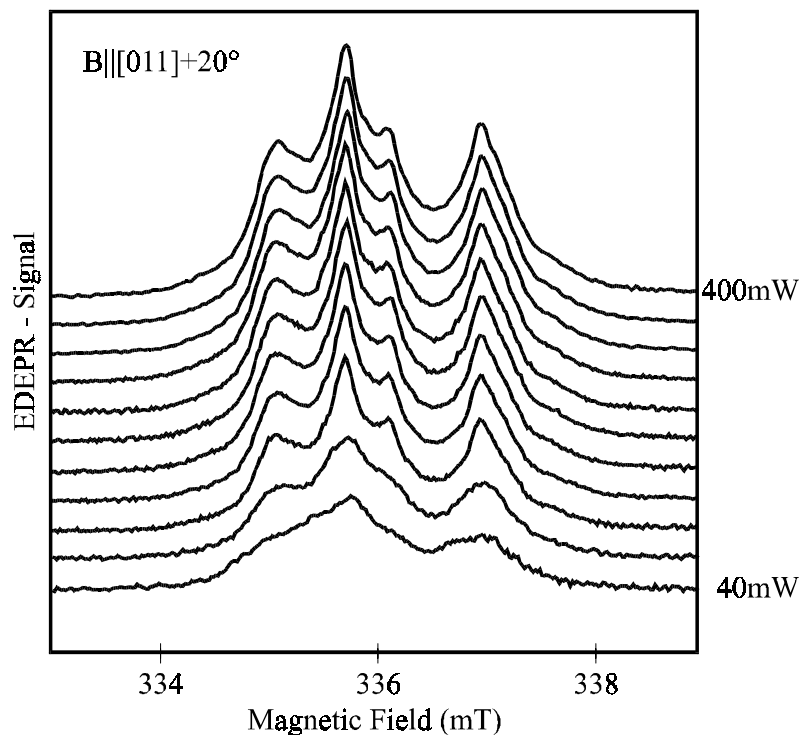


Fig. 2.2 Power dependent X-band EDEPR spectra of the sample presented in figure 2.1. The microwave power was reduced from 400mW to 40mW and square-wave modulated with 0.7kHz/30dB attenuation.

the amplitude modulation is superior as the development of each signal can be traced. An example for a power dependence taken with source amplitude modulation is given in figure 2.2. The evaluation of the line intensities of the resolved resonances shows that all four appear with the same microwave power dependence.

To gain structural information about a defect angular dependent magnetic resonance measurements are performed. An angular dependence starting with the spectrum presented in figure 2.1(a) could only be interpreted using a simulation program with various assumptions, giving rise to a high degree of uncertainty of the results. In figure 2.3 an angular dependence is shown making use of the source amplitude modulation technique. Again, certainty about the position of the individual resonance lines is achieved, resulting in a clear pattern of the symmetry of the defect. In this case two defects with a trigonal symmetry each can be detected.

For a further example of the benefits of EDEPR with source amplitude modulation a silicon sample irradiated with fast electrons was examined. The spectra recorded with

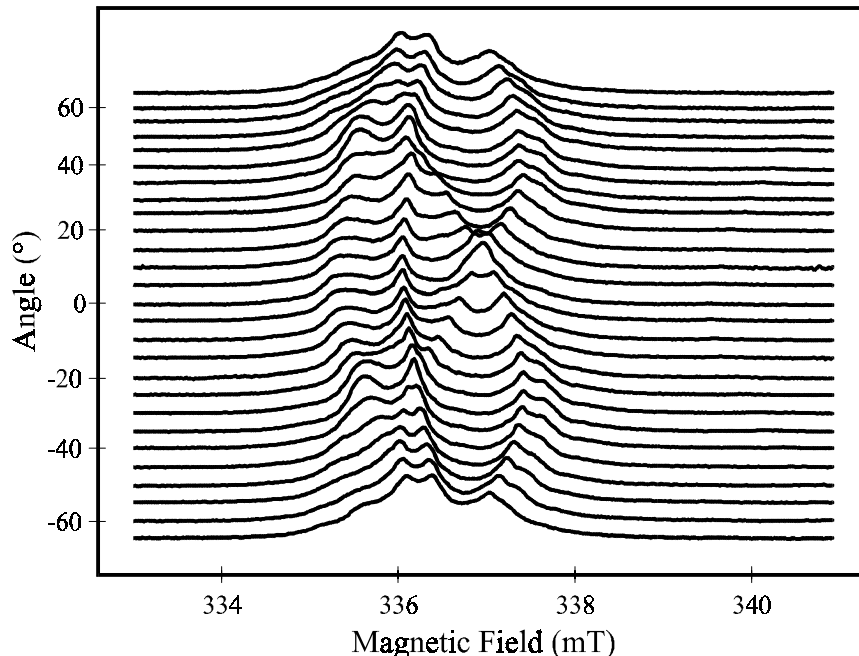


Fig. 2.3 Angular dependent X-band EDEPR spectra of the sample introduced in figure 2.1. Square-wave source amplitude modulation with 0.7kHz/30dB is used. The angles given represent the orientation of the sample surface relative to the static magnetic field.

both the conventional and the source modulation technique are given in figure 2.4. The two dominant lines in figure 2.4(a) arise from the hyperfine splitting of ^{31}P with an electron-spin $S = 1/2$ and spin $I = 1/2$ of the central nucleus. Phosphorous is the shallow dopant of this n-type silicon sample.

Next to this doublet six lines can be seen that are due the excited neutral triplet-state of the vacancy-oxygen pair $(\text{V}-\text{O})^{0*}$, labelled SL1 in literature. [Brower 1971] The SL1 ($S = 1/2$) signal arises only after illumination of the sample giving raise to a recombi-

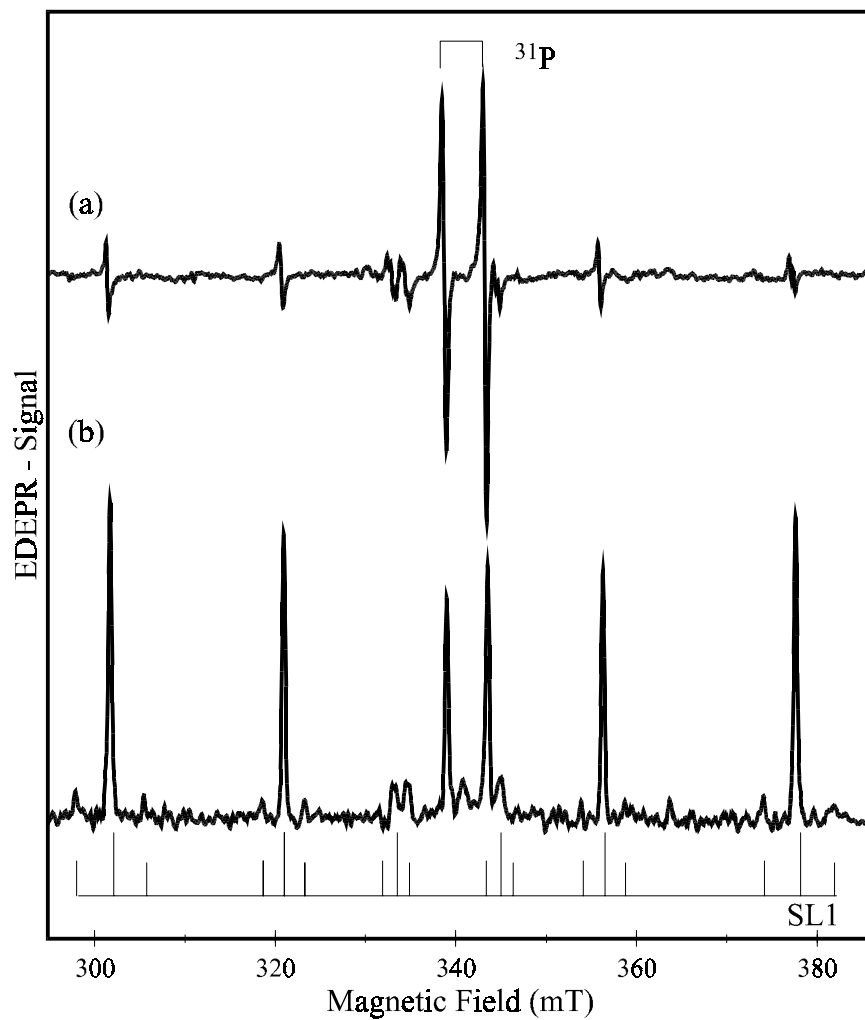


Fig. 2.4 X-band EDEPR spectra of a silicon sample after irradiation with fast electrons using modulation of (a) magnetic field with 5kHz/0.1mT and (b) microwave amplitude with 0.7kHz/30dB (square-wave). The integration time for (b) was only 30% of that needed for spectrum 2.4(a).

nation of free charge carriers at the vacancy-oxygen centre (V–O). The vacancies itself are introduced into the crystal by irradiation with fast electrons. Further lines appearing shall not be of interest here and are explained in detail in [Stich 1997]

Remarkable for the spectrum 2.4(b) is the short integration time (one third) compared to the one needed to record the spectrum in 2.4(a). In spite of the shorter measurement time more details are resolved such as the SL1-hyperfine satellite lines. They are caused by the hyperfine interaction of the SL1 electron spin $S = 1$ with the nuclear spin $I = 1/2$ of the ^{29}Si atoms which are present in the crystal with a natural abundance of 4.7%.

It is not directly apparent why the method of source amplitude modulation is more effective than the sinusoidal magnetic field modulation (effect modulation). From ENDOR measurements it is known that a square-wave modulation of the radio-frequency is superior to a modulation with a sine function [Spaeth 1992]. The advantage arises from the fact that the square-wave's fundamental *Fourier* component, as detected by a lock-in amplifier, is higher by about 30% than its amplitude. This results in a 30% signal improvement, a value in good agreement with the one obtained in this work for EDEPR.

For magnetic field modulation it is known that with the use of modulation amplitudes higher than the line-width a broadening of the respective line will occur [Poole 1983]. However, this is not the case for source amplitude modulation. Hence, the modulation amplitude can be increased significantly to improve the signal-to-noise ratio.

2.2 EDEPR with high microwave frequencies

In recent years great efforts have been undertaken to increase the microwave frequencies used to measure EPR. In spite of the difficulties in the technique of the microwave generation, guidance and control and the dimensions of the utilised microwave cavity decreasing proportionally to the increasing frequency, the benefits are on hand. With respect to equation 1.11 the use of high frequencies enables the separation of resonance lines being only distinguishable by small differences of their g-value. Many spectra known for their overlapping EPR lines when measured in the most commonly used X-band (8-12)GHz frequency region were resolved clearly after investigation with high frequencies and corresponding high magnetic fields.

So far EDEPR measurements were exclusively performed with X-band microwave sources except for tests with low frequency / low field EDEPR. The latter clearly

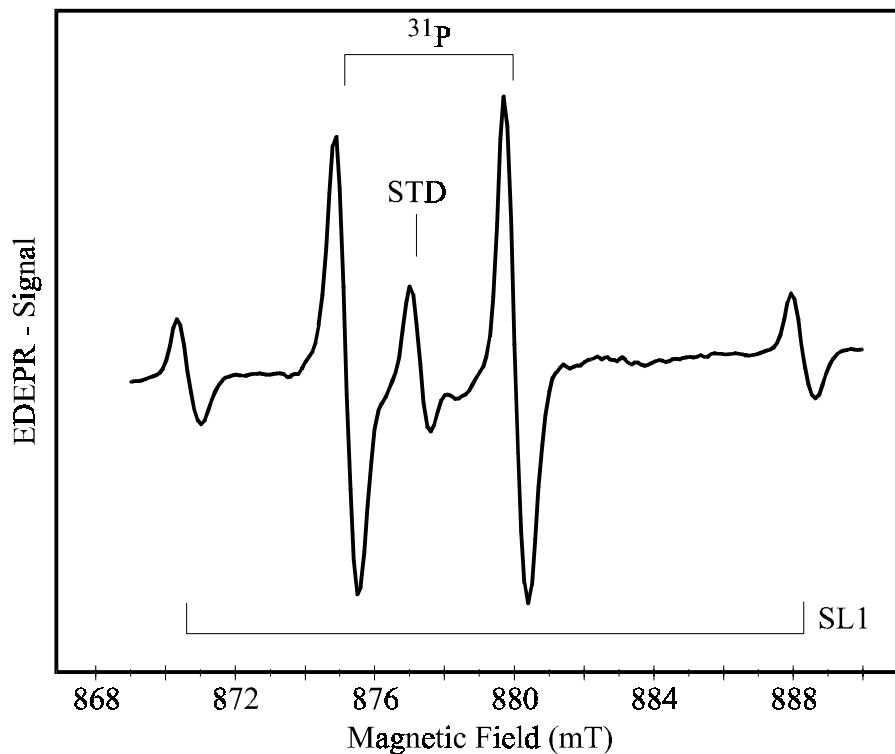


Fig. 2.5 K-band (25GHz) EDEPR spectra of a silicon sample after electron irradiation and heat treatment (→ shallow thermal donor, STD). Sinusoidal modulation of the microwave frequency was used in an experimental set-up without a microwave resonator. The resonances appearing between (874–882)mT are depicted in more detail in figure 2.6.

showed the frequency independence of the EDEPR effect but could not, of course, improve the resolution of details.

For this work the setup needed for EDEPR was transferred to a K-band (25GHz) spectrometer, providing an advantage in spectral resolution by a factor of 2.5. A spectrum of a Cz-Si sample after electron irradiation and heat treatment (30min / 450°C) measured at 25GHz is presented in figure 2.5.

The dimensions of a microwave cavity used for K-band frequencies are 15mm diameter and a length of 13 mm, generally spoken. Mounting the rods for magnetic field modulation and even more to insert a sample with dimensions of several millimetres into such a small cavity decreases often the quality factor Q of the cavity. In the case of EDEPR where thin wires are needed to electrically connect the sample contacts even more mate-

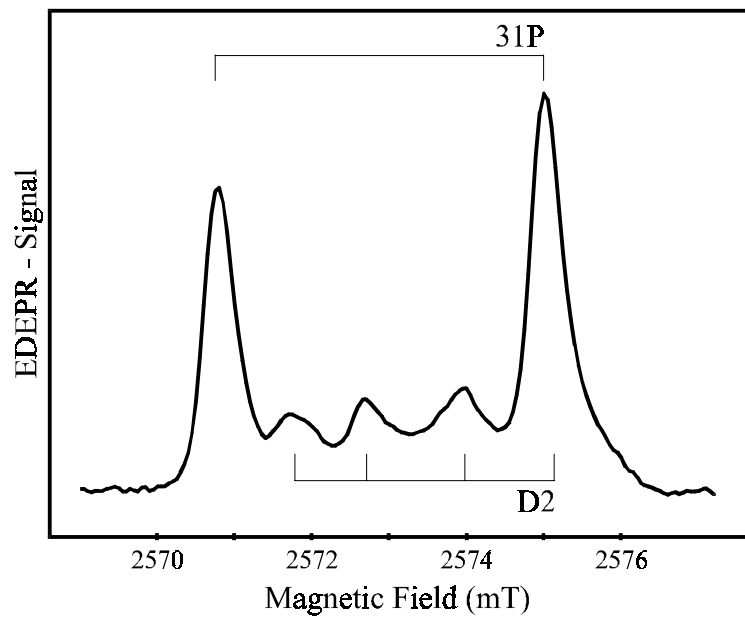


Fig. 2.6 V-band (72GHz) EDEPR spectrum of a silicon sample after electron irradiation and heat treatment. The dominating two lines are arise from ^{31}P . The high field ^{31}P -line superimposes one of the four lines of an anisotropic oxygen precipitation centre. The latter could not be resolved with K-band frequency (25GHz) and the selected resonance lines are identical to those appearing in figure 2.5 in the range of (874–882)mT. The orientation of the sample is $\vec{B} \parallel [011] + 20^\circ$. The spectrum was recorded using a modified high-field ODMR set-up without microwave resonator and with illumination of the sample. The microwave power was square-wave modulated with 30dB attenuation and a frequency of 500Hz.

rial with high conductivity is inserted into the resonator, which can lead to a complete loss of its resonant characteristics. The only way to proceed was to get rid of the cavity together with the adjacent modulation rods and to place the end of the microwave waveguide directly in front of the sample. For the spectrum in figure 2.5 a modulation of the microwave frequency was applied, making use of a sinusoidal variation of the reflector voltage of the employed Varian microwave clystron.

A further idea of these experiences was to transfer the EDEPR equipment to a V-band (72GHz) spectrometer, especially, as EDEPR measurements at frequencies as high as 72GHz have not been reported so far. The result of the implementation of this idea is

displayed in figure 2.6. The sample already investigated in K-band (figure 2.5) was used to show the resolution enhancement by the application of high microwave frequency. The two lines dominating the spectrum are due to the hyperfine splitting of the shallow dopant ^{31}P ($I = 1/2$). As the hyperfine splitting does not change with the microwave frequency the ^{31}P lines are ideal calibration peaks as their g-factor ($g=1.99850$) is known precisely as well [Feher 1959]. With the help of the ^{31}P lines and the obtained spectral resolution the principal values of the g -tensor of the defect can be determined with high precision.

In summary it has been shown that the electrical detection of EPR can be applied in a versatile manner, making use of various modulation techniques and microwave frequencies.

Chapter 3

EDEPR investigation of implanted and heat-treated FZ-silicon

In the following chapter the results of magnetic resonance studies of silicon samples after implantation of molybdenum (Mo) and silicon (Si) atoms are presented. The strong resonances detected with EDEPR at low temperatures were attributed to Mo-atoms at first sight. After detailed consideration of both the determined *g*-factors and the formation kinetics of the resonance lines this explanation had to be revised. The obtained spectra can be explained by Si/SiO₂ interface defects and dangling bond centres within the silicon bulk material.

The well known resonance lines of interface defects obtained by room temperature EPR measurements, called P_b-centres in the literature, are generally attributed to one defect centre. However, investigations by Stathis et al. already indicated that two independent defect centres, called P_{b0} and P_{b1}, should be the origin of the signals occurring on (100) oriented Si/SiO₂ interfaces [Stathis 1994].

Two separate defect centres can clearly be distinguished by EDEPR at low temperatures in this study. One of them is very similar to the P_{b0}-centre reported in the literature and an identification is tempting, whereas the other centre is detected for the first time. An explanation of the resonances due to two dangling bond centres at and below the technologically important (100) Si/SiO₂ surface is given and the results are critically compared with those reported in the literature.

In this chapter no detailed discussion of the EDEPR mechanism responsible for the detection of the dangling bond resonances is presented since in a later chapter the EDEPR mechanism will subject of the investigations.

3.1 Motivation for Mo-implantation into silicon samples

In order to dope FZ-silicon with the intention to generate shallow acceptors (p-type silicon) boron is generally added to the melt during the silicon crystal growth process. For acceptor-doping during device fabrication boron is implanted into the device. Since boron is a rather small atom the penetration depths are large. This rules out the method for multiply stacked, state-of-the-art thin layers, where separate layers have to be doped individually. A procedure to avoid the penetration of boron through several layers was found by complexing it with fluorine (F) to BF_2 prior to implantation. Both the size and the weight of the BF_2 greatly reduce the implantation penetration depth to a few hundred Å. Annealing procedures after implantation are used to dissociate the molecule and to out-diffuse the fluorine, resulting in a boron doping of the specific layer.

Unfortunately, high molybdenum concentrations up to 10^{18}cm^{-3} were found by secondary ion mass spectroscopy (SIMS) in devices prepared this way. Molybdenum is a strong minority lifetime killer in silicon, forming an electrically active deep level at $E_V+0.31\text{eV}$ and thus acting as a powerful recombination centre [Rohatgi 1980][Ghandhi 1983]. Moreover, molybdenum has been characterised as a fast diffuser, with a diffusivity in the range of $10^{-8}\text{cm}^2/\text{s}$ at elevated temperatures [Tobin 1985]. This makes it a dangerous contaminant, particularly in devices requiring long minority carrier lifetimes such as bipolar transistors and solar cells. The explanation for the Mo-contamination can be found in the coincidence of the charge-to-mass ratio for doubly ionised $^{98}\text{Mo}^{2+}$ and the $^{11}\text{B}^{19}\text{F}_2^+$ molecular ion. Thus, the molybdenum ion is not filtered out by the mass analyser magnet of the implantation set-up and the element is co-implanted.

With the intention to study the effect of molybdenum in silicon, p-type FZ-silicon samples (boron-doped, $n(\text{B})=2\cdot10^{15}\text{cm}^{-3}$) were implanted with molybdenum at 50keV and a density of $1.3\cdot10^{11}\text{cm}^{-2}$. The projected penetration depth for the Mo-atoms is 350Å [Michel 2000] according to calculations with a program called “TRansport of Ions in Matter”, TRIM. In the TRIM program the energy dependence of stopping powers for each element is given as a data base, and the main fitting parameter is the density of silicon. Selected samples were implanted with Si-atoms with various energies additionally and others were annealed after the implantation. The samples were provided by Dr. J. Michel from the MIT, Cambridge, MA, USA.

3.2 EPR of Mo- and Si-implanted and annealed FZ-silicon

In figure 3.1 EPR spectra of a silicon sample implanted with molybdenum and annealed at 838°C for 10h are shown. The spectra were recorded using two microwave frequencies of 9.8GHz and 25.0GHz, respectively. In each spectrum a single, weak resonance line is detected. Angular dependent measurements revealed an isotropic behaviour of the line with a g -factor of 1.9984 ± 0.0004 . The angular dependence showed particularities regarding the line-shape which have been called “breathing behaviour” in the literature, being a cyclical broadening of the linewidth upon rotation of the sample [Wörner 1985]. Both, the change of the line-shape and the isotropic g -factor indicate an identification of the observed resonance with the so-called New Donors ($g=1.9984$), arising after heat treatment at high temperatures ($550\text{--}800$)°C [Suezawa 1983]. In the literature the resonance has been associated with a superposition of several resonances

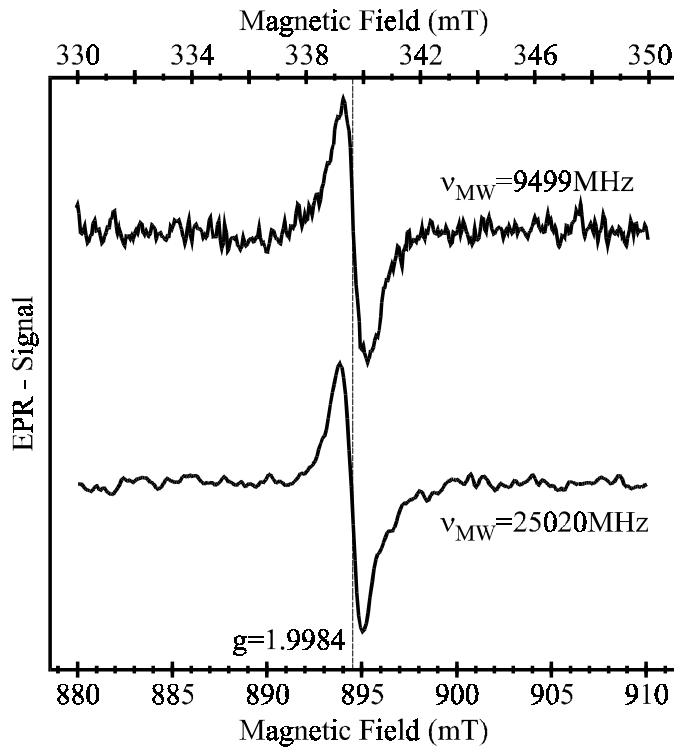


Fig. 3.1 EPR spectra of a FZ-silicon sample after molybdenum-implantation and annealing at 837°C for 10h. The spectra were recorded at 10K with X-band- (upper curve) and K-band-frequency (lower curve). Illumination of the sample showed no change of the spectrum in both cases.

after annealing being due to interface traps at Si/SiO_x interfaces as they occur in amorphous environment [Hölzlein 1984]. In the present case such interfaces and amorphous regions in the silicon crystal are most likely to appear after the implantation of molybdenum or silicon atoms.

It is noted that the resonances presented in figure 3.1 are directly related to the annealing process and did not occur without it. However, they appeared with increased signal intensity for samples which had been implanted with Si or Mo prior to annealing.

3.3 EDEPR of Mo- and Si-implanted and annealed FZ-silicon

As no further information about molybdenum in silicon could be gained by EPR measurements EDEPR was applied to investigate the samples. Ohmic contacts were fabricated on the implanted side of the specimen and illumination with white light from a halogen lamp was used on this sample side to create excess charge carriers at low temperatures. In figure 3.2 four EDEPR spectra recorded with identical integration times for the entire spectrum are shown.

Spectrum 3.2.a is obtained from a non-implanted FZ-silicon sample which has been annealed at 838°C for 30min. It has been magnified by a factor of 10. The samples for spectra 3.2.b (magnified by a factor of 5) and 3.2.c were implanted with silicon atoms (22keV, $1.3 \cdot 10^{13} \text{ cm}^{-2}$) and molybdenum atoms (50keV, $1.3 \cdot 10^{11} \text{ cm}^{-2}$), respectively, and subsequently annealed at 838°C for 30min and 10h, respectively. The spectra 3.2.a–c show a striking similarity of both the line shapes and positions of the resonances.

Only the spectrum in 3.2.d, obtained from a sample after Mo- (50keV, $1.3 \cdot 10^{11} \text{ cm}^{-2}$) and Si-implantation (7MeV, $4 \cdot 10^{14} \text{ cm}^{-2}$), and annealing at 838°C for 5h after each implantation step, shows differences. The spectrum reveals clear changes in line shape after the implantation of high-energy Si-atoms by new resonances superimposing the precedent group of resonance lines. The change in line-shape is most probably due to an increased damage after the implantation of the Si-atoms and will be discussed later.

In the spectra of Mo-implanted samples resonances lines of Mo should appear corresponding to the natural abundance of approximately 25.5%, taking into account the isotopes ⁹⁵Mo(15.9%) and ⁹⁷Mo(9.6%). Though both isotopes show a nuclear spin of $I=5/2$ no hf structure could be detected. As can be seen clearly in figure 3.2.b the same group of superimposed resonance lines found in the Mo-implanted sample appears in the spectrum of a Si-implanted one as well. Especially remarkable is the appearance of

this group of lines in the specimen exclusively annealed. Therefore, an identification of these lines with resonances due to Mo-atoms must be ruled out.

Taking into account the *g*-factors and the presence of the detected resonance lines even in nominally non-implanted samples leads to the family of intensively studied and yet controversially discussed surface defects, also known as “dangling bonds”, dislocation

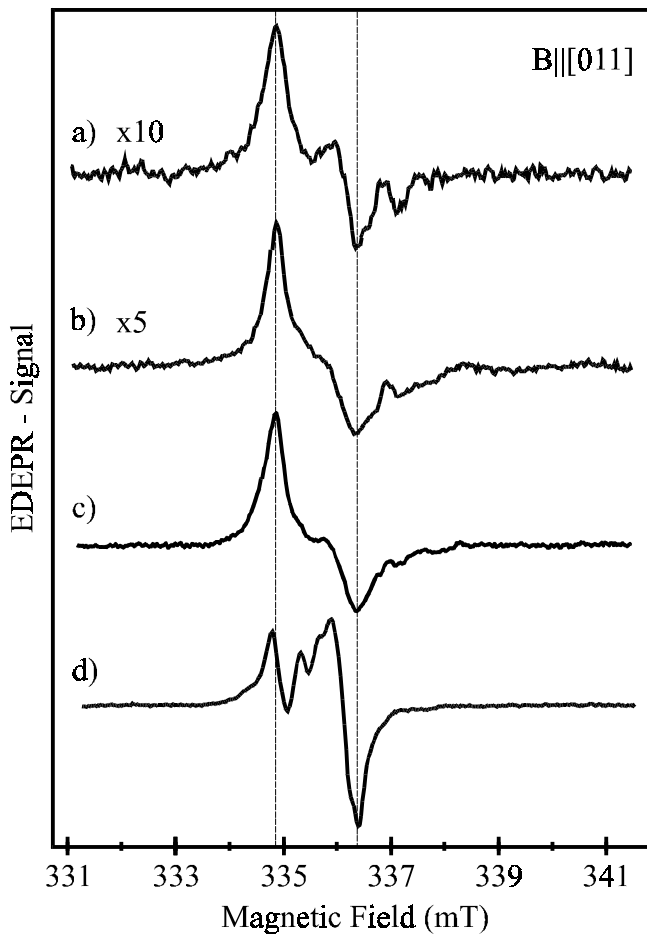


Fig. 3.2 EDEPR spectra of FZ-silicon samples after
 a) annealing at 838°C for 30min,
 b) implantation of Si-atoms (22keV) and annealing at 838°C for 30min,
 c) implantation of Mo-atoms (50keV) and annealing at 838°C for 10h,
 d) impl. of Mo- and Si-atoms (50keV / 7MeV) and ann. at 838°C for 10h.
 The samples were illuminated with white light and a sample current of $5\mu\text{A}$ was applied. The spectra were recorded in X-band at $T=10\text{K}$ using magnetic field modulation (5kHz) for an sample orientation of $\vec{B} \parallel [011]$.

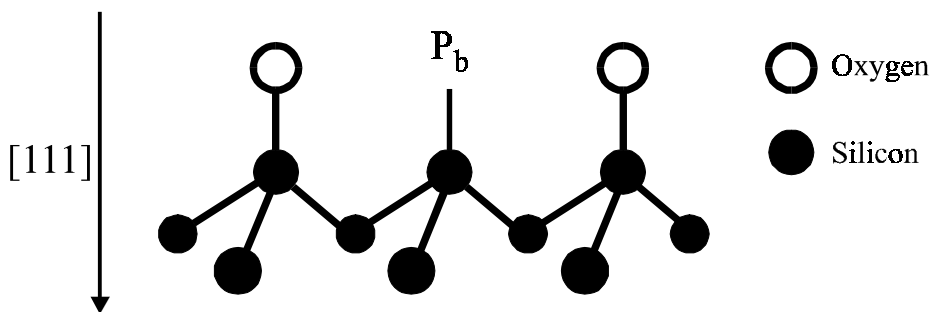


Fig. 3.3 Model of the P_b -defect occurring at (111) Si/SiO₂ interfaces after Poindexter et al. [Poindexter 1981].

or interface centres. The commonly used abbreviation for these defects is “ P_b -centres”. It has been established that they appear at Si/SiO₂ interfaces which not necessarily have to be located within the volume of a specimen but can also be found at the surface of the specimen. The “omnipresence” of the Si/SiO₂ interface defects can be explained by the fast oxidation of a pure silicon surface to SiO₂ with a thickness of SiO₂ of 24Å in 24h after exposition to air even at room temperature [Archer 1957].

The dangling bonds at the (111)-oriented Si/SiO₂ interface were detected first and are labelled P_b -centres. Room temperature EPR and photo-conductive resonance (PCR) have been widely used to investigate the structure of the P_b -centres [Poindexter 1978] [Brower 1986] [Cantin 1995]. The paramagnetic centre giving rise to the P_b resonances is shown in figure 3.3. It is apparent that it shows axial symmetry along a [111] direction. The paramagnetism is supposed to arise from an unpaired electron localised in a dangling bond silicon hybrid orbital of a Si-atom being bonded covalently to the three lower Si-atoms. These dangling bonds are also made responsible for charge trapping at the interface [Lenahan 1982].

At (111) Si/SiO₂ only the single variety P_b -centre of a dangling bond defect arises. Because of its relative simplicity, the majority of fundamental research about defects at the Si/SiO₂ interface has been carried out at the (111) surface. Therefore, the knowledge about this P_b centre is quite detailed.

However, for semiconductor integrated circuits the (100) surface is the preferred one. As the dangling bond defect structure appears to be more complicated for the (100) Si/SiO₂ interface the experimental results have been discussed controversially and the understanding is incomplete. Two resonances have been presented forming at this interface, called P_{b0} and P_{b1} . They appear with g -values of $g=2.0060$ and $g=2.0032$, respec-

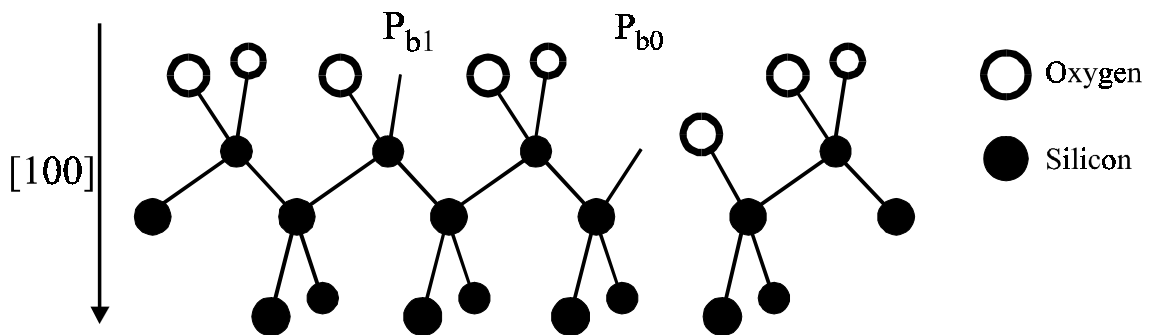


Fig. 3.4 Model of the P_{b1} and P_{b0} defects occurring at (100) Si/SiO₂ interfaces after Poindexter et al. [Poindexter 1981].

tively, for a sample orientation of $\vec{B} \parallel [110]$ [Poindexter 1981][Stathis 1991]. The precise structure of the responsible defects and the relation to the P_b centre at the (111) surface has not yet been clarified.

In search of the origin of the P_{b0} resonance Stathis and Dori proposed either a defect being fundamentally different from a dangling bond, or a dangling bond lying deeper inside the bulk silicon material away from the interface [Stathis 1991]. An atomic model of the proposed structure of P_{b0} and P_{b1} at the (100) Si/SiO₂ interface is displayed in figure 3.4. It is recalled that at the (111) interface only one type of dangling bond arises with an axial symmetry. For samples oriented with a (100) plane at least two different dangling bond structures have been proposed. Both show axial symmetry about the (111) direction. The P_{b1} centre is supposed to arise directly at the Si/SiO₂ interface whereas the P_{b0} is located below the interface. By the observation of different reactions on treatment with atomic hydrogen on the P_{b0} and P_{b1} at the (100) Si/SiO₂ interface strong indications were presented arguing against a single origin for both centres [Stathis 1994]. So far, the (100) interface had been studied with EPR with magnetic field modulation. The resulting resonances with differential line-shapes are strongly overlapping, inhibiting a detailed investigation of the individual resonances.

It is noted that no EDEPR resonances of these P_b -defects could be measured at room temperature in this study. Experiments were carried out with modulation frequencies up to 100kHz with and without above-band-gap illumination. It seems that the EDEPR effect is not observable at room temperature because of spin dependent recombination times being too fast to be influenced by the available microwave power, i.e. spin flip

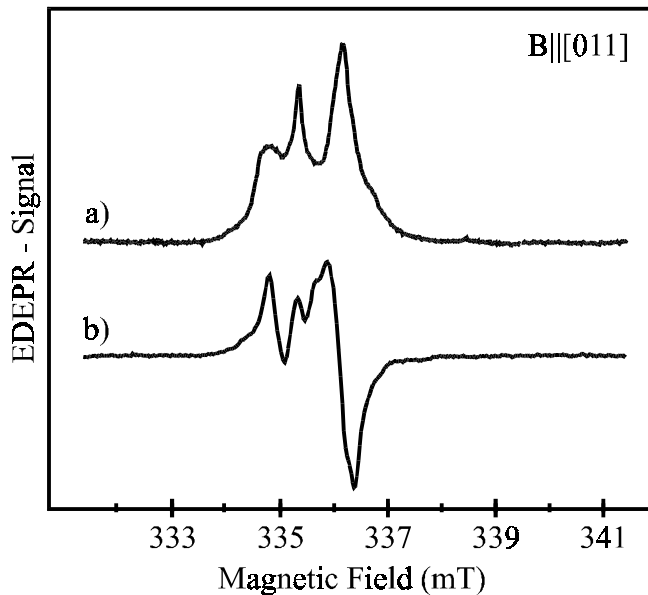


Fig. 3.5 EDEPR spectra of a FZ-silicon sample after implantation of Mo- and Si-atoms (50keV / 7MeV) and annealing at 838°C for 10h. The sample was illuminated with white light and a sample current of 5 μ A was applied. The spectra were recorded in X-band at T=10K using a) square wave microwave amplitude modulation with 700Hz/30dB attenuation and b) magnetic field modulation (5kHz). A further set of spectra is shown in figure 2.1.

rates. Experiments using conventional X-and K-band EPR were not successful with respect to the dangling bond resonances since the total number of these paramagnetic centers was not high enough in the available samples. It is recalled that the minimum absolute number of paramagnetic centres needed for the detection of EPR is $N = 10^{11}$ [Spaeth 1992]. As a consequence, the number of present P_b -centres is estimated to be lower than this value. The detection of the P_b -centres with EDEPR at low temperatures underlines the higher sensitivity regarding the defect concentration of this method.

The findings are supported by taking into account the generally accepted value of a P_b -centre density of 10^{12}cm^{-2} for samples annealed in oxygen atmosphere [Caplan 1979]. The samples investigated in this work have been annealed in an inert atmosphere (Ar) and their surface area is approx. 0.1cm^2 only. Consequently, the total number of interface defects is smaller than $N = 10^{11}$. The value is too low for EPR but sufficient for EDEPR as confirmed by the experimental results.

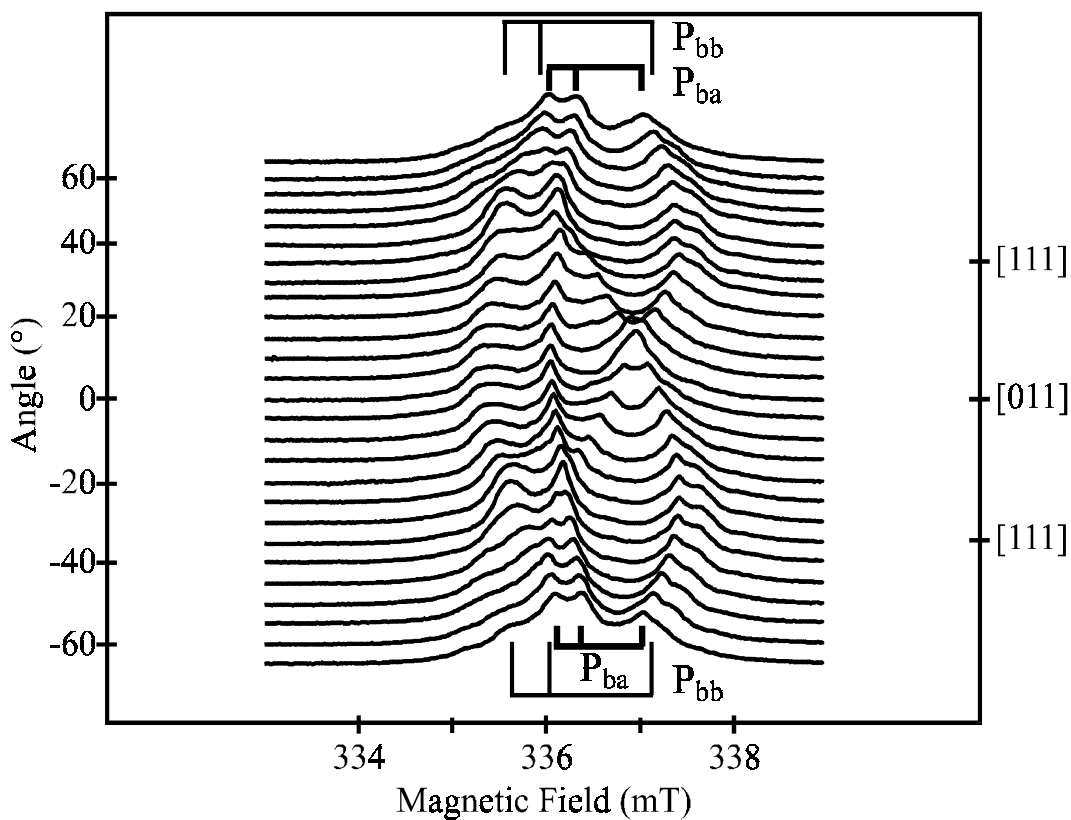


Fig. 3.6 EDEPR spectra of a FZ-silicon sample after Mo- and Si-implantation with 50keV and 7MeV, respectively. Annealing steps were carried out at 838°C for 5h after each implantation. Microwave power modulation (700Hz) was used in X-band at 10K. The sample was rotated in a $(\bar{0}\bar{1}1)$ -plane, the rotation angle being limited to 65° by the necessity of sufficient illumination of the sample surface with white light.

Various procedures were used to increase the absolute number of P_b -centres to enable their detection with EPR. Some authors prepared porous silicon layers with a thickness up to 120 μ m, hence containing a large number the interface defects [e.g. Mao 1993]. Others stacked together up to 35 samples to increase the investigated Si/SiO₂ interface area up to 30cm². The defects at the interface were prepared by long-term annealing in O₂ atmosphere at 900°C [e.g. Brower 1983].

In the present case the samples with Mo-implantation had been oriented with a (100) surface. Thus, they are candidates for the investigation of the P_{b0} and P_{b1} centres at the (100) Si/SiO₂ interface. In figure 3.5 two spectra from a sample after Mo- and Si-

implantation and annealing are shown. Spectrum 3.5 (b) is recorded using conventional magnetic field modulation (5kHz) whereas for spectrum 3.5 (a) a square-wave modulation (700Hz/30db) of the microwave power amplitude as described in chapter 2 was applied. The spectrum 3.5 (a) shows the high signal-to-noise ratio and an increased spectral resolution of this EDEPR technique.

In figure 3.7 angular dependent EDEPR spectra of the sample presented in figure 3.5.a are given. The pattern was obtained by rotation of the sample in a $(0\bar{1}1)$ -plane from $\vec{B} \parallel [011]$ towards $\vec{B} \parallel [100]$. Next to the three dominant resonance lines placed centrally in the spectra a further group of resonances can be detected. The latter appears with reduced intensity and a larger anisotropy. It lies centrally below the dominant lines. In comparison with the spectra published so far the obtained resolution is significantly higher and this second group of lines is detected for the first time. For clarification reasons the dominant group of lines will be labelled P_{ba} whereas the underlying one will be referred to as P_{bb} in the following. The angular dependence of the detected resonances can be simulated assuming a [111] threefold axially symmetric g -tensor. The resulting g -factors are given in table 3.1. The intensity ratio between the two defects was estimated to 3:1 from the EDEPR lines. In figure 3.7 both the experimental data points obtained from the angular dependent EDEPR spectra (figure 3.6) and the results of calculations using trigonal symmetry (solid lines) are given.

Centre	g_{\parallel}	g_{\perp}	Refs.
P_{ba} on (100)	2.0008	2.0098	this work
P_{bb} on (100)	1.9974	2.0160	this work
P_b at Si/SiO ₂	2.0012	2.0081	Caplan 1979
P_b at Si/SiO ₂	2.0013	2.0090	Stesmans 1986
Porous Si	2.0023	2.0090	Mao 1993

Table 3.1 Values of the g -factors of dangling-bond-related paramagnetic defects ($S=1/2$) investigated in this work ($\Delta g_{\parallel/\perp} = \pm 0.0004$) and compared to those of several related centres published previously.

From the rotation pattern it can be derived that the axial directions of the dangling bonds are distributed in all the four [111] crystal axes of the original silicon lattice. Resuming the results so far, both centres, P_{ba} and P_{bb} , can be attributed to dangling bonds located in silicon or at the (100) Si/SiO₂ interface. The difference in origin of the two centres is not apparent, yet.

The intensity of the dominant group of resonance lines, P_{ba} , is significantly enhanced after the implantation of fast Si-atoms only. The implantation of low-energy Mo-atoms increased the broader P_{bb} signal already being present after annealing of the sample. All

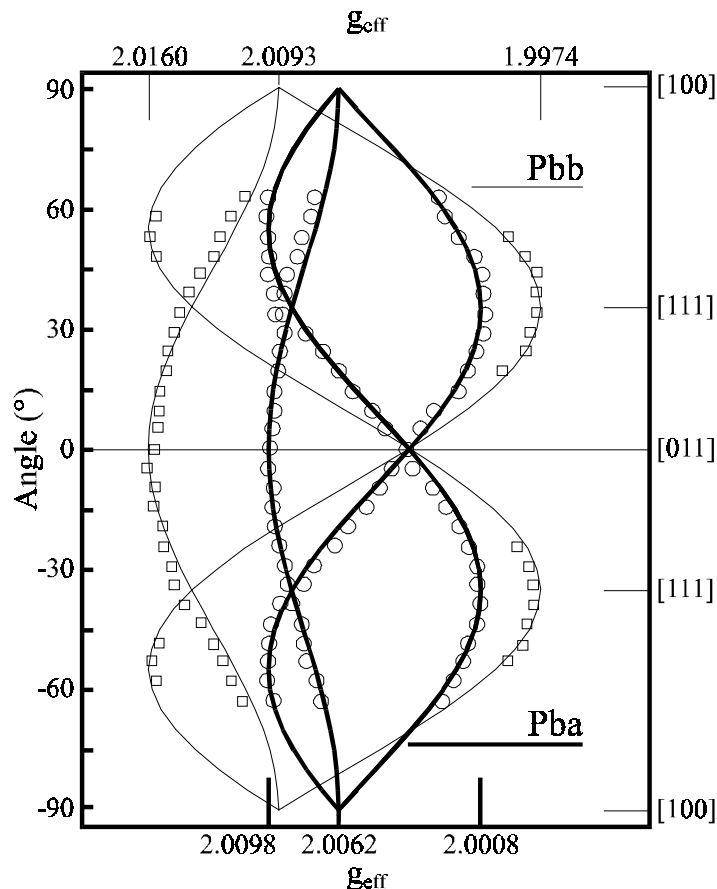


Fig. 3.7 Experimental (open squares and circles) and theoretical (solid lines) rotation patterns of the EDEPR angular dependent spectra presented in figure 3.6 (microwave amplitude modulation). The rotation takes place in a (0̄11)-plane. The spin Hamilton-parameters used for the calculation of the solid lines are given in table 3.1.

samples have been chemically polished with acids containing HF. This procedure is known to give rise to dangling bond related resonances, which can be intensified by subsequent annealing [Mendz 1980]. Further, the projected range of 50keV Mo-implantation was estimated to be 340Å by TRIM calculations, whereas the corresponding value for 7MeV Si-implantation is calculated to 3.5μm.

Since the depth of the “active” measurement layer in the case of EDEPR is approximately 5μm (the penetration depth of the above band gap light), the implantation with an impact reaching further below the surface will increase the EDEPR signal. This supports the assumption of the P_{ba} center being caused by the implantation of the high en-

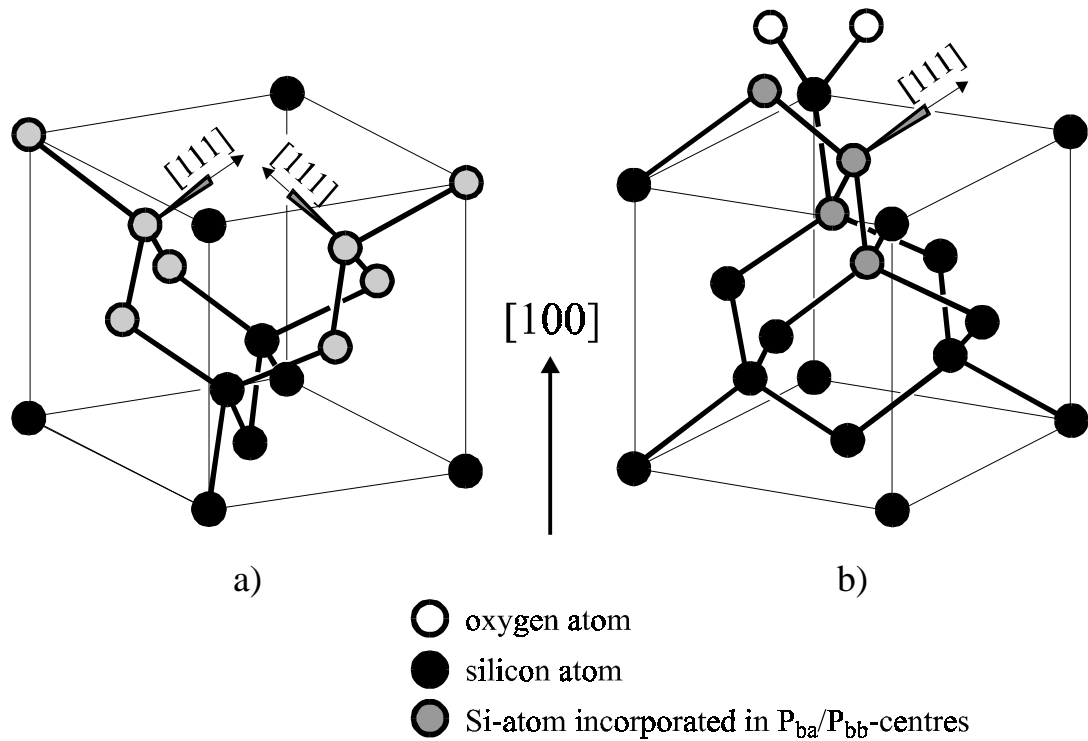


Fig. 3.8 Suggested models for the dangling bond defects detected in this work at and below a (100)Si/SiO₂ interface. Two of the four possible sites of the P_{ba}-centre in the bulk material are depicted in a). In b) one of the four possible sites of the P_{bb}-centre at the Si/SiO₂ interface is shown. To simplify the understanding only two additional oxygen atoms, indicating the SiO₂ part of the crystal, are inserted in b). The arrows pointing along [111] direction indicate the dangling bonds due to Si-vacancies. It is noted that the Si-lattice is rotated by 90° about the [100] axis for b) respective to a).

ergy Si-atoms. It also explains the weakness of the EDEPR signal detected after annealing only or low energy implantation. In figure 3.8 selected sites are shown of the suggested structures of P_{ba} - and P_{bb} -centres in a silicon crystal oriented along [100].

The presence of dangling bonds implies the presence of vacancies (V_{Si}) in the lattice which are created by the implantation. It is known for n-type silicon samples that the V_{Si} heal out even at room temperature. Thus it is to question why dangling bonds are observable after long term annealings at high temperatures as found in this study. It is noted that the sample used in this investigation was boron-doped with a concentration of $n(B)=2 \cdot 10^{15} \text{ cm}^{-3}$. For similar samples Awadelkarim et al. observed a high thermal stability of radiation defects (dangling bond type) even for long term annealings at 400°C [Awadelkarim 1989]. Their results indicated that the defects are trapped by boron which

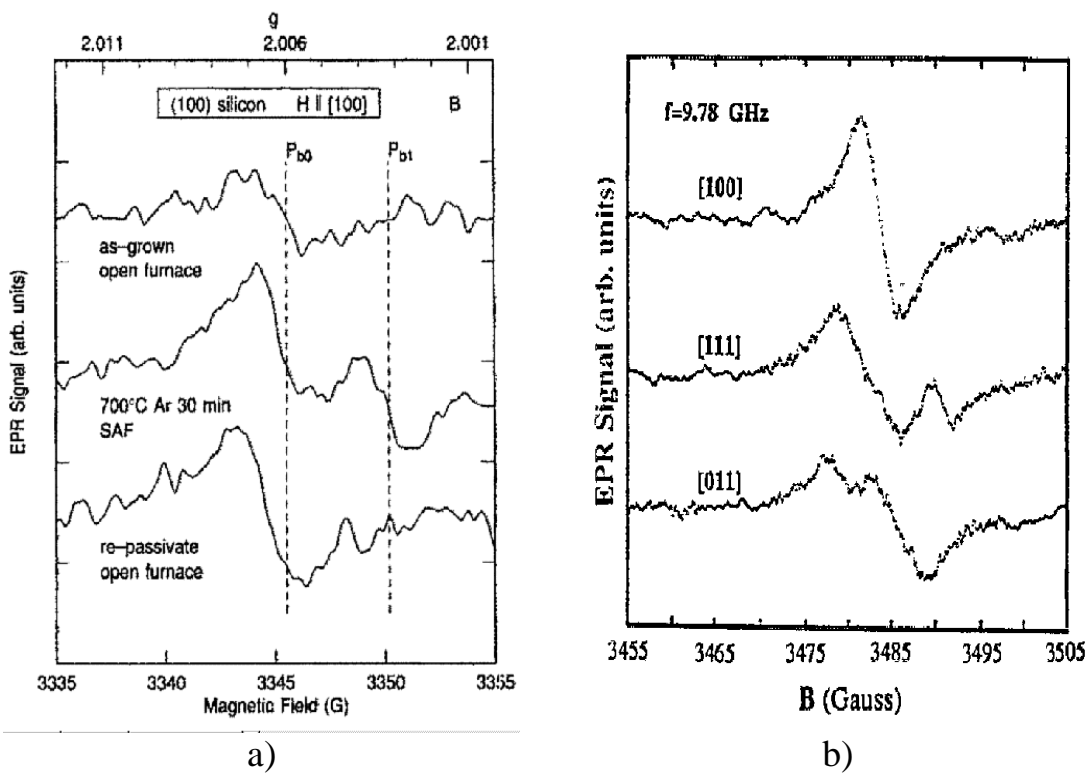


Fig. 3.9 Room temperature X-band EPR spectra of P_b -centres at the (100) Si/SiO_2 interface. In a) spectra of the P_b -centres after various preparation steps published by Stathis et al. are shown [Stathis 1991]. In b) three spectra of the P_b -centre studied by Mao et al. are given depicting the main crystallographic orientations [Mao 1993].

can explain the observation of the P_{ba} and P_{bb} centres in this study.

When comparing the two atomic models of the P_{ba} and P_{bb} centres presented in figure 3.8 their similarity in structure is obvious. Both are of tetrahedral form and consist of four silicon atoms on their regular lattice sites. However, a significant difference in anisotropy is found for P_{bb} and P_{ba} . The increased anisotropy for P_{bb} can be explained by the strongly distorted crystal field in the Si/SiO₂ interface. For examples reconstructions of the silicon crystal occur at this interface which can show a strong mismatch of the lattice parameters. Since the *g*-value is strongly influenced by the crystal field, the perturbed surrounding of the P_{bb} , compared to the idealised perfect cubic one of the P_{ba} , is responsible for the increased *g*-factor anisotropy.

There is only a very limited number of publications with values for *g*-factor anisotropy of the dangling bonds centres. The reason is probably the poor signal-to-noise ratio of the spectra recorded at Si/SiO₂ interfaces. Nevertheless, the values available are in the range of $g_{\perp} = (2.0012 - 2.0023)$ and $g_{\parallel} = (2.0081 - 2.0090)$ [Caplan 1979][Stesmans 1986][Mao 1993], thus the data obtained for P_{ba} in this work are in good agreement with those published so far.

In the work of Mao et al. crystalline silicon was heavily anodised in strong HF solutions in order to create porous silicon layers of a thickness up to 120µm. Their room temperature EPR measurements revealed a weak dangling bond signal, which was attributed to a trigonally symmetric angular pattern after decomposition and computer simulation. The resonances were supposed to arise from crystalline phase particles within the porous layer. The Si-surface/interface structure prepared by Mao et al. is probably comparable to the one created by high-dose high-energy implantation. Therefore, because of the good agreement between the *g*-values presented by Mao et al. and this work (see Tab. 3.1) an identification of both centres with P_{b0} is tempting.

Spectra of P_b -centres obtained in this work with those presented in literature shall be compared, selecting the works of Stathis and Dori and Mao et al. Both groups have carried out room temperature EPR measurements and find dangling bond related signals. In figure 3.9.a EPR spectra of the two centres P_{b0} and P_{b1} detected by Stathis and Dori are shown for an orientation of $\vec{B} \parallel [100]$. No details about an angular dependence of the resonances are given by the authors. The *g*-factor of 2.0060 determined by Stathis et el. for $\vec{B} \parallel [100]$ is very close to the one presented in this work for the P_{ba} centre, $g=20062$. From the EPR spectra presented in figure 3.9.b by Mao et al. determined a trigonal symmetry of the *g*-tensor. The signal-to noise ratio and the spectral resolution are poor

in both publications, but the spectral range of the group of resonances in both publications is comparable with the one of the P_{ba} centre of this work.

In summary the simultaneous detection of two trigonal dangling bond centres at and below a (100) Si/SiO₂ interface is reported for the first time. It is noted that the detected dangling bond centre P_{ba} is very similar to the P_{b0} defect reported in the literature [Caplan 1979][Stesmans 1986][Mao 1993]. The P_{b0} centre is related to implantation damage below the Si/SiO₂ interface, leading to dangling bonds within the bulk material. When assuming a positive identification of P_{ba} with P_{b0} the result underlines the observation that the P_{b0} centre is generated by particle radiation [Vranch 1988]. However, the identification of the P_{ba} centre found here with the known P_{b0} center must remain somewhat speculative.

The more anisotropic P_{bb} centre can be attributed to dangling bonds at the (100) Si/SiO₂ interface, occurring after annealing or low energy particle implantation. The EDEPR signal of the P_{bb} centre can be increased by annealing in an oxygen containing atmosphere. The P_{bb} centre has been detected for the first time due to the increased sensitivity and low noise figure of low temperature EDEPR measurements.

Chapter 4

Oxygen related defects in silicon

The need to understand the behaviour of oxygen impurities in silicon is caused by the requirements of device fabrication. Infrared absorption measurements have shown that isolated oxygen atoms occupy interstitial sites in the lattice. Their absorption lines enable the estimation of the oxygen concentration in the specimen. After heat treatment cycles oxygen precipitation has been observed by several methods (EPR, ENDOR, DLTS, FTIR, PTIS). The defects created as a consequence of heat-treatment are called thermal donors in general. According to the temperature and duration of the annealing different families of thermal donors can be distinguished. Annealing at high temperatures ($T \geq 600^{\circ}\text{C}$) gives rise to the so called “New Donors” (ND). At intermediate temperatures ($450^{\circ}\text{C} \leq T \leq 550^{\circ}\text{C}$) the most prominent oxygen clusters develop which appear with a double donor characteristic and are called “Thermal Double Donors” (TDD). After long term annealing at these intermediate temperatures, oxygen clusters labelled “Shallow Thermal Donors” (STD), which can be singly ionised, develop additionally.

Several elements which can be present in or added to the crystal have been investigated regarding their interaction with oxygen. Some of these elements enhance the formation of oxygen precipitates, such as hydrogen (H) whereas the formation of TDD is suppressed by high concentrations of carbon (C), for example.

This chapter is presented to provide a general survey of the oxygen-related defects in silicon. The STDs are studied in detail in chapter 5 whereas the results of EDEPR measurements of TDDs are discussed in chapter 6.

The radiation-induced A-centre, introduced in this chapter as well, plays an important role not only for the STDs and TDDs but for the mechanism of EDEPR as well.

4.1 Oxygen in silicon – an introduction

For the fabrication of silicon single crystals two different processes can be applied. One of them makes use of a polycrystalline silicon rod which is pulled through a high frequency (HF) coil. With sufficient HF power the silicon heats up to 1420°C and is transferred into a single crystal in a “float zone” manner, the process giving the name for this material (FZ-silicon). The single crystals gained by this method excel themselves as highly pure with contamination of less than 0.5ppb.

Silicon crystals used for the fabrication of 90% of the integrated circuits are grown by the much less expensive Czochralski (Cz) technique. Ultra pure polycrystalline silicon is melted in a silica crucible at a temperature above 1400°C, a rotating seed crystal is dipped into the melt and then slowly withdrawn while the crucible is rotated in the opposite sense. Oxygen from the crucible enters the melt and oxygen is subsequently incorporated into the growing crystal at a concentration close to 10^{18}cm^{-3} ($\sim 10\text{ppm}$).

Oxygen in silicon is electrically neutral and occupies bond-centered interstitial sites, see figure 4.1 [Kaiser 1957]. Kaiser et al. found an infrared absorption band ($9\mu\text{m}$) correlated to the isolated O_i which is commonly used to determine its concentration in silicon crystals. Next to the ^{16}O band absorption lines corresponding to the isotopes ^{17}O and ^{18}O (natural abundance 0.04% and 0.2%, respectively) can be found with infrared spectroscopy. An example for a low temperature (7K) FTIR measurement of an ^{17}O enriched sample is given in figure 4.2.

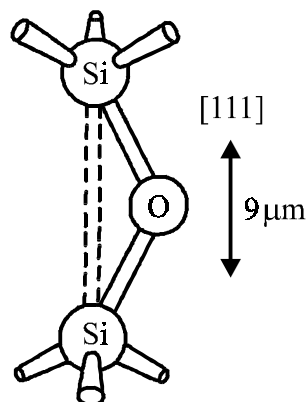


Fig. 4.1 Interstitial site of oxygen in the silicon lattice. The arrow indicates the direction of the localised vibrational mode (LVM) of the oxygen atom.

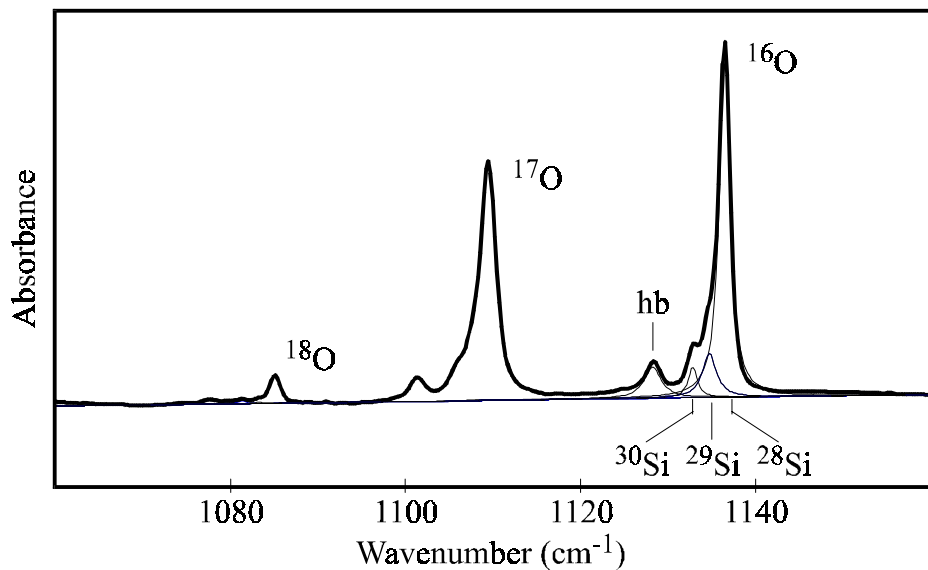


Fig. 4.2 FTIR spectrum of Cz-silicon enriched with ^{17}O . Inserted in the range of the dominant ^{16}O absorption are computer simulations of lines that are due to the interaction of the interstitial O with the three silicon isotopes. The label “hb” stands for hot bands and is explained in the text.

The FTIR spectrum shows three significant peaks which are due to the three isotopes of oxygen. Each IR line has two satellites on its low energy side with separations of 1.9cm^{-1} and 3.8cm^{-1} , respectively, due to O_i atoms with various combinations of neighbouring ^{28}Si (92.3%), ^{29}Si (4.7%) and ^{30}Si (3%) isotopes [Pajot 1967]. Each of the dominant lines is also accompanied by a line of lower energy, called “hot band” (hb). These hot lines were attributed to transitions from thermalised levels close to the ground state which are due to the splitting of the vibrational levels. The splitting is explained by the orientational degeneracy of the O atom between equivalent sites in the crystal [Hrostowski 1960].

4.2 Thermal Double Donors

In 1955 Fuller et al. observed an increase of the donor concentration in silicon after heat treatment cycles in the temperature region of 450°C [Fuller 1955]. The incorporation of oxygen in this defect was examined by Kaiser et al. later [Kaiser 1957]. The formation of these defects is attributed to the sequential clustering of oxygen atoms and at least 16

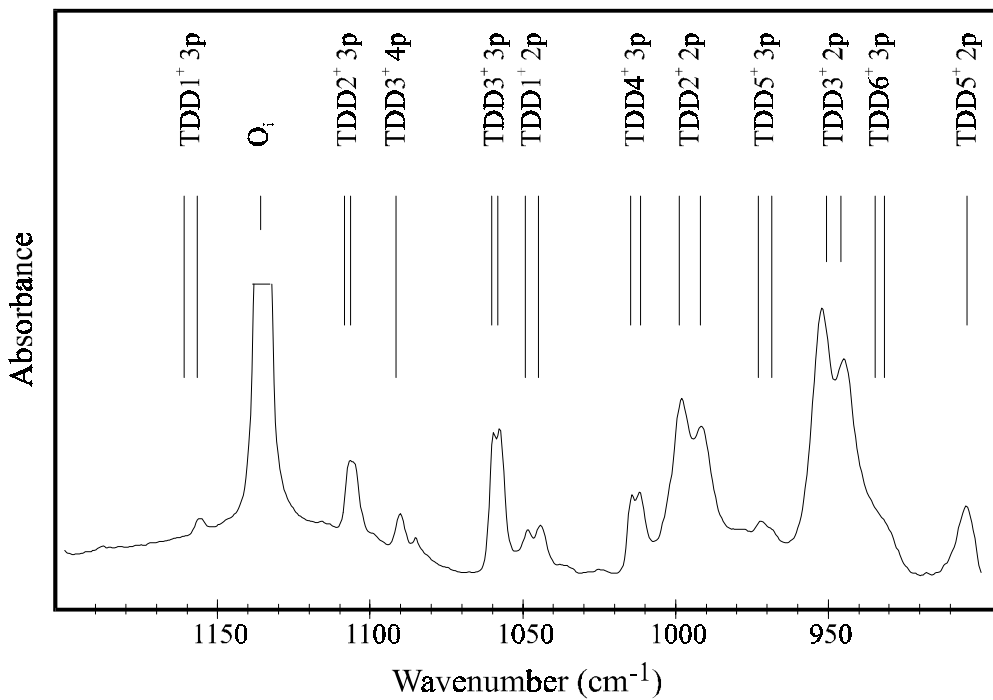


Fig. 4.3 FTIR spectrum of Cz-silicon after 12hours heat treatment at 450°C. The absorption lines are due to electronic transitions of singly ionised TDD^+n .

discrete centres ($1 \leq n \leq 16$) have been resolved by IR measurements, with n increasing with annealing time [Wagner 1989, Götz 1992]. Each centre is a shallow helium like double donor according to effective-mass-theory (EMT), that gives rise to sharp electronic absorption lines from the ground state ($1s$) to the excited states ($2p_0, 2p_{\pm 1/h}, 3p_0$ etc.). They appear in the range of ($533 - 350$) cm^{-1} at 4.2K where the donors are in their neutral charge state. If the annealed silicon also contains acceptors such as boron, it will be partially compensated. The singly ionised centres, TDD^+n , give rise to electronic transitions in the range ($1170 - 580$) cm^{-1} , see figure 4.3 [Wagner 1989].

In EPR the TDD^+n centres cause the so called NL8 spectrum, consisting of four strongly overlapping lines corresponding to a C_{2v} -symmetry. The NL8 spectra show progressively shifting g-values and decreasing anisotropy with increasing annealing temperature. The observations are attributed to the simultaneous presence of overlapping, unresolved resonance lines due to adjacent TDD^+n species [Muller 1978] [Dirksen 1999]. ENDOR measurements reveal the presence of ^{17}O in diffused samples containing a high concentration of this isotope with nuclear spin of $I=5/2$ and a quadrupole moment, whereas ^{16}O and ^{18}O show no nuclear spin [Michel 1989]. The results show an

increasing intensity of the ENDOR transitions with increasing n , providing evidence that the number of O atoms incorporated also increases. The same authors revealed a highly anisotropic structure of the TDDs with a line of O atoms along a [110] direction. The structure of the core is still a matter of controversial debate, as can be outlined by the following two citations. A model by Deák et al. indicates that a mobile interstitial Si atom is trapped and forms dative bonds with two trivalent O_i atoms in the donor core [Deák 1992]. However, first principles calculations by Chadi imply that vacancies or self-interstitials can not be present in the core [Chadi 1996]. A model of the TDD atomic structure as proposed by Deák is shown in figure 4.4 [Deák 1992].

A recent model for the formation kinetics of the TDDs demonstrates the sequential dissociation of early species of oxygen clusters in favour of the creation of higher species that show increasing stability with increasing size (increasing n) [Götz 1998]. This model supposes that no further loss of O_i should appear as the re-arrangement of the TDD towards larger clusters takes place. The model also implies that a TDD_n centre is transformed into a TDD_(n+1) centre by the addition of two O atoms (a dimer), rather than one atom, to one end of the oxygen chain aligned along the [110] direction. Such growth must be responsible for the unusual sequential changes of the measured ionisation energies E_i of the individual TDD_n [Götz 1992]. The E_i decreases with a “staircase structure” [Götz 1992] as n increases, implying the existence of two types of centres.

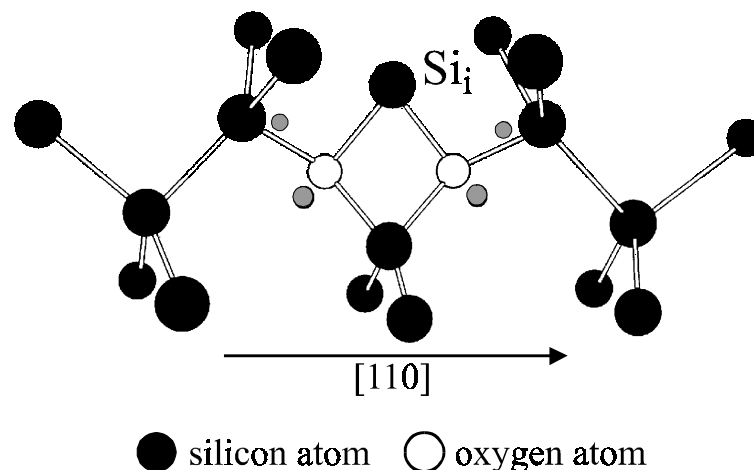


Fig. 4.4 Atomic model of the core structure of the TDDs as proposed by Deák. Unperturbed lattice positions are marked by small grey circles. Besides electrons present in bonds and lone pair orbitals, two electrons are in a delocalised orbital so that the complex is a shallow double donor [Deák 1992].

High resolution EPR and ENDOR measurements of the NL8 spectrum have confirmed that adjacent members have alternating C_{2v} (orthorhombic I) and C_s (monoclinic I) symmetries, as n increases to $n+1$ [Dirksen 1999]. It follows that the extra O_i atom (or O_2 dimer) must be added sequentially to alternate ends of the existing chain or that the core structure is re-located due to local diffusion jumps. A simulation of an angular dependence for NL8 EPR spectra is given in figure 4.5.

A strong enhancement of the TDD formation has been found by Brown et al. after exposing the Cz-silicon specimen to H plasma during the heat treatment cycle [Brown 1988]. By means of high resolution FTIR measurements Newman et al. proved that hydrogen is not incorporated in the TDD [Newman 1996]. As a possible conclusion of both findings an enhanced oxygen diffusion in the presence of hydrogen during heat treatment has to be assumed.

Finally, due to the results of very specific approaches to IR absorption lines of TDD_n centres a bi-stability of the TDD1 and TDD2 has been postulated [Hallberg 1996] but could not be supported and analysed in EPR.

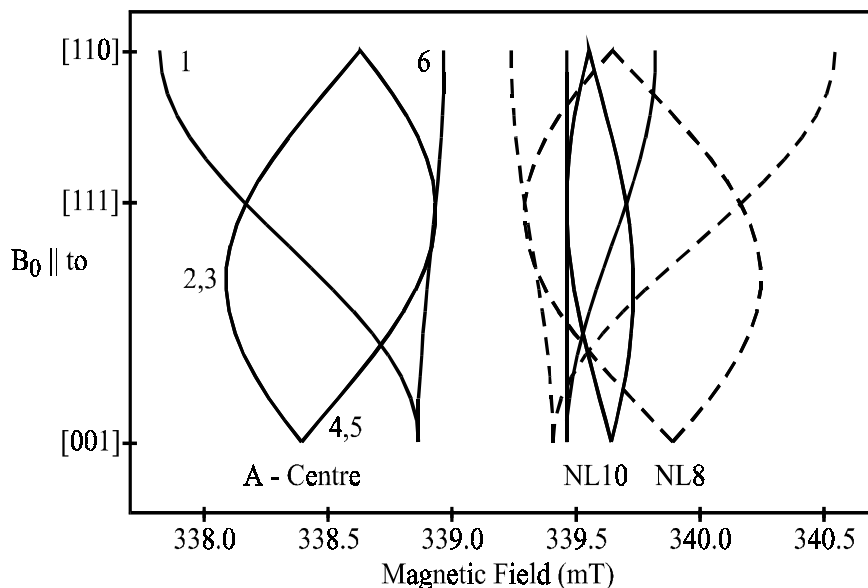


Fig. 4.5 Calculated EPR angular dependence of A-centre-, NL8- and NL10-spectra for a fixed microwave frequency ($v_{MW}=9.5\text{GHz}$) and g-tensors as given in table 4.1. The sample was rotated in a $[1\bar{1}1]$ -plane. The numbers in the pattern of the A-centre indicate the six centre orientations of the C_{2v} symmetry of the defect.

4.3 Shallow Thermal Donors

Next to the NL8 spectra further resonances labelled NL10 can be found in EPR if the heat treatment around T=450°C is significantly prolonged. The NL10-centres are related to “Shallow Donor Centres”, STD n , seen in IR absorption measurements in the range of (150-300)cm⁻¹ [e.g. Gregorkiewicz 1988]. The spectra of NL10 are less anisotropic compared to the ones of NL8 (figure 4.4). The centres were first detected by photo-thermal ionisation (PTIS) and absorption spectroscopy of Cz-Si preannealed in oxygen gas and then heated at T≤500C°. The donor ionisation energies of (30–40)meV correspond to the values predicted by effective mass theory (EMT), thus STDs are shallower than TDDs. ENDOR spectra of ²⁹Si demonstrate that the extended [110] structure of the NL10 defects is similar to that of NL8 centres, a similarity also observed for the ¹⁷O ENDOR [Ammerlaan 1996, Spaeth 1996].

Several groups of these single donors depending on further impurities involved in the STDs are known. At least three families can be distinguished by the elements contributing to the formation of the STD n . For STD(Al) n it has been shown with ENDOR that an aluminium atom (²⁷Al, (100% : I=5/2) is incorporated in the core of the defect [Gregorkiewicz 1988, Meilwes 1993]. Further, the structure of the NL10 in Al-doped silicon alternates between C_{2v} (orthorhombic) and C_S (monoclinic) symmetry for adjacent species as it does for TDD⁺ n .

For a second family of STD, labelled STD(H) n , the incorporation of hydrogen (H) is revealed by a shift of IR absorption lines towards lower energies (~0.1cm⁻¹) when H is replaced by deuterium (D) in the preannealing process [Newman 1998]. The frequen-

Defect	Spin	$g_1 \parallel [001]$	$g_2 \parallel [110]$	$g_3 \parallel [-111]$
NL8 ^a	½	1.99991	1.99323	2.00091
NL10 ^a	½	1.99959	1.99747	1.99957
A-centre ^b	½	2.0029	2.0096	2.0019

Table 4.1 Values of the g-factor for relevant oxygen-related paramagnetic defects as given by a) Muller et al. [Muller 1978] and b) Bemski [Bemski 1959].

cies of the IR absorption lines are different from those recorded of STD(Al)*n* and the change in ionisation energy E_i when passing from $1 \leq n \leq 5$ for STD(H)*n* is only ~50% of that for the shallow donors incorporating Al. The incorporation of hydrogen in silicon during crystal growth is proven by the identification of several IR absorption lines of as-grown samples [McQuaid 1994] with the known STD(H)(1-3) in hydrogenated samples. Further, Martynov et al. found H-related ENDOR resonances in Al-doped samples although the specimen had not been H-doped deliberately [Martynov 1995].

Several further shallow donors gives rise to IR absorption lines that are grouped to the family STD(X)*n* where the element or elements participating in the defect are not clear yet. Their transition frequencies are nearly indistinguishable from those gained by PTIS of samples doped with nitrogen (N) during crystal growth or preannealed in N₂ atmosphere. Still there is no direct evidence to identify X with nitrogen and it is suggested that vacancies diffusing from Si₃N₄ surface layers with a concentration of approx. 10¹⁴cm⁻³ during nitridation are involved in the STD(X)*n* [Newman 1996].

Alternatively, these vacancies can be caused by radiation damage [Watkins 1965]. The IR spectroscopy results are very close to those of STD(H)*n* yet a small but reproducible shift proves a different origin.

4.4 Radiation defects with participation of oxygen

The most prominent oxygen related defect occurring only after electron- or γ -irradiation of silicon crystals is a vacancy-oxygen complex labelled A-centre [Watkins 1959, Bemski 1959]. Its electronic structure was studied with ENDOR by van Kemp et al. [van Kemp 1986]. The singly negative charged paramagnetic state (V–O)[−] shows an orthorhombic symmetry and is stable in n-type silicon. In figure 4.5 a simulation of an angular dependence is given. The excited neutral triplet state of the A-centre, (V–O)^{0*}, with an electron spin $S=1$ is called SL1-centre. It can only be detected after and during illumination with above-band-gap light. It is created by the recombination of free charge carriers at the (V–O) complex. The SL1-centre is easily detected in EPR as well as in EDEPR.

It has been shown recently that the formation of STD can be increased strongly by electron irradiation of the silicon samples and thus creation of radiation defects prior to annealing [Markevich 1998].

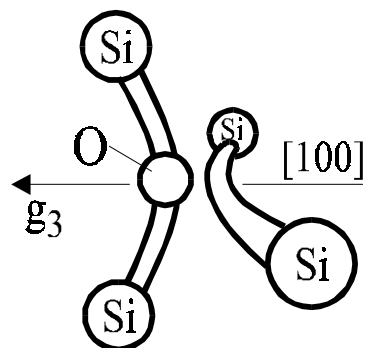


Fig. 4.6 Model for the Si-A centre depicting it as a vacancy trapped at an interstitial oxygen atom.

Chapter 5

Magnetical and optical studies of shallow thermal donors in hydrogen-ated Cz-Si crystals

Three species of a shallow donor family (D1–D3) have been observed previously by means of infrared absorption measurements in hydrogenated Czochralski-grown Si-crystals [Markevich 1994]. They appear after irradiation with fast electrons and subsequent annealing in the temperature range of (300–550)°C.

In this chapter the results of an optical (FTIR) and magnetic resonance study (EPR, EDEPR, ENDOR) of the D1–D3 shallow donors are presented. Hydrogen incorporation into the D1 and D2 centers is found by the observation of resonance lines due to hyperfine (hf) interactions of an unpaired electron with the ^1H and ^2H nuclei in ENDOR spectra. Parameters of the hf-tensor are determined from the analysis of angular dependencies of the ENDOR lines. The observed EPR and ENDOR signals are compared with those due to Si-NL10(H) shallow thermal donors published previously and possible atomic structures and formation mechanisms of the defects are discussed.

5.1 Introduction

In order to introduce the family of shallow donor centres forming with the participation of hydrogen, STD(H)*n*, the published data presented in chapter 4 are summarised. Upon heat treatment of oxygen-rich silicon at approx. 470°C two oxygen related defect centres show distinguishable absorption lines in FTIR and PTIS. The centres labelled TDD and STD develop after annealing times of $t \approx 0.5\text{h}$ and $t > 10\text{h}$, respectively. The STDs appear with absorption bands in the range of (300–150)cm⁻¹ and corresponding ionisation energies of (34–40)meV [e.g. Navarro 1986]. After such heat treatments of Cz-Si two defect centres are found in EPR as well, and are called NL8 for $t \approx 0.5\text{h}$ and NL10 for $t > 10\text{h}$, respectively. The oxygen incorporation in the centres has been proven by ENDOR [Gregorkiewicz 1987][Michel 1989].

Several features (e.g. formation kinetics) indicate an identification of the TDDs, found in FTIR, with the NL8 defects and of the STD with the NL10 centres [e.g. Newman 1996]. The labelling of the centres is sketched in table 5.1.

The defects occurring after prolonged annealing ($t > 10\text{h}$) can be divided into several families depending on the additional doping of the Si. Each of them is specified by a distinctive set of absorption lines in FTIR. Three families of STDs have been established so far: the STD(H) (incorporating hydrogen), the STD(Al) (incorporating aluminium), and the STD(X) (incorporation of nitrogen or lattice vacancies). The impurities incorporated in the centres have been detected using FTIR and ENDOR [Newman 1998][Martynov 1995][Meilwes 1993]. In recent years the strong effects of hydrogen in silicon have triggered intense studies of hydrogen related defect centres, such as the STD(H). The participation of hydrogen in this defect was proven by isotopic shifts of electronic absorptions after exchanging hydrogen by deuterium [Newman 1996]. An enhanced formation of STDs after hydrogenation of nominally nitrogen- and aluminium-free Cz-Si was found [Martynov 1995].

	FTIR		EPR
$t \approx 0.5\text{h}$	TDD	\Leftrightarrow	NL8
$t > 10\text{h}$	STD	\Leftrightarrow	NL10

Table 5.1 Formation conditions and labelling of the corresponding heat treatment centres detected by optical and magnetic resonance methods.

Two models describing the STDs(H) have been presented so far. In one model an incomplete passivation of the NL8 is claimed resulting in a single donor centre NL10(H) / STD(H) instead of a double donor [Martynov 1995]. A theoretical study yielded a C_i-H-2O_i complex with a single donor character [Ewels 1996]. Several arguments and experimental findings support the latter model rather than the former one and will be discussed later.

A new family of shallow thermal donors was found occurring after hydrogenation and electron-irradiation of Cz-Si and subsequent heat treatment in the range of (300–500)°C [Markevich 1994][Hatakeyama 1997]. The centres labelled D1–D3 show enhanced formation kinetics compared to the conventional STDs(H). The advantages in studying the D1–D3 species compared to the STD(H)_n centers are worth mentioning. Usually several different species of the STD(H) family give rise to very similar EPR and ENDOR signals simultaneously, very much complicating the analysis of the EPR and ENDOR spectra [e.g. Gregorkiewicz 1988]. However, for the irradiated Si:O,H samples, it is possible to choose the annealing conditions such that only one particular donor species dominates the spectra. This provides a good opportunity for structural studies of one particular species.

Samples for this study were prepared from n-type ($N(P)=5\cdot10^{15} \text{ cm}^{-3}$) Czochralski-grown silicon with a resistivity of $\rho=1 \Omega\text{cm}$ and cut to dimensions of $3\cdot3\cdot15\text{mm}^3$. The oxygen concentration was estimated by FTIR absorption measurements to be $9.5\cdot10^{17}\text{cm}^{-3}$. The carbon concentration was under the detection limit of the optical absorption method ($\leq 1\cdot10^{16} \text{ cm}^{-3}$). Hydrogen (deuterium) was introduced into the samples by heat-treatments in H₂ (D₂) gas at 1200°C for 1h, terminated by quenching. Irradiation with fast electrons (3MeV) was performed at room temperature with a flux of $2\cdot10^{16}\text{cm}^{-2}$. The samples were subsequently placed in an evacuated quartz ampoule filled with argon and heat treated in the range of (100–500)°C. Isochronal annealing procedures were performed with 50°C steps for 30min each. Before optical and EPR measurements the samples were etched with CP4 (HNO₃ : CH₃COOH : HF) at 60°C in order to remove damaged surface layers and to obtain polished surfaces.

5.2 Electronic properties of the shallow donors D1–D3

A typical infrared absorption spectrum of a hydrogenated, irradiated and annealed ($400^{\circ}\text{C} / 30\text{min}$) sample is shown in figure 5.1. Two strong absorption lines arising from the primary dopant phosphorous are detected. Further, absorption lines due to three shallow donor centres are seen, which are called D1, D2 and D3 [Markevich 1994]. The subscript index ($0, \pm$) indicates the orbital quantum number. The indices are applied for shallow states of defect centres which can be described by effective-mass-theory (EMT). For further information the reader is referred to textbooks like [Alonso 1988].

To gain information about the formation of the D1-D3 heat treatment centres samples with various preparations have been studied. In figure 5.2 infrared absorption spectra of hydrogenated Cz-Si crystals are shown, which were either heat-treated at 470°C for 10 hours (spectrum a)) or electron irradiated and subsequently annealed at 470°C for 0.5 and 3 hours (spectra b) and c)), respectively. The spectra were measured at 10K with a resolution of 0.5cm^{-1} . Several donor absorption lines are observed in the range of ($180\text{--}250\text{ cm}^{-1}$). These lines are due to electronic transitions of heat treatment centres [Newman 1998]. It is found that the positions of some lines coincide in all samples studied.

Particularly, the lines due to donors labelled D2 and D3 in irradiated samples are at the

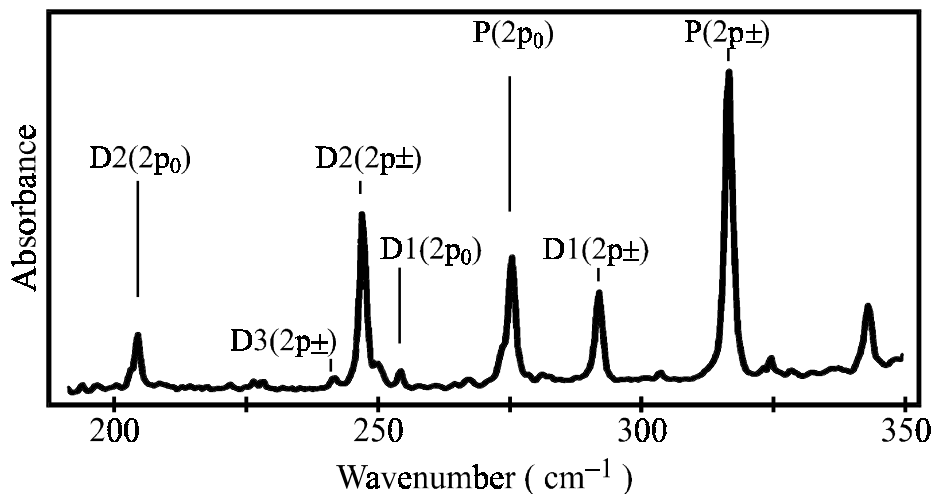


Fig. 5.1 FTIR spectrum of n-type Cz-Si after hydrogenation, electron-irradiation and subsequent annealing at 400°C for 30min. The sample was measured at 10K.

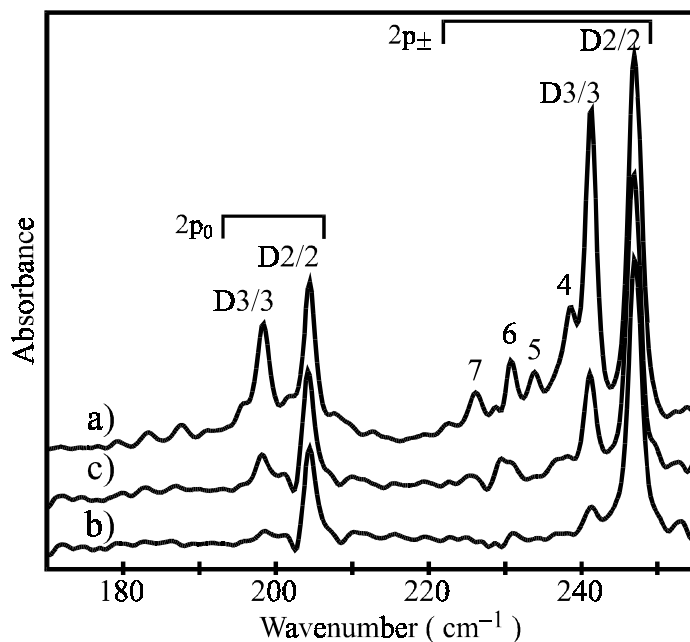


Fig. 5.2 Infrared absorption spectra ($T=10\text{ K}$) of the following hydrogenated Cz-Si samples: a) heat-treatment at 470°C for 10h, b) and c) electron irradiation at room temperature ($F = 2 \cdot 10^{16} \text{ cm}^{-2}$) followed by anneals at 470°C for 0.5 and 3 h, respectively. The numbers (1–7) indicate the number of the donor species of the STD(H) n family, according to [Newman 1998]. The D n indicate the donors according to [Markevich 1994].

same positions as the corresponding lines in the spectrum of the non-irradiated sample (204.3 and 246.9 cm^{-1} for D2 and 198.3 and 241.2 cm^{-1} for D3). These wave numbers are the same as those cited for the STD(H)2 and STD(H)3 centers by Newman [1998].

In table 5.2 the absorption line positions and the corresponding ionisation energies are listed for the D1–D3 centres. The values for D2 and D3 are compared with those obtained by Newman et al. for the STD(H)2 and 3 [Newman 1998]. The good agreement between the values confirms previous suggestions about the identity of the D2 and D3 donors and two centers of the STD(H) family [Markevich 1998][Newman 1998].

In figure 5.3 a study of the relation between the temperature of the heat treatment and the development of the D n centres is shown. The results were obtained after isochronal (30min) annealing of a hydrogenated and electron irradiated Cz-Si sample. The sample was measured with FTIR after each annealing step, starting at 275°C for 30min. The annealings were carried out with a temperature increased by 50°C each time. The procedure was continued up to a final temperature of 550°C . Depicted in figure 5.3 are the

Transition	D1	D2	D3	STD(H)2	STD(H)3
$1s \rightarrow 2p_0$ (cm^{-1})	249.7	204.3	198.3	204.2	198.2
$1s \rightarrow 2p_{\pm}$ (cm^{-1})	291.7	246.9	241.2	246.8	241.1
E_b (meV)	42.6	37.0	36.3	37.0	36.3

Table 5.2 Absorption line positions of the shallow donor centres D1–D3 investigated in this work compared to those published for STD(H)2 and 3 previously [Newman 1998].

intensities of the absorption lines due to $1s \rightarrow 2p_{\pm}$ electronic transitions as listed in table 5.2. The development of the individual species of this shallow donor family can easily be traced. Each donor can be prepared with a maximum intensity at one specific temperature.

Remarkable are the comparable signal intensities of D1 and D2 indicating an equal con-

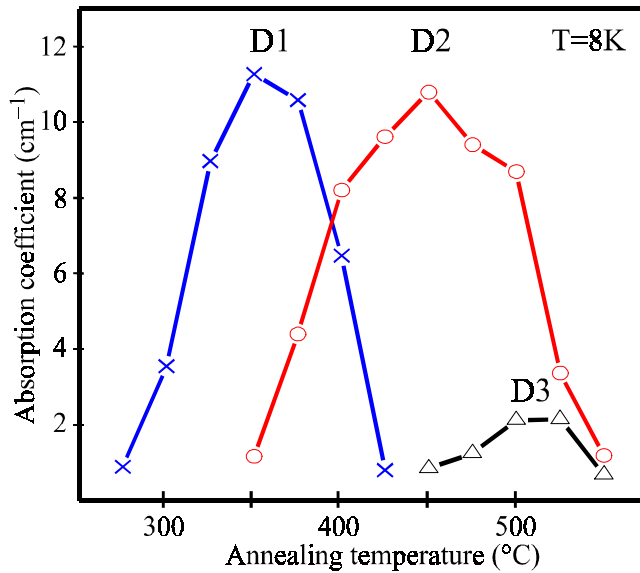


Fig. 5.3 Development of the intensities of the $1s \rightarrow 2p_{\pm}$ electronic transitions appearing at the absorption line positions listed in table 5.1. The sample was hydrogenated, electron-irradiated, and isochronally (30min) annealed with 50°C temperature increments. FTIR measurements were carried out after each annealing step. In the graph the absorption intensities are given for the corresponding annealing temperatures indicated on the abscissa.

centration of these centres. Only the D3 centre is formed with a reduced concentration compared to D1 and D2.

The necessity of both the hydrogenation and electron irradiation for the accelerated and increased formation of the D_n donors is underlined by the FTIR spectra presented in figure 5.4. They were recorded from samples that all had been annealed at 400°C for 30min as a final preparation step. The temperature was chosen in order to create both donors D1 and D2. The preceding preparation for sample a) was annealing at 1000°C in an inert gas ambience and electron irradiation, whereas sample b) was hydrogenated at 1000°C only. In both spectra a) and b) absorption lines due to electronic transitions of the primary dopant ^{31}P are also detected. Only after a preparation procedure including hydrogenation (1000°C), electron irradiation and final annealing new absorption lines due to the shallow thermal donors D1 and D2 arise. This strongly indicates the incorporation of hydrogen in the atomic structure of the D_n family. An incorporation of interstitial atoms, created by the irradiation of the sample, can be assumed tentatively from the FTIR results.

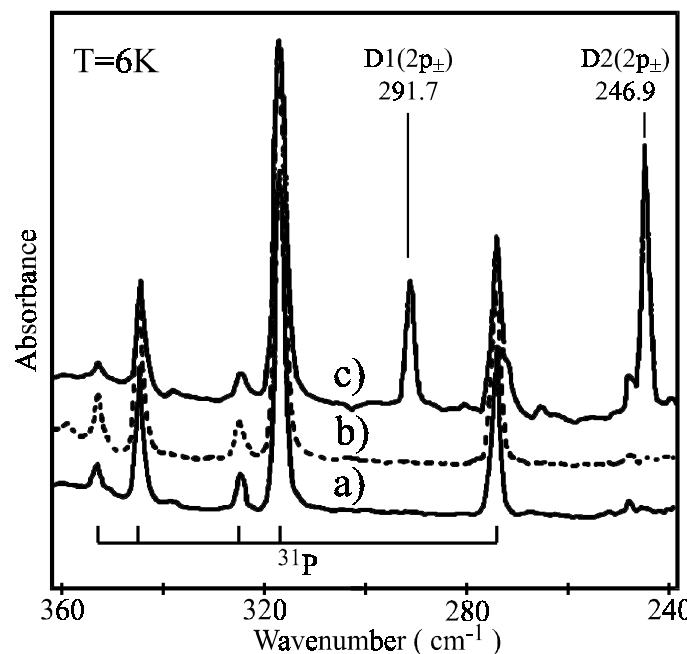


Fig. 5.4 Development of the infrared absorption line intensities of D1 / D2 and ^{31}P electronic transitions. All samples were finally annealed at 400°C for 30min. The precedent preparation was a) annealing in inert ambience at 1000°C and electron irradiation, b) hydrogenation at 1000°C, and c) hydrogenation at 1000°C and electron irradiation.

5.3 EPR investigation of the shallow donors D1–D3

The infrared absorption measurements presented above reveal that the D1–D3 centers develop sequentially upon isochronal annealing of irradiated Si:O,H samples in the temperature range (275–550)°C. The concentration of D1 centers reaches a maximum value at about 350°C and then decreases upon annealing at higher temperatures. After annealing at about 450°C the concentration of D1 is negligible, while the D2 species is the dominant one. Treatments at higher temperatures lead to a decrease of the D2 concentration with the simultaneous growth of the concentration of the D3 centers. To trace this development of the D_n centres by EPR is one of the intentions of the following section.

For all donors D_n a dependence of the EPR spectra on illumination of the sample is found. The feature is illustrated for the D1 centre in figure 5.5 as an example. Only a weak D1 EPR signal is detected next to ^{31}P resonances when the sample is cooled to measurement temperature (10K) in the dark. Upon white light illumination of the sample at 10K the D1 EPR resonance strongly increases (figure 5.5 b). This intensity remains when the light is turned off for the following measurements (c).The signal can only be suppressed by heating the sample to (50–60)K, followed by cooling to measurement temperature in the dark. Such changes in the signal intensity of the D1 centre had been observed previously with FTIR as well [Markevich 1994]. The results of EPR and FTIR reveal that the strong EPR signal is related to a metastable shallow donor state of the D1 centre. When the centre is cooled to the measurement temperature in the dark, the centre is transformed into the singly negatively charged stable state. Both the absorption of transitions in FTIR and the D1 EPR resonance line disappear. However, it is possible to recreate the FTIR lines and the EPR signal by illumination of the sample at low temperatures (6–10)K. No new EPR lines appear when the sample is cooled in the dark. Hence, the electrons at the $(\text{D1})^-$ state are paired.

Figure 5.6 shows the development of the EPR spectra, measured at 10 K, upon isochronal (30min) annealing of a hydrogenated and electron-irradiated Cz-Si sample. The same sample as used of the FTIR study presented in figure 5.3 is taken. Weak EPR signals are observed in the field range (323–324)mT after annealing at 300°C (figure 5.6, spectrum 1). According to their g -factor the signals are fingerprints of the radiation-induced A-centre (see chapter 4). After annealing at 350°C these signals are not observed any more, but the resonance line seen in figure 5.6 (spectrum 1), situated cen-

trally between the two lines due to ^{31}P is strongly enhanced. This intense EPR signal with a nearly isotropic g -factor of 1.9987 arises from the shallow donor D1.

Heat treatment of the irradiated crystals at temperatures higher than 350°C results in a transformation of the D1 to the D2 centers. This leads to the transformation of the isotropic EPR signal observed after annealing at 350°C to another one, the shape of which

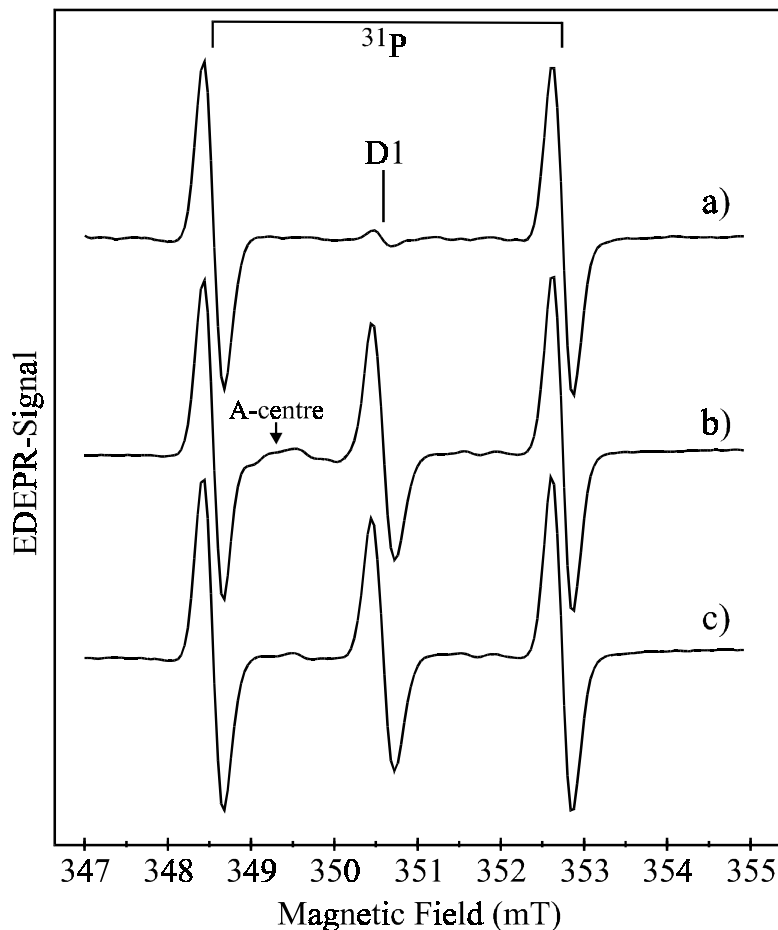


Fig. 5.5 Development of the intensity of the shallow donor resonance D1 upon illumination of the sample before/during measurement. The spectra have been recorded subsequently with the sample a) cooled in the dark to 10K, b) with subsequent illumination at 10K, and c) illumination turned off at 10K. In the range of (349–350)mT traces of the A-centre induced by irradiation of the sample appear in spectrum b). The sample was hydrogenated, electron-irradiated and subsequently annealed at 350°C for 30min prior to the above measurements. The spectra have been measured in X-band for $\vec{B} \parallel [110]$.

is characteristic for the defects with orthorhombic-I symmetry, C_{2v} point group (figure 5.6, spectra 3-5). The decrease in the concentration of the D2 centers and the appearance of the shallower D3 donors after annealing at 500°C leads to changes of the EPR signals.

The isotropic behaviour of the D1 signal and the orthorhombic-I symmetry of the D2 centre are confirmed by EPR measurements in K-band. The corresponding spectra are presented in figure 5.7.

On the basis of a slightly decreased spectral range of the D3 resonance lines compared to those of D2 a more isotropic g -tensor can be assumed. Recalling the results of the FTIR measurements it is found that the D3 donor is not created with a concentration as

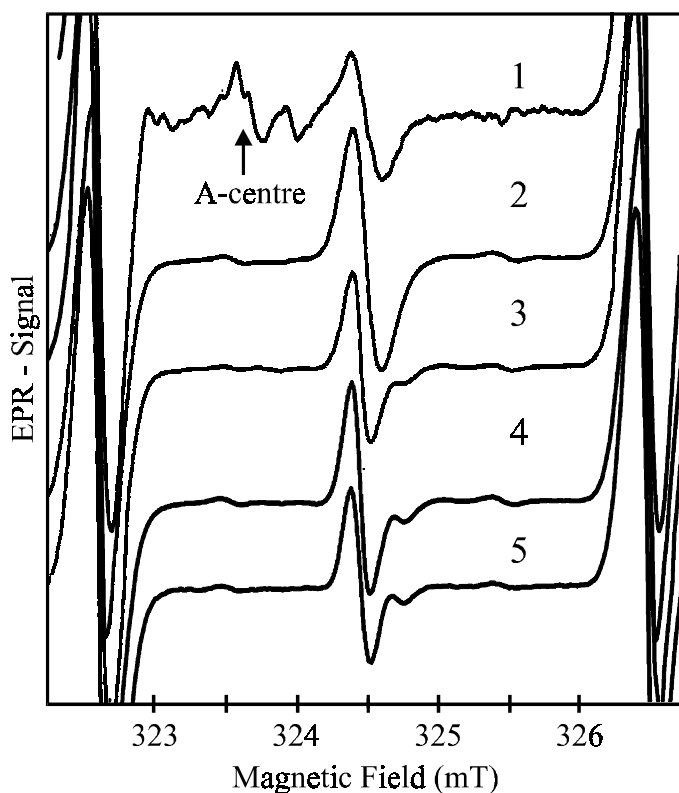


Fig. 5.6 Development of EPR spectra upon 30-min isochronal annealing of a hydrogenated Cz-Si sample which was irradiated with fast electrons ($2.0 \cdot 10^{16} \text{ cm}^{-2}$). Last annealing temperature, [°C] 1:300; 2:350; 3:400; 4:450; 5:500. The spectra were measured in X-band at 10 K for $\vec{B} \parallel [110]$. The spectra are normalised to the equal intensity of the signal due to ${}^{31}\text{P}$.

high as that of D1 or D2. Attempts to prepare D3 as the dominant shallow donor failed. This is in good agreement with findings by Newman [Newman 1998]. The IR absorption spectra presented there show as well a weak STD(H)3. Because of the low concentration and the strongly overlapping EPR signals no further investigation of the D3 centre was performed.

Figure 5.8 shows an angular dependence of the positions of four D2 EPR lines upon rotation in a $(1\bar{1}0)$ -plane. The solid lines represent the best fit to the data assuming that the lines are due to a defect with orthorhombic-I symmetry. The principal values of the g-tensor are determined from the fit as $g_1||[\bar{1}10] = 1.99952$, $g_2||[110] = 1.99722$ and $g_3||[001] = 1.99982$ ($\Delta g_n = \pm 0.00005$, obtained from EDEPR, section 5.4). These values are close to those usually quoted for NL10 centers ($g_1 = 1.99957$, $g_2 = 1.99747$ and $g_3 = 1.99959$, $\Delta g_n = \pm 0.00004$) [Muller 1978], but there is a small difference. The values of the D2 centre indicate a somewhat bigger anisotropy of this centre compared with the NL10 centers, with above values of g-tensor. The reason of this small difference is probably the higher value of the ionisation energy of the D2 centre compared to those of other species of the STD(H) family. According to Sieverts [Sieverts 1983] an increased

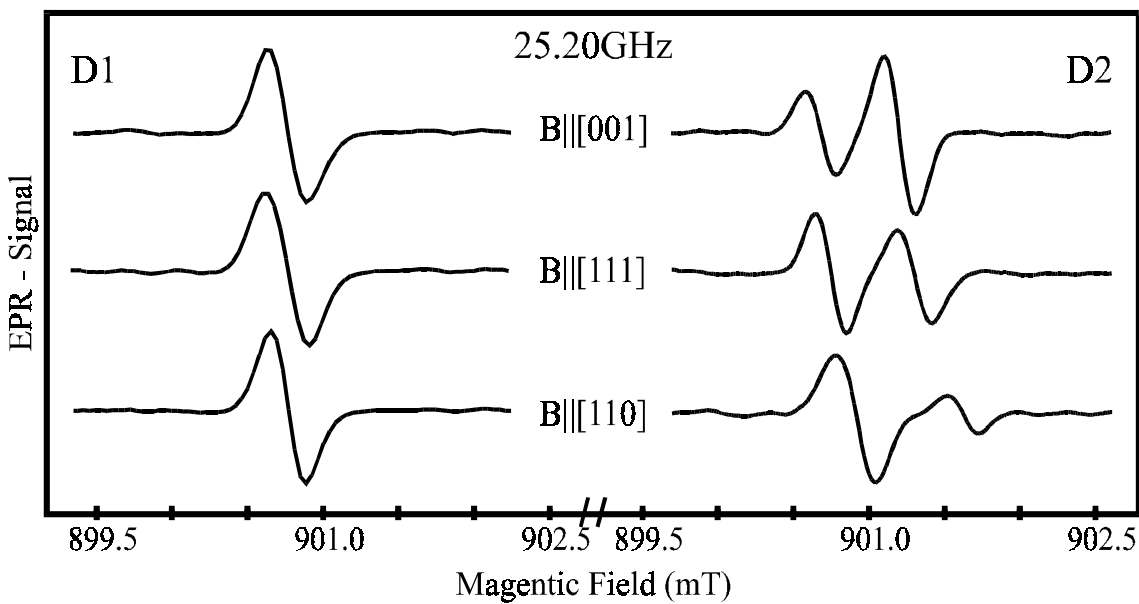


Fig. 5.7 Angular dependent K-band EPR spectra at 8K of a P-doped Cz-Si sample after hydrogenation, electron-irradiation and annealing at 450°C for 30min. The detected resonances appear upon illumination and are attributed to the shallow donor centre D1 and D2, respectively.

ionisation energy of a shallow donor results in a larger anisotropy of the corresponding EPR signal. In table 5.3 the g -values obtained for D2 in this work are compared with those presented for NL10(H) in literature.

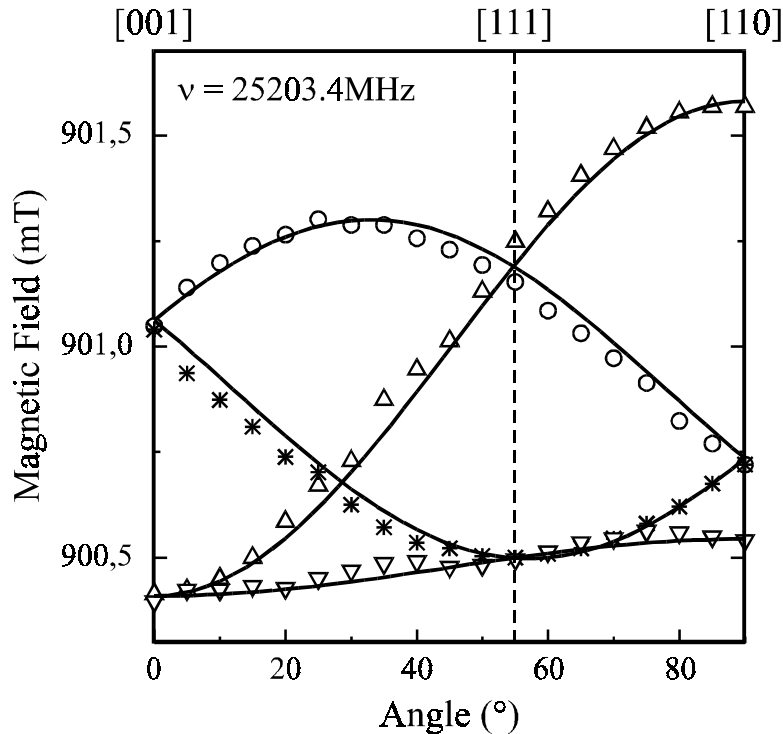


Fig. 5.8 Angular variation of the EPR lines due to D2 centres for rotation in a $(\bar{1}\bar{1}0)$ -plane. The angle “0” corresponds to $\vec{B} \parallel [001]$. The solid lines are calculated for a defect with $S = 1/2$, C_{2v} symmetry. The principal values of the g -tensor are listed in table 5.3.

	g_{xx}	g_{yy}	g_{zz}	symmetry	δ	ψ	ϕ	Refs.
D2	1.99952	1.99722	1.99982	rhombic-I	0	0	45	this work
NL10(H)	1.99957	1.99747	1.99959	rhombic-I	0	0	45	Muller 1978

Table 5.3 Principal values of the g -tensor of the shallow donor centres D2 ($\Delta g_n = \pm 0.00002$) investigated in this work compared to those published for NL10(H) ($\Delta g_n = \pm 0.00004$) centres previously [Muller 1978]. The high accuracy of the D2 g -values is achieved by the 72GHz EDEPR measurements. The angle δ is between the z-axis of the tensor and a [001] direction.

5.4 EDEPR investigation of the shallow donor D2

The EPR resonance lines due to the D2 shallow donor are overlapping strongly in the spectra measured in X-band (~9GHz) and even in K-band (~25GHz). In order to resolve them, higher microwave frequencies have to be utilised. Since a microwave bridge to detect the microwave absorption in a conventional EPR experiment was not available for frequencies higher than 25GHz, EDEPR as described in chapter 2 was used to realise measurements in V-band (~72GHz).

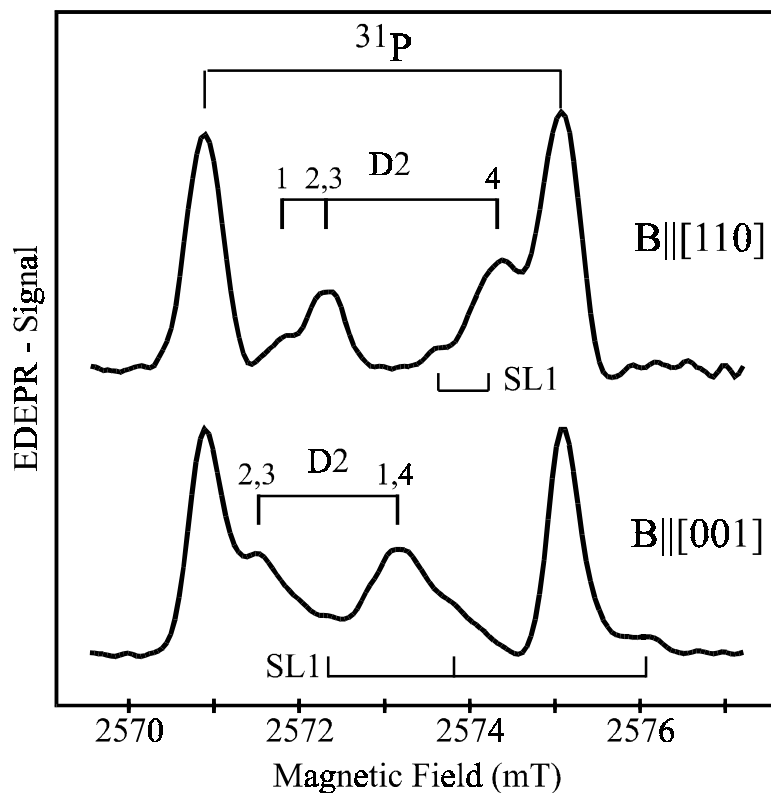


Fig. 5.9 EDEPR spectra of an electron-irradiated Si:O,H sample annealed at 450°C, measured at 10K using a microwave frequency and power of 72.2GHz and 150mW, respectively. The sample was illuminated with white light in order to create excess charge carriers and the EPR effect was detected monitoring a resistivity increase of the sample when applying a constant current of 6 μ A. The numbers 1-4 represent the centre orientations corresponding to the orthorhombic-I symmetry (figure 4.4). The tensor orientation is given in table 5.3. The contributions to the spectra by resonances due to the radiation-induced SL1 defect are indicated.

In figure 5.9 EDEPR spectra of an electron-irradiated Si:O,H sample after annealing at 450°C are shown. The angular positions for $\vec{B} \parallel [110]$ and $\vec{B} \parallel [001]$ have been chosen to demonstrate the increased separation of the individual resonance lines of the D2 centre between the ^{31}P -lines. The latter dominating lines are due to the hyperfine splitting of the sample's phosphorous doping and can be used as *g*-factor calibration markers as their SHF parameters have been determined precisely [Feher 1959].

Indicated in figure 5.9 is the labelling of the individual lines of the orthorhombic-I D2 centre. The analysis of the angular dependence measurements yielded the same *g*-tensor values already determined by fitting of the K-band data, but the precision of the values could be enhanced. It is noted that successful measurements of the shallow donor D1

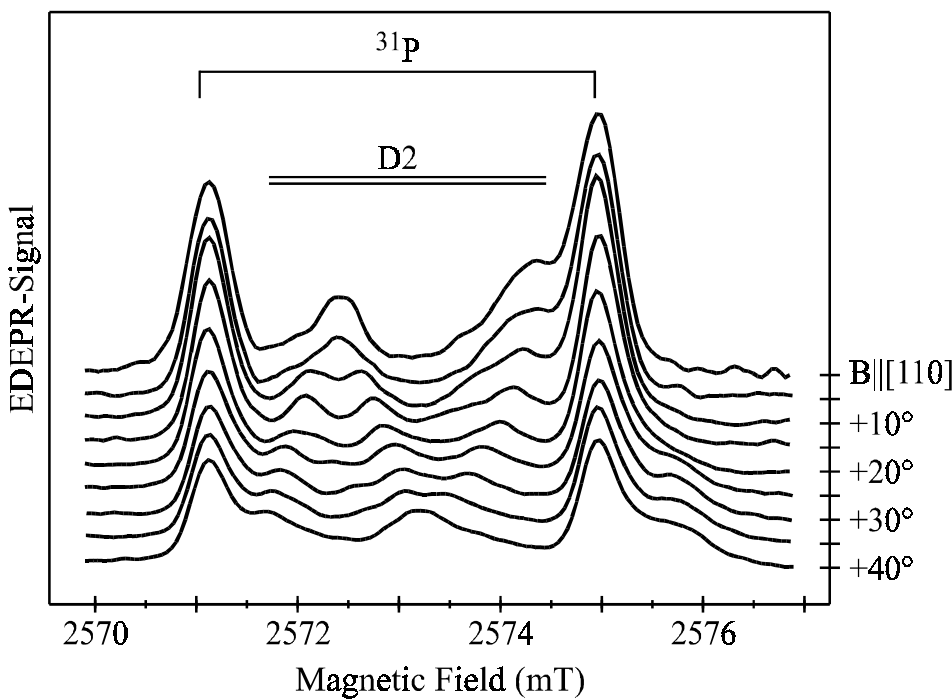


Fig. 5.10 Angular dependent EDEPR spectra of a P-doped Cz-Si sample after hydrogenation, electron-irradiation and annealing at 450°C for 30min. The dominant lines are caused by the primary dopant ^{31}P . In the range of (2571.5–2574.5)mT four resonance lines of the D2 centre appear. Additionally, traces of the radiation induced SL1-centre contribute to the spectra. The microwave frequency of 72.2GHz was square-wave amplitude modulated with 30dB/500Hz. No microwave resonator was used and the sample was illuminated with white light at T=6K.

were carried out as well. The spectra show again the isotropic character of the centre studied in K-band already and are not presented here again therefore.

In figure 5.10 more spectra of the V-band EDEPR angular dependence are shown. It is noted that EDEPR investigations with microwave frequencies as high as 72GHz have not been reported in the literature so far. Tests with a W-band microwave source (95GHz) were successful for the dominant ^{31}P -lines depicted in figure 5.9. Unfortunately, only very weak traces of the D2 centre could be revealed due to limited microwave power (<80mW).

More details about the EDEPR features and a discussion about the mechanism allowing to measure EDEPR of the donor centres are presented in chapter 6.

5.5 EPR investigation of shallow donor interaction with ^{29}Si nuclei

When taking a closer look at the spectra presented in figure 6.5 two additional, weak resonance lines can be detected next to those being caused by the ^{31}P atoms and the D1 centre. As the lines appear symmetrically about the D1 resonances it is tempting to assign them to satellite lines, arising from hyperfine interaction of the unpaired electron with ^{29}Si nuclei. The ^{29}Si is present with a natural abundance of 4.7% ($I=1/2$). In order to study these satellite lines in detail measurements with increased integration time were performed.

Figure 5.11 presents a D1 EPR spectrum which was recorded after cooling in the dark. It was subtracted from one recorded after previous illumination of the sample at low temperatures. Two satellite lines around the central line are clearly detectable in the inset. The ratio of the integrated area under the satellite lines to the total integrated area of all three lines is (4.7 ± 0.2)%. This value is in good agreement with one expected for one ^{29}Si -atom. From the angular dependence of the D1 satellite lines an isotropic hyperfine interaction with $a= (58\pm1)\text{MHz}$ is derived. The results obtained from angular and power dependent measurements of the D1 satellite lines are presented in figure 5.12. Similar ^{29}Si satellite lines with an intensity of (5.6 ± 0.2)% were observed for the D2 centre.

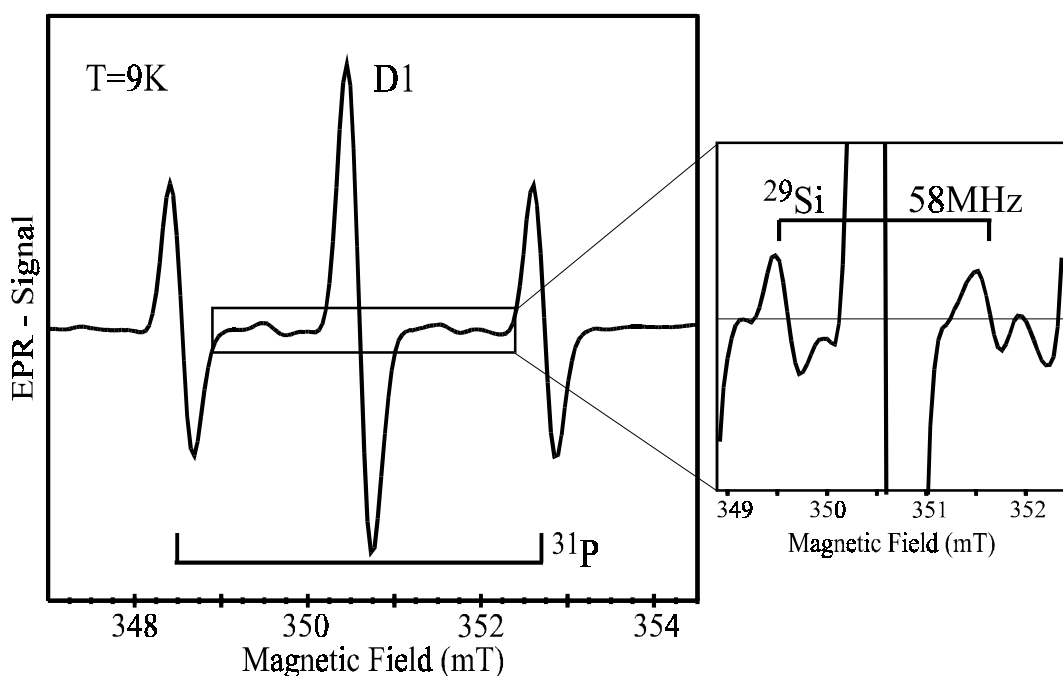


Fig. 5.11 X-band EPR spectrum of a hydrogenated, electron irradiated and finally annealed ($350^\circ\text{C}/30\text{min}$) Cz-Si sample. Further details are given in the text.

Centre	Preparation (°C / h)	Satellite- Ratio (%)	A (MHz)	E_b (meV)
D1	$\text{H}/\text{e}^-/(350/0.5)$	4.7	58	42.6
D2	$\text{H}/\text{e}^-/(450/0.5)$	5.6	70	37.0
NL10(H)	$\text{H}/(470/50)$	5.3	71	(34–40) ^a
NL10(Al)	Al-doping /(460/100)	1.7	52	–

Table 5.4 Values for the integrated area ratio of the satellite lines ($\pm 0.2\%$) and the hyperfine splitting ($\pm 1\text{MHz}$) listed with the preparation procedure and the corresponding ionisation energy of the shallow donor centres. The values for the ionisation energies for NL10(H) (a) are taken from [Navarro 1986].

A further Cz-Si sample was hydrogenated and annealed for 50h. The preparation gave rise to intense NL(H) resonances. Also for this sample a hyperfine splitting of the shallow thermal donor centre is observed for the first time. The data obtained are given in table 5.4. The intensity of the EPR satellite lines of 5.3% indicates an identification with

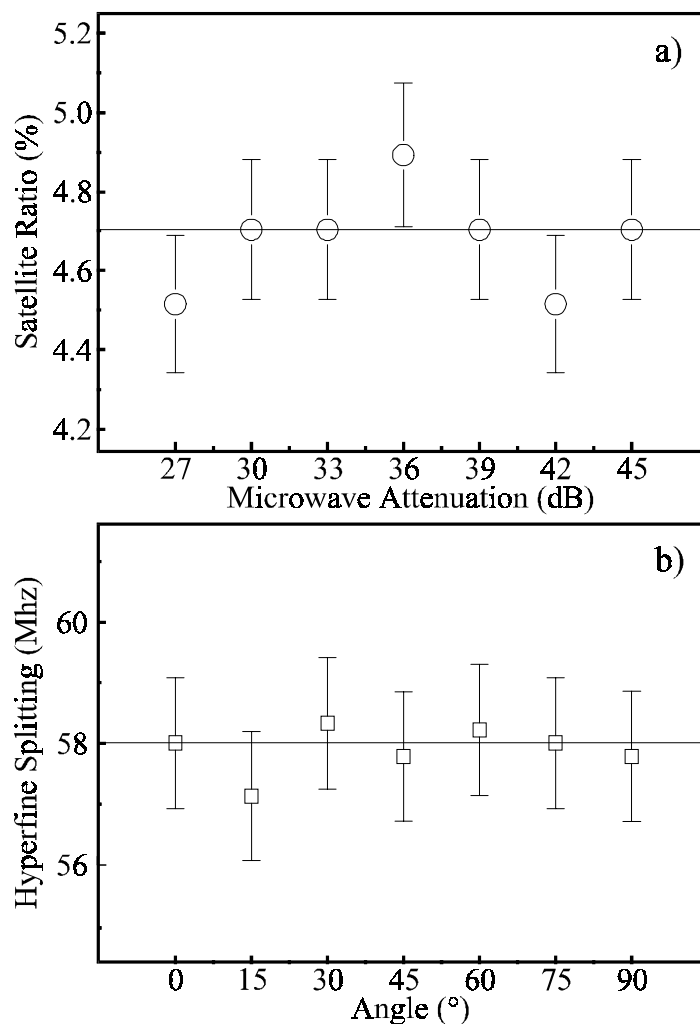


Fig. 5.12 a) Power dependence of the of the D1 ^{29}Si -satellite lines. The circles give the ratio of the integrated area under the satellite lines to the total integrated area under all three lines in dependence on the microwave power. b) The angular dependence of the hyperfine splitting of the D1 ^{29}Si -satellite lines for a rotation in the $(\bar{1}\bar{1}0)$ -plane is shown. The angle “0” corresponds to $\vec{B} \parallel [001]$.

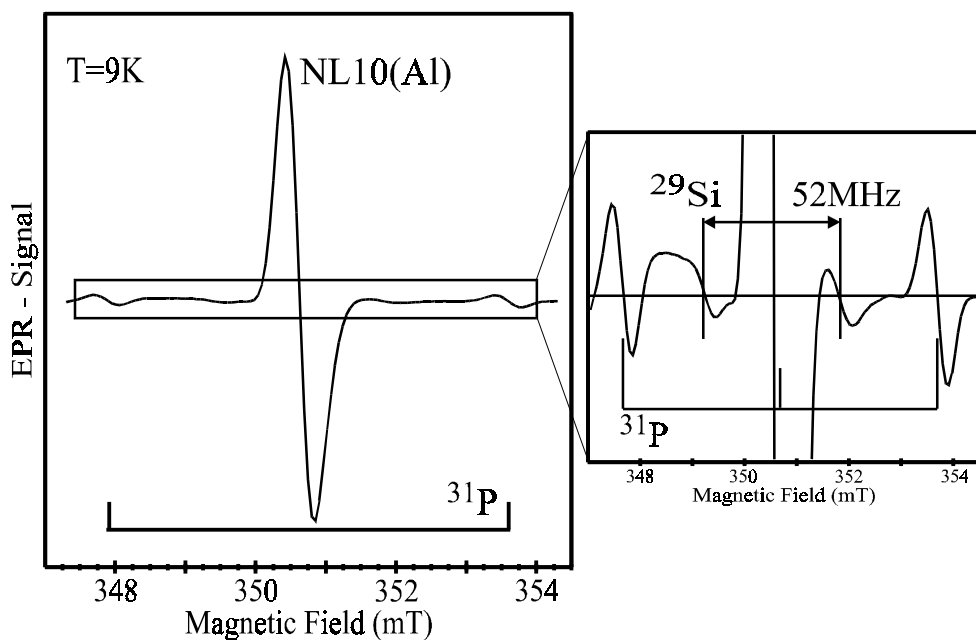


Fig. 5.13 X-band EPR spectrum of a Al-doped Cz-Si sample after annealing at 460°C for 100h. In spite of a nominally phosphorous free Si starting material traces of ^{31}P are observed.

a hyperfine interaction with one ^{29}Si nuclei again. However, the splitting constant a for the D2 and NL10(H) centres is larger than that obtained for D1.

Finally, an Al-doped (p-type) Cz-Si sample, annealed for 100h at 460°C was examined. The sample was originally prepared by Meilwes and the incorporation of aluminium in the NL10 centre proven with ENDOR [Meilwes 1993]. The NL10(Al) defect had been studied in detail and resonance lines due to ^{31}P in the nominally phosphorous free silicon had been observed by Meilwes. However, in the present study the NL10(Al) satellite lines were detected for the first time upon increased signal integration. The NL10(Al) EPR spectrum is shown in figure 5.13. For the hyperfine splitting a value of (52 ± 1)MHz is determined, which is significantly smaller compared to those found for the centres studied so far. Further, the intensity ratio of the satellite lines (1.7%) is too small to be explained by a ^{29}Si hyperfine interaction of the NL10(Al) centre. The findings are discussed in a later section.

It can be concluded from the investigation of the shallow donor hyperfine lines that a prominent interaction of the unpaired electron of the defect with one neighbouring or interstitial Si-atom is observed.

5.6 ENDOR investigation of the shallow donors D1 and D2

The precedent EPR measurements have already revealed strong similarities between the D1/D2 donors appearing after hydrogenation, electron irradiation and annealing and the NL10(H) donors reported in literature. In order to reveal the atomic structure of the D_n-species and to find additional arguments for their identification with the hydrogen incorporating donors NL10(H), ENDOR measurements have been carried out. Figure 5.14 shows ENDOR spectra in the frequency range of (14.8–15.2)MHz for an electron-irradiated Si:O,H sample which was annealed at 350°C and had a strong EPR signal due to the D1 centre.

Prominent resonance lines are observed in the spectra. The lines are positioned symmetrically around the nuclear frequency of free hydrogen and depict the hyperfine interaction.

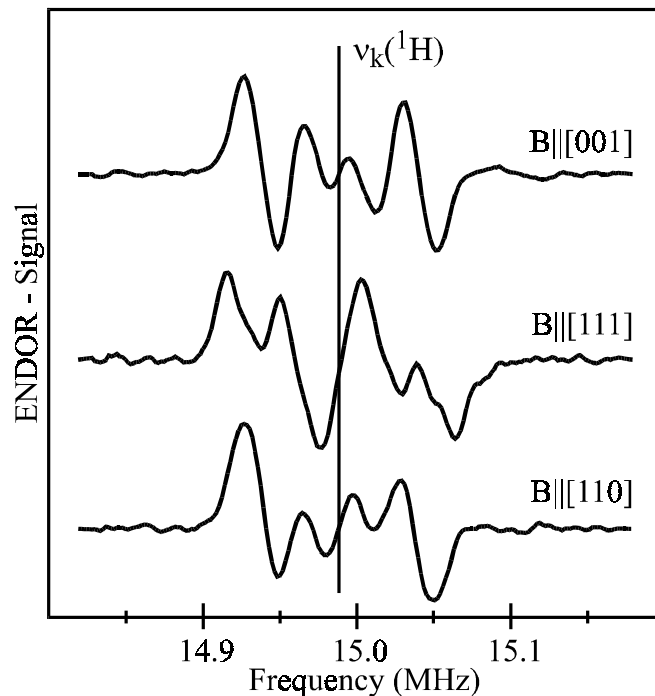


Fig. 5.14 ENDOR spectra of an electron-irradiated Si:O,H sample annealed at 350°C, measured at 7K with illumination of the sample with white light. A microwave frequency of 9.8GHz and frequency-modulation of the rf-field was used. Indicated is the position of the frequency of the free hydrogen nucleus calculated for a static magnetic field of $B=352\text{mT}$. Three spectra for the main crystallographic orientations are given.

tion between the unpaired electron and a hydrogen nucleus. Thus, hydrogen incorporation into the D1 donor is proven. Apparent changes in the spectra upon rotation of the sample with respect to the static magnetic field ("characteristic" as opposed to "distant" ENDOR) are observed showing that the hydrogen atom takes a characteristic position within the structure of the centre.

A deconvolution of the ENDOR spectra was performed assuming various symmetries of the defect. Due to the nuclear spin $I=1/2$ of the hydrogen two sets of resonance lines have to be used, placed symmetrically around the frequency of a free hydrogen nucleus. Thus spectra consisting of 2·12, 2·7 and 2·4 ENDOR lines for triclinic, monoclinic-I and orthorhombic-I symmetry, respectively, were simulated. The simulation was performed

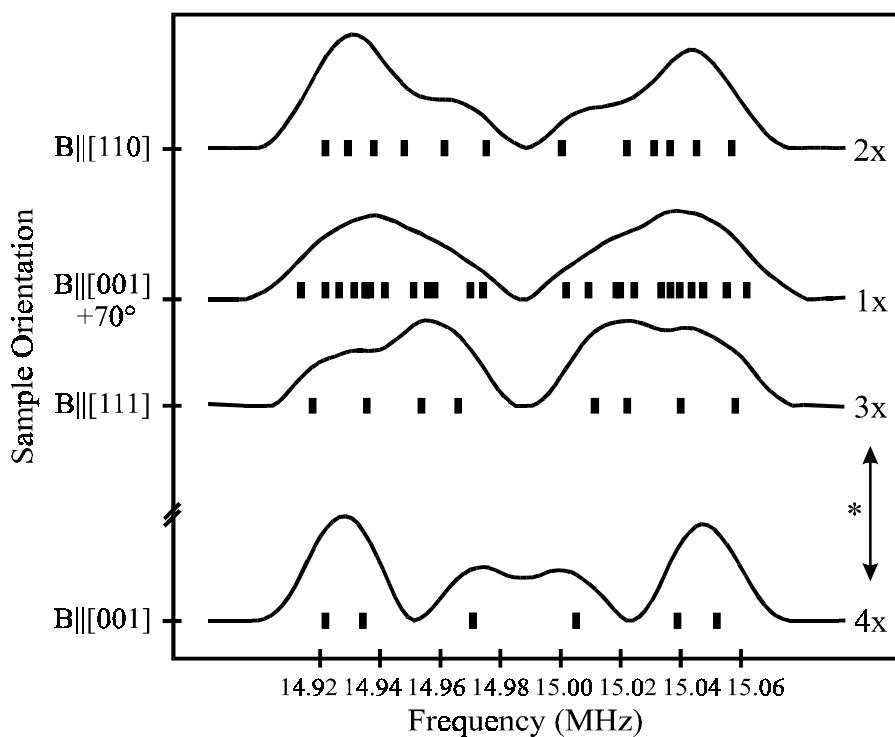


Fig. 5.15 Comparison of the ENDOR line positions as determined by fit and simulation, assuming a triclinic symmetry, with the corresponding, integrated ENDOR spectra. With (*) the number of ENDOR lines coinciding at each data point of an orientation is given. Data points and spectra are shown for the main crystallographic orientations and one additional orientation ($\vec{B} \parallel [001] + 70^\circ$). The latter angle is chosen to depict the largest width of the spectrum.

for all (10) ENDOR spectra recorded upon rotation in the range of (0–90)° with 10° steps. The obtained correlation coefficient for the deconvoluted spectra was 98%, 91% and 82% for triclinic, monoclinic-I and orthorhombic-I symmetry, respectively. Thus, triclinic symmetry was chosen.

To confirm the choice of the triclinic symmetry the ENDOR spectra with differential line shapes were integrated and compared to the ENDOR line positions determined by fit and simulation. In figure 5.15 four examples of such a comparison are shown. The three angles $\vec{B} \parallel [001], [111], [1\bar{1}0]$ have been chosen as for these orientations several of the total 2·12 lines coincide. The pattern of the positions where the lines coincide is characteristic for a triclinic symmetry of the defect centre. Further, the results for the angle $\vec{B} \parallel [001] + 70^\circ$ are shown, as for this orientation the largest width of the spectrum is detected. It is noted that the numbers (*) indicate the quantity of ENDOR lines coinciding for each data point for a certain sample orientation. Thus, the numbers represent the signal strength of each data point. Especially for the orientation $\vec{B} \parallel [001]$ the composition of the ENDOR spectrum is obvious. The signal intensity of the integrated spectrum can be described by 2:1:1:2 (left to right). The double intensity is caused by the two adjacent resonance lines whereas only one is responsible for the single intensity detected at the inner side of each ENDOR branch.

A further detail is noted for a later discussion of the anisotropic hf parameters b and b' . From the spectrum $\vec{B} \parallel [110]$ the smallest gap between the two ENDOR branches can be determined (18kHz) whereas for $\vec{B} \parallel [001] + 70^\circ$ a largest width of the overall spectrum (148kHz) can be found.

In summary, the triclinic symmetry of the defect can be assumed to be the correct one. Resulting from the triclinic symmetry it can be stated that only one hydrogen atom is incorporated in the defect. Further consequences of these results are discussed in a later section.

In figure 5.16 the solid lines represent the results of a computer calculation of the ENDOR angular dependence using triclinic symmetry with the following parameters of the hyperfine interactions $a = \mp 88\text{kHz}$, $b = \pm 40\text{kHz}$ and $b' = \pm 20\text{kHz}$, given with an accuracy of $\pm 5\%$. The z-axis of the tensor is pointing along $[110] \pm 3^\circ$ direction. The orientation of the hf tensor is shown in figure 5.17 in a more detailed way and the orientation of the z-axis in the atomic structure of the defect is explained in figure 5.20. In figure 5.16 the positions of ENDOR lines for four sample orientations relative to the magnetic field, determined by fit and simulation of the respective spectra, are given as well

The hf interactions are given in terms of the isotropic hyperfine (hf) constant a and the anisotropic hf constants b and b' which are related to the principal values of the usual hf tensor $A_{x'x'}$, $A_{y'y'}$, $A_{z'z'}$ by:

$$a = (A_{x'x'} + A_{y'y'} + A_{z'z'}) / 3$$

$$b = (A_{z'z'} - a) / 2$$

$$b' = (A_{x'x'} - A_{y'y'}) / 2$$

The absolute signs of the hf constants cannot be determined experimentally. However, the isotropic and anisotropic hf constants show opposite signs. The choice of a negative

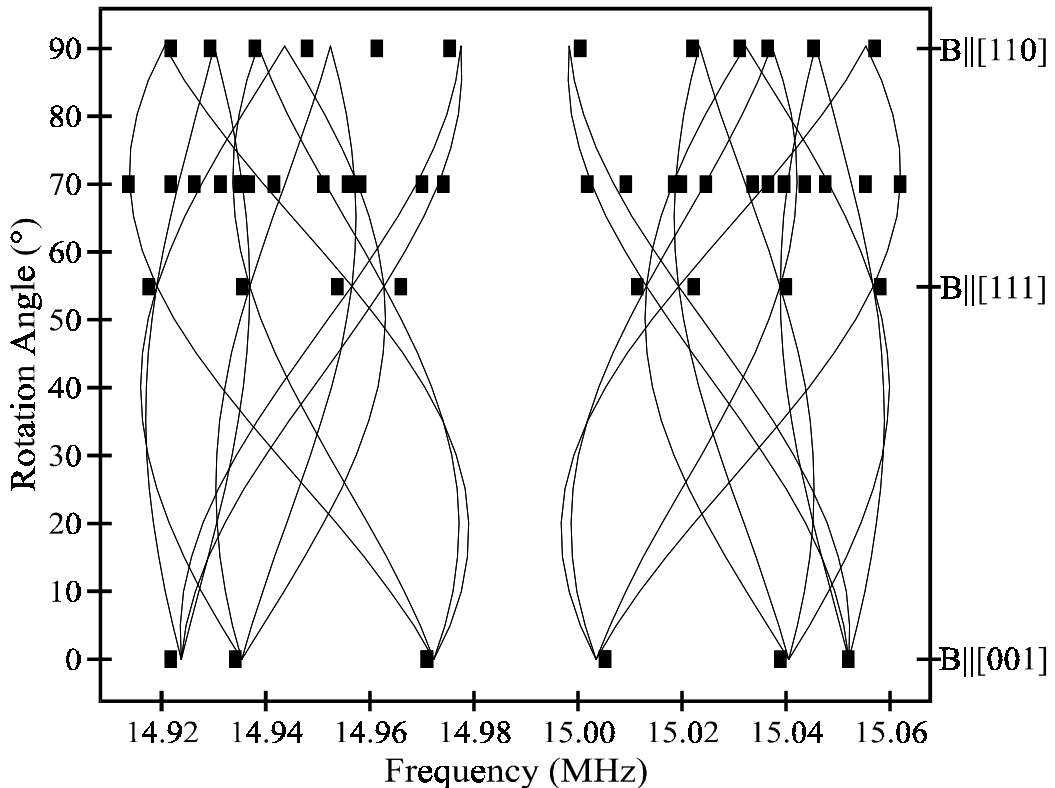


Fig. 5.16 Calculation of the angular dependence of the D1-hydrogen-ENDOR presented in figure 5.14. A triclinic symmetry with the hyperfine-constants $a=\mp 88\text{kHz}$, $b=\pm 40\text{kHz}$ and $b'=\pm 20\text{kHz}$ was assumed ($\pm 5\%$). Experimental data points for the main crystallographic orientations and one additional orientation ($\vec{B} \parallel [001] + 70^\circ$) are inserted. The latter angle is chosen to depict the largest width of the spectrum.

value for the isotropic part a can be explained by a spin polarisation process which is described by [Carrington 1967]. The anisotropic parts of the tensor, b and b' , can be explained by a point dipole-dipole interaction. The parameters a , b and b' are discussed later in more detail.

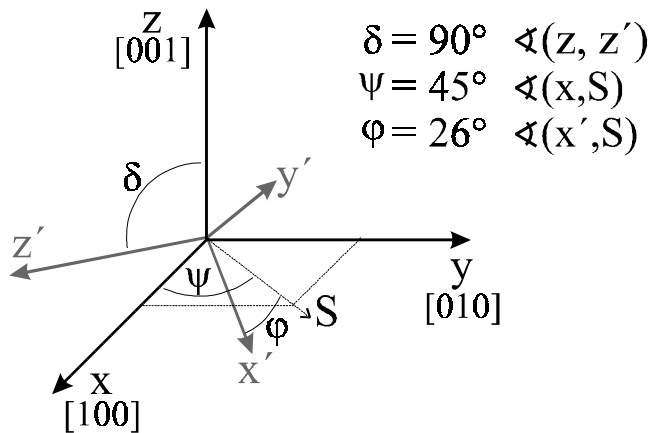


Fig. 5.17 Orientation of the hf tensor (x' , y' , z') according to the transformations necessary to successfully calculate the ENDOR angular dependence assuming triclinic symmetry. “S” indicates the intersection line between the (x , y)- and the (x' , y')-plane.

To obtain information about the field-gradient at the site of the hydrogen nucleus this atom has to be exchanged by one with a nuclear spin of $I=1$, i.e. having a quadrupole moment. For this reason samples were prepared with deuterium ($I=1$) instead of hydrogen during the gas heat treatment cycle. An irradiated sample, finally heat treated at 350°C to create the D1 centre, has revealed EPR features identical to those investigated before with the hydrogen incorporation. No ENDOR lines in the frequency range (14.8–15.2)MHz have been observed in this sample. However, new lines in the frequency range of (2.1–2.4)MHz occur. An ENDOR spectrum of the deuterium-doped sample with D1 centers is given in figure 5.18(a). Three prominent resonance lines placed symmetrically around the nuclear frequency of free deuterium are observed. The spectrum was analysed with respect to further ENDOR lines which should appear symmetrically around these, but all other signals can only be explained by the high noise level of the spectrum.

For the parameters of the hf tensor of the deuterium-ENDOR it has to be considered that the exchange of hydrogen by deuterium does not change the symmetry of the defect. However, to simulate the recorded spectrum the ratio of $g_{n(H)}/g_{n(D)} = 0.1535$ of the nuclear g -factors of hydrogen ($g_n=5.585$) and deuterium ($g_n=0.857$) has to be considered. Hence, the hf constants found for the corresponding hydrogen ENDOR spectra have to be downscaled by this factor, leading to $a=\mp 13\text{kHz}$, $b=\pm 6\text{kHz}$ and $b'=\pm 3\text{kHz}$ with an accuracy of $\pm 5\%$. In figure 5.18(b) a stick spectrum calculated with the downscaled hf

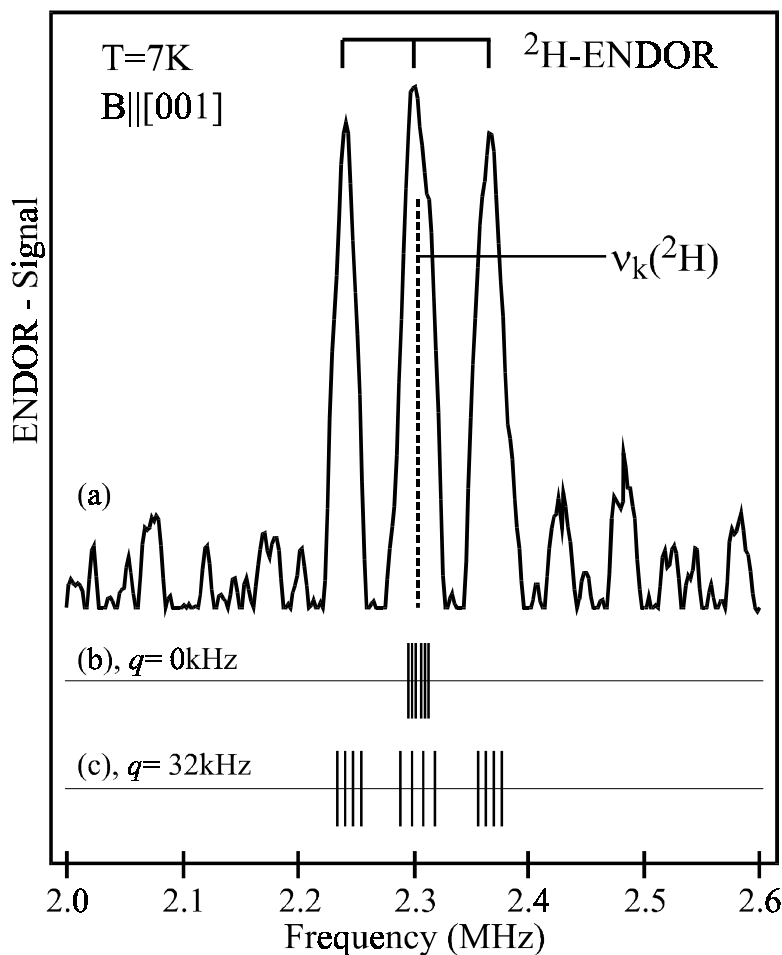


Fig. 5.18 In (a) the ENDOR spectrum of an electron-irradiated, deuterium-enriched Si:O sample, annealed at 350°C (D1(D) centre). The sample was measured with illumination with white light. A microwave frequency of 9.8GHz and frequency-modulation of the rf-field was used. The frequency of the free deuterium nucleus, calculated for a static magnetic field of $B=352.2\text{mT}$, is indicated. The stick spectra in (b) and (c) are explained in the text.

parameters is given. It is obvious that the recorded spectrum cannot be explained sufficiently by this calculation. A quadrupole interaction of deuterium has to be taken into account with $Q_{[001]}=64\text{kHz}$ additionally. This leads to a satisfactorily description of the D1-deuterium ENDOR spectrum as can be seen by the stick spectrum in figure 5.18(c). The tensor of the hf interaction was assumed to be the same as used to calculate the D1-ENDOR angular dependence. However, to explain the D1-deuterium ENDOR spectrum for $\vec{B} \parallel [001]$ with a quadrupole interaction the z-axis of the quadrupole tensor and thus the field gradient was assumed to be aligned along [001]. A relative strong deuterium ENDOR signal as depicted in figure 5.18 was only detected for $\vec{B} \parallel [001]$. Attempts to detect deuterium signals for further orientations of the sample failed, thus the orientations of the tensors cannot be verified and remain speculative.

To obtain information about the incorporation of hydrogen into another species of the D_n family, ENDOR measurements were performed using a specimen annealed at 450°C thus leading to the creation of D2 centers. The respective spectrum is given in figure 5.19. The ENDOR lines are again placed symmetrically around the hydrogen frequency but a reduced width of the pattern compared to that shown in figure 5.14 occurs. This indicates a smaller hf interaction of the unpaired electron with one hydrogen atom in this case. There are apparent changes in the spectra upon rotation of the samples in $(1\bar{1}0)$ plane with respect to the magnetic field direction, but strong overlapping of the individual resonance lines makes the determination of positions of the lines extremely difficult. Nevertheless, a calculation of the ENDOR angular dependence with triclinic

	a (kHz)	b (kHz)	b' (kHz)	$Q_{[001]}$ (kHz)
D1 (hydrogen)	∓ 88	± 40	± 20	—
D1 (deuterium)	∓ 13	± 6	± 3	± 64
D2 (hydrogen)	∓ 75	± 25	± 5	—

Table 5.5 Calculated values for the hf interaction constants. The error of the hf values is within $\pm 5\%$ for D1-hydrogen and D1-deuterium. For D2 the error is estimated to be within $\pm 15\%$. The value for the quadrupole interaction q is calculated with a certainty of $\pm 20\%$. For all three defects the same tensor orientation was assumed.

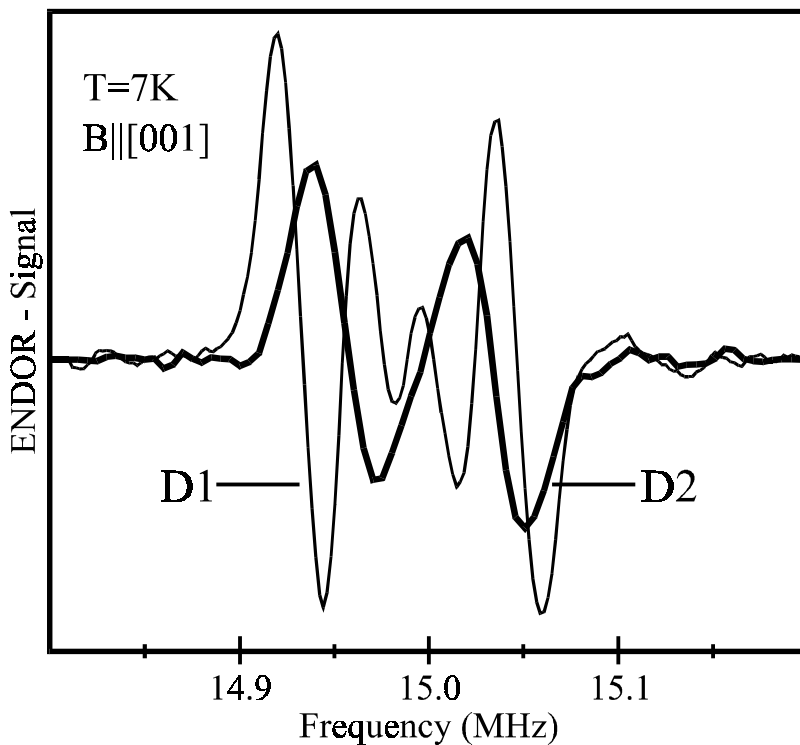


Fig. 5.19 ENDOR spectra of two electron-irradiated, Si:O,H samples, annealed at 350°C (D1) and 450°C (D2), respectively. The samples illuminated ith white light during measurement. A microwave frequency of 9.8GHz and frequency-modulation of the rf-field was used.

symmetry of the D2 tensor reveals the hf parameters as given in table 5.5. Since the resolution of the D2 spectra was very low the only appropriate way was to assume the lowest symmetry possible, being triclinic. Therefore, the same tensor orientation as for the D1-hydrogen and the D1-deuterium sample was used.

5.7 Discussion

Two models of the atomic structure of the STD(H) centers have been proposed so far. On the basis of similarities in arrangements of oxygen and silicon atoms for the STD(H) and oxygen-related thermal double donors (TDD) and a sequential formation of these defects, an identification of the STD(H) / NL10(H) centre as a singly passivated state of the TDDs in its neutral charge state was suggested [Martynov 1995]. According to another model, carbon atoms play an important role in the appearance of the STD(H)

centers and a $(C-H)_i-O_{2i}$ structure was proposed as a core of the STD(H) family [Ewels 1996].

The former model is not consistent with several experimental observations. Particularly, STD(H) centers are found to be stable up to 500°C [Newman 1998], while, according to deep level transient spectroscopy measurements, passivated TDDs dissociate at about 200°C [Weber 1996]. It appears that the results of the presented infrared absorption measurements are not consistent with this model either. The concentration of TDDs is found to be negligible ($\leq 10^{13} \text{ cm}^{-3}$) in hydrogenated irradiated Cz-Si samples after short-time ($t=30\text{min}$) anneals at (350–450)°C, while the concentration of D1 and D2 centers exceeds 10^{15} cm^{-3} in the samples. It seems to be extremely unlikely that TDDs in concentration exceeding 10^{15} cm^{-3} can be formed so fast and then be passivated by hydrogen during short-time treatments of irradiated Si:O,H samples at (350–450)°C. To achieve a TDD concentration of 10^{15} cm^{-3} at these temperatures anneals for at least $t \geq 60\text{min}$ are necessary.

A closer look at the results of the NL10 H-ENDOR presented by Martynov et al. [Martynov 1995] shall be taken. The authors investigated Cz-Si samples that had been treated with hydrogen prior to annealing at 470°C for various periods. Equal to the D1 and D2 investigations of this work they performed angular dependent ENDOR measurements for a rotation of the sample in a $(1\bar{1}0)$ -plane. The data are given with the principal hf values combined with the respective orientation cosines. For comparability they have been transformed to the a , b and b' format, used in this work and are given in table 5.6. Martynov et al. fitted the NL10(H) ENDOR angular dependence using two similar hf tensors of triclinic symmetry. Thus, the spectra are described by 48 resonance lines altogether, giving a high degree of freedom for the fitting of the spectra and hence reducing the reliability of the fit. The tensor orientation given by Martynov does not allow any alignment of one of the tensor axes with an orientation of the silicon lattice and no atomic model of the NL10(H) is given. Both can most probably be explained by the low signal-to-noise ratio of the spectra recorded by Martynov. Only one spectrum of the NL10(H) ENDOR has been published by the author. A comparison of this with the spectra recorded in this study reveals a higher signal-to-noise ratio of the latter. Generally speaking, the results obtained in this work can be regarded with a higher degree of certainty.

It is apparent from table 5.6 that Martynov did not observe a change of the sign for the isotropic and anisotropic hf parameters. However, it will be shown later that this change is partly characteristic for the atomic model of the NL10(H).

Although the isotropic parts a of the hf tensor are very similar for all three ENDOR studies compared in table 5.6, significant differences are obvious regarding the anisotropic parts b and b' . The question arises which of the two centres D1 or D2 the Martynov NL10(H) can be compared to. The comparison of the values for b and b' indicates an identification of the D2 with the NL10(H), and further arguments can be found. To conventionally create the NL10(H) defect in a concentration sufficient for ENDOR Martynov had to anneal the samples for 20h at least. For annealing periods as long as this it is known that multiple species of the NL10(H) are created. Their resonances are super-positioned in the spectra, but it is known that they show a decreasing anisotropy (see chapter 4). The latter fact explains the low values for the anisotropic hf parameters b and b' , whereas the value for the isotropic part a remains similar for all presented samples.

It has been shown by FTIR and EPR at the beginning of this chapter that the preparation

	a (kHz)	b (kHz)	b' (kHz)	δ ($^{\circ}$)	ψ ($^{\circ}$)	φ ($^{\circ}$)	Refs.
D1 (H)	∓ 88	± 40	± 20	90	45	26	this work
D2 (H)	∓ 75	± 25	± 5	90	45	26	this work
NL10 (H)	84.6	15.2	14.8	75	30	55	Martynov (1995)
	80.6	15.0	11.4	70	35	50	

Table 5.6 The values for the D1 ($\pm 5\%$) and D2 ($\pm 15\%$) hf interaction constants yielded in this work and those presented by [Martynov 1995] are compared. A triclinic symmetry of the defect was assumed in each case. Martynov et al. presented their data with the principal hf values associated to the direction cosines. Thus, the values had to be transformed to the a , b , b' format used in this work. The data were arranged in such a way that the z-axis of the hf tensor is oriented along the direction of the largest hf interaction. No value of the error of the hf constants is given by Martynov.

method of hydrogenation, electron-irradiation and annealing used in this study provides the facility to prepare the first species of NL10(H) selectively. Hence, from a comparison of the hf parameters and the preparation methods of the samples it can be concluded that an identification of the Martynov NL10(H) with the D2 of this work is most likely. As a consequence, it can be stated that with the D1 defect the first species of the NL10(H) has been studied with ENDOR in this study for the first time.

In this study several arguments have been found to support the $(C-H)_i-O_{2i}$ structure, originally suggested by Ewels et al. [Ewels 1996]. An atomic model of the NL10(H) defect is shown in the figures 5.20 and 5.21. The C_i atom is placed slightly above the $(1\bar{1}0)$ -plane in which next to the Si lattice atoms the two O_i are located. The H_i is bonded to the C_i in a $[1\bar{1}0]$ direction. The Si atom bonded to the C_i in the $[00\bar{1}]$ direction is attached to two further Si atoms on regular lattice sites, but lacks bonding of its fourth electron. The silicon p_z orbital with the unpaired electron is aligned along the

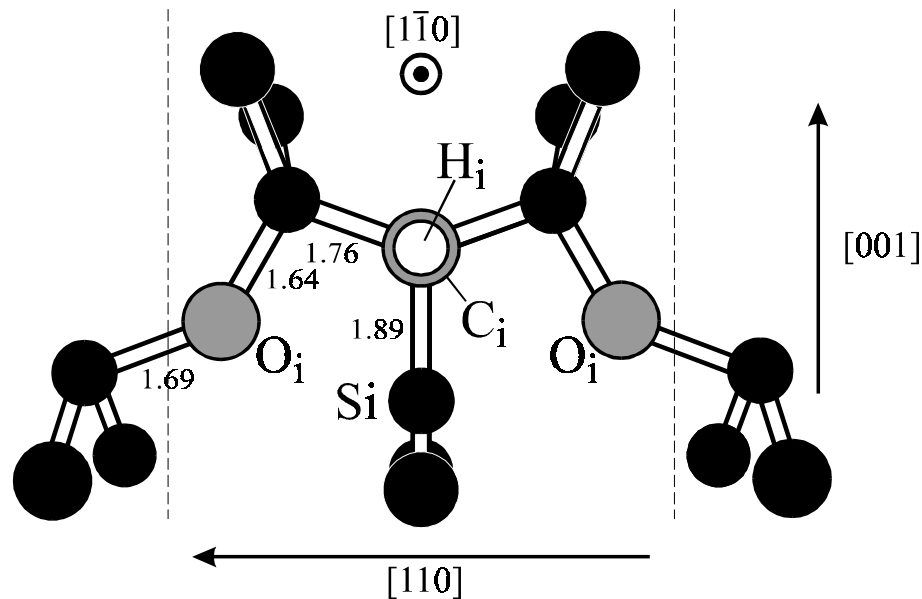


Fig. 5.20 Atomic model of the core structure of STD(H) on the basis of the calculations by Ewels et al. [Ewels 1996]. The position of the hydrogen is determined from ENDOR investigations in this study. The numbers in the figure indicate the bond lengths in Å. In figure 5.21 the central part of the model (bordered by the dashed lines) is shown in a different orientation.

[110] direction. From the calculated Kohn-Sham eigenvalues Ewels et al. estimated a high spin density in the silicon p_z -orbital and concluded a single shallow donor level of the defect [Ewels 1996]. It is noted that Ewels obtained his results from calculations of clusters with 151 atoms. Since the cluster size is small the calculated spin densities are significantly higher compared those predicted by effective-mass-theory (EMT). Further, no absolute values for the spin densities were given by the authors.

In the following paragraphs results of this work and considerations are presented which support the $(C-H)_i-O_{2i}$ model of the core structure of the shallow thermal donors.

The enhanced formation of STD(H) n centres in irradiated samples can be considered as an indirect evidence for the carbon-related model of the STD(H). According to this model, the formation of the STD(H) donor core requires the appearance of interstitial carbon atoms (C_i) in Cz-Si crystals. The main mechanism of their appearance is known to be the interaction of silicon self-interstitials (I_{Si}) with substitutional carbon atoms (C_S) [Watkins 1965]. The concentration of the C_S is typically at least $5 \cdot 10^{15} \text{ cm}^{-3}$ in Cz-silicon crystals [Series 1982].

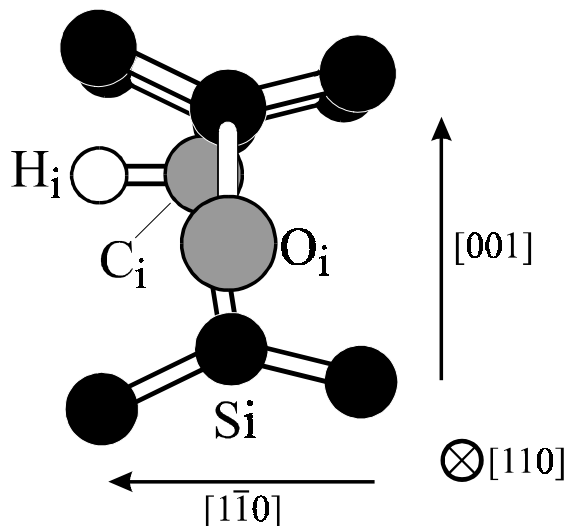


Fig. 5.21 Atomic model of the core structure of STD(H) on the basis of the calculations by Ewels et al. [Ewels 1996] and the results of this work. In comparison to figure 5.20 the atomic model has been rotated for 90° about the [001] direction and only the central part of figure 5.20 (bordered by the dashed lines there) is shown.

The creation of silicon self-interstitials and consequently C_i in non-irradiated Cz-Si samples upon annealing at about 450°C is believed to be associated with the process of oxygen aggregation [Newman 1990]. As the C_i are effectively formed due to the interaction of radiation-induced I_{Si} with C_S , the enhanced formation of shallow donor centers in irradiated Cz-Si:H samples can be easily explained assuming that the STD(H) species incorporate a C_i -H unit.

The calculated value for the hf constant of the free hydrogen atom is 1420.4MHz. Estimating the ratio of this value to the one observed in the ENDOR experiments ($a = \mp 88\text{kHz}$) leads to an extremely small unpaired spin density in an hydrogen 1s orbital ($\sim 6 \cdot 10^{-5}$). The hydrogen atom is therefore in a diamagnetic charge state. Because of a well defined hf tensor orientation it is bonded to a lattice or interstitial atom. However, the small unpaired spin density of the hydrogen cannot come from this bond. It is well possible that the hydrogen is placed next to a C_i , forming $(C-H)_i$. A theoretical interpretation of the hydrogen hf interaction with its characteristic opposite signs of the isotropic and anisotropic part can be given for this model.

The negative sign of the isotropic part of the hf tensor can be explained by a spin-polarisation process between the $2p_z$ -orbitals of the interstitial carbon atom and the $1s$ -orbitals of the bonded hydrogen [e.g. Carrington 1967]. It is known from aromatic radicals that the odd electron occupies a molecular π orbital delocalised over the carbon atom framework of the molecule. This orbital, formed by an overlap of the carbon $2p_z$ atomic orbitals, has a node in the plane of the molecule, where the ring hydrogen atoms are. However, the unpaired spin density of the $1s$ orbitals necessary for the observed hyperfine splittings can not be explained by this configuration yet. It has to be considered that the exchange forces between the electrons couple together the spins of the σ electrons in the C–H bond and the π electrons in the ring. With molecular orbital theory the coupling can be explained by assuming an isolated $>C-H$ fragment with one π electron, occupying the carbon $2p_z$ orbital, perpendicular to the plane of the three trigonal bonds. Considering the two electrons forming the σ C–H bond, the fragment can be drawn as shown in figure 5.22.

In approximation of a perfect pairing one would consider the structures a) and b) to be equally important. Taking into account the interaction between the σ and π systems, structure a) is slightly preferred because of the favourable exchange interaction between the π electron and the carbon σ electron, whose spins are parallel. The spins in the C–H

σ bond are therefore polarised slightly. If the odd electron has spin α , there is slight excess α spin in the carbon σ orbital and corresponding excess β spin in the hydrogen 1s orbital. This gives rise to a negative isotropic proton splitting. It is noted that α spin in the carbon p_{π} orbital induces β spin at the proton. For this reason the spin density at the proton and the hyperfine coupling constant are both negative.

A value of $a_H = -23.04\text{G}$ for the β proton splitting for an unpaired spin density of 100% in the carbon p_z orbital is known for methyl radicals ($-\text{CH}_3$) [e.g. Carrington 1967]. For a reduced spin density the splitting constant is consequently lowered. The hf splitting constant derived from the hydrogen ENDOR measurements of the shallow donor centre D1 in this work can be written as $a_{H,\text{exp.}} = -0.00315\text{G}$ ($a = \mp 88\text{kHz}$, table 5.5). The resulting ratio of $a_H/a_{H,\text{exp.}} = 0.0014$ or 0.14% indicates a very low spin density in the carbon p_z orbital. This corresponds nicely with the findings of Ewels et al. whose calculations revealed a negligible spin density on both the carbon and hydrogen atom for the favoured $(\text{C-H})_i\text{-O}_{2i}$ structure for STD(H) [Jones 2000].

It is noted that the spin polarisation process described above is not exactly accurate for the atomic model of the shallow donors as presented in figure 5.20/5.21. The process explained by Carrington is based on a hydrogen atom being regularly bonded to a carbon atom [Carrington 1967]. In the present case of the $(\text{C-H})_i\text{-O}_{2i}$ structure the H_i is bonded to a C_i and no further electrons of this are unpaired. More exact, the unpaired electron of the $(\text{C-H})_i\text{-O}_{2i}$ structure is located in the p_z orbital of the Si atom which is bonded along a $[00\bar{1}]$ direction to the C_i . Thus the spin polarisation process takes part between the unpaired electron of the Si atom and the hydrogen atom via the carbon

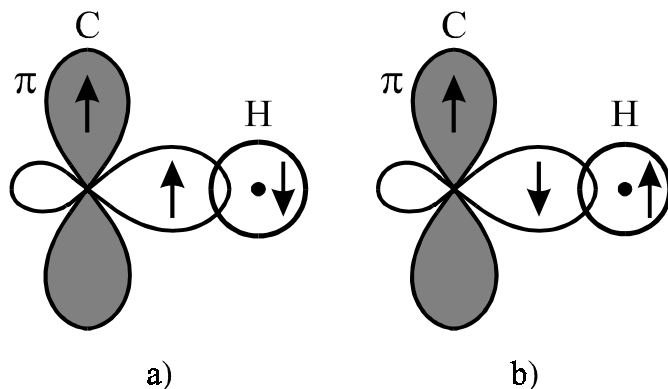


Fig. 5.22 Atomic orbital models of the two electron configurations of the σ bond for a C–H fragment.

atom. The process is known as “superexchange”.

In EPR an isotropic interaction of ^{29}Si nuclei with the D_n centres of $a=(60\text{--}70)\text{MHz}$ was observed. With an isotropic hf splitting constant of 4594MHz [Morton 1977]for a 3s silicon orbital with 100% spin density, a ratio of both the observed and the maximal interaction of $1.3 \cdot 10^{-2}$ is calculated. The value represents the spin density at the silicon. It can be assumed that a spin density of about one order of magnitude less is induced at the site of the carbon. This results in a spin density of $1.3 \cdot 10^{-3}$ in the carbon orbitals, a value which is in excellent agreement with the one obtained from the ENDOR analysis above (0.14% or $1.4 \cdot 10^{-3}$).

For the silicon atom equal spin densities can be assumed as well in the 3s- as in the 3p-orbital. The spin density value of $1.3 \cdot 10^{-2}$ obtained above leads to an anisotropic hf interaction which would detectable as an angular dependence of the observed interaction with the ^{29}Si nuclei. With an anisotropic interaction value of about 114MHz [Morton 1977] for the silicon 3p orbital the angular variation of the ^{29}Si satellite positions would be of about 1MHz. However, this variation is below the resolution of the experiments performed in this study.

With the result of 0.14% spin density in the carbon p_z orbital a valuable information is given to consider the point dipole-dipole interaction, leading to the anisotropic hf interaction constant b . This can be calculated as $b_H = 95.625 g_n / R_B^3$ where R_B is the distance between the neighbour nucleus and the defect centre (in atomic units) [Spaeth 1992]. Assuming a C–H bond length of $R=1.2\text{\AA}$ and a g -factor of the hydrogen nucleus of $g_n=5.58569$ a hf constant of $b_H=61.46\text{MHz}$ is obtained. Scaling this value by the factor obtained for the carbon p_z -orbital 0.14% results in $b_H=46\text{kHz}$, being in excellent agreement with the experimentally obtained data of $b_{H,\text{exp}}=40\text{kHz}$.

An explanation of the smaller hf interactions for the D2 centre compared with those for the D1 can be found considering the decreased ionisation-energy of D2 to D1 centers and thus the lower localisation of the paramagnetic electron on the hydrogen atom.

As a summary of the above sections about the hf interaction constants it can be noted that an excellent agreement of the observed hf parameters with those gained by theoretical considerations is found. The “superexchange” process can explain the orientation of the hf tensor with its z-axis parallel $[1\bar{1}0]$ as well.

The EPR investigation of the hyperfine interactions of the D_n centres with ^{29}Si nuclei reveals that one silicon atom is taking a prominent position in the defect structure. This result corresponds nicely to the results obtained from calculations by Ewels et al., who find a very low spin density on the interstitial atoms (N_i for STD(X) and C_i for STD(H)) but a significant one on the nearest Si-atom. In this work this hf interaction has been observed for NL10(H) prepared only by hydrogenation and annealing for the first time. The observation of the satellite lines in both the D_n and NL10 centres provides a further argument to identify the D_n and the NL10(H) centers.

Martynov et al. observed weak hydrogen-related ENDOR lines in nominally H-free samples which had been doped with Al [Martynov 1995]. The finding was astonishing as no indications had been presented earlier about an incorporation of H in the NL(Al) defect structure. No model of the defect has been presented by the authors and the connection of the Al-atoms with the hydrogen remained unclear. With respect to the alleged observation of hf interaction of NL10(Al) centres with ^{29}Si nuclei an explanation consistent with all experimental findings and suggested defect models can be found. The decisive argument is the low ratio of the integrated area under the satellite lines compared to the integrated area under all lines of only 1.7%. The result clearly indicates that the central line ascribed to the NL10(Al) is not causing the satellite lines. The central line is most probably a superposition of the EPR lines of NL10(Al) and a weaker resonances arising from NL10(H). The following considerations can explain the formation of NL(H). After prolonged annealing of the Al-doped sample NL10(Al) is formed with high concentrations. The large number of defects gives rise to further interstitial atoms such as carbon which is generally present in the Cz-Si samples. It has been proven that in addition hydrogen is an omnipresent contamination in the samples. Both elements give rise to low concentrations of the NL10(H) of D_n centres after prolonged annealing. Thus, the low intensity of the satellite lines can be qualitatively explained.

According to ENDOR investigations of the NL10(Al) by Meilwes it was suggested that the defect consists of an oxygen chain aligned along a [110] direction and an interstitial Al-atom in the defect core [Meilwes 1993]. The finding of Al_i by Meilwes and the C_i presented in this work as well as by Ewels indicates strongly that the presence of an interstitial atom is essential for the defect structures of NL10(Al, N, H). Particularly, as Ewels et al. calculated models of shallow donors with an incorporation of an interstitial nitrogen atom as well. The “labelling” atoms can be made interstitial by irradiation or prolonged annealing. No evidence is found to support the model of an H-passivated

NL8 centre being responsible for the NL10 resonances. In fact, the “passivation” model would only explain a single feature found for NL10(H).

So far the incorporation of interstitial carbon in the STD(H)/NL10(H) core structure has been suggested without having any evidence for this assumption from the experimental data. To find a prove for the C_i , a sample diffused with a high concentration of ^{13}C ($n(^{13}C) \approx 10^{16} \text{ cm}^{-3}$) was hydrogenated, electron-irradiated and annealed at 350°C in order to create the shallow donor D1. The isotope ^{13}C has a nuclear spin of $I=1/2$ and should be detectable with ENDOR therefore. Although great efforts have been made to detect a ^{13}C -ENDOR signal, none has been found. The low spin density at the site of the carbon may explain why the detection of the ^{13}C failed. Experiments with high resolution FTIR or Photo Thermal Ionisation Spectroscopy (PTIS) are projected since the change of the isotope leads to a change in the position of the absorption line. Unfortunately, the expected isotope shift is about 0.03 cm^{-1} , a value which is close to the maximum resolution (0.01 cm^{-1}) of the best spectrometers available.

To complete this discussion it is noted that the interstitial carbon atom in the $(C-H)_i-O_{2i}$ model for STD(H)/NL10(H) could be exchanged by an interstitial silicon atom. The structure of the defect would remain the same, as both atoms can have four bonds according to the sp_3 -hybridisation. According to a detailed estimation even the spin densities in the Si_i -orbitals would be very similar to those for the C_i . However, interstitial ^{29}Si -atoms would give rise to characteristic ENDOR resonances which should be detected symmetrically around the “distant” silicon ENDOR line. According to the natural abundance (4.67%) of ^{29}Si , the isotope is present in the samples with a ratio of 4.67% compared to ^{28}Si . Although a sufficient signal-to-noise ratio was achieved by increasing the integration time for the ^{29}Si -ENDOR measurements, no signals of the isotope were detected. The failure to observe such ^{29}Si -ENDOR lines contradicts the assumption of an interstitial Si-atom instead of a C_i in the core of the STD(H)/NL10(H).

All the presented experimental results are consistent with the assignment of the D1, D2 and D3 centres to the STD(H) / NL10(H) family. Electronic properties of the D1 donor differ from those of the other STD(H) n species, but there is a clear correlation in annealing behaviours of the D1 and D2 centres [Markevich 1996]. D2 donors seem to grow at the expense of D1 centres. Thus, it appears that the D1 defect represents the first species of the STD(H) donor family and can be called STD(H)1.

5.8 Conclusions

Direct evidence for the incorporation of one hydrogen atom into the D1 and D2 shallow donor centres is obtained by the observation of hydrogen-related hyperfine interaction lines in ENDOR spectra. Well-defined hydrogen-related ENDOR patterns („characteristic“ as opposed to „distant“ ENDOR) are observed showing that a hydrogen atom takes a characteristic position within the structure of the centres. From the hyperfine interactions with ^{29}Si nuclei it is concluded that one silicon atom is incorporated in a prominent position in the shallow donor centres as well. Evidences for the identity of D2 and D3 defects and two species from the hydrogen-related STD family are obtained from the comparison of positions of IR absorption lines due to these centres. It is argued that the formation of hydrogen-related shallow thermal donors is not related to the hydrogen passivation of thermal double donor centres. In fact, intrinsic point defects (most probably silicon self-interstitials) play an important role in the formation of STD(H). With the selective preparation of D1 and the complex investigation of the donor centre by means of EPR and ENDOR the first species of the hydrogen-related STD family has been examined for the first time. A unifying model for the STD or NL10 families, supported by all experimental findings so far, can be presented as well.

Chapter 6

On the mechanism and applicability of EDEPR

In the chapters 3 and 5 magnetic resonance investigations of various defects in silicon have been presented. Some of the results could only be obtained by EDEPR (chapter 3) and other studies were improved by this method (chapter 5). Because of the diversity of the studied samples a survey of the method itself and is presented in this chapter. First, an investigation of the Thermal Double Donors (TDDs) with EDEPR is described. In this case, however, the method claimed for its sensitivity for small defect concentrations, failed to provide resonance lines of the TDDs. Further examples of unsuccessful EDEPR experiments are presented. The question for the reason of failure leads to the need to understand the mechanism of EDEPR. Therefore, the mechanism will be studied on the basis of the successful EDEPR experiments in the later paragraphs of this chapter.

6.1 Investigation of Cz-silicon after heat-treatment at 470°C

As mentioned before the core structure of the thermal donors is undergoing a controversial discussion for more than three decades, equally for both TDD and STD or NL8 and NL10, respectively. After the electrical detection of EPR was intensively studied in the group of Prof. Dr. J.-M. Spaeth by Dr. B. Stich its mechanism and potentialities were explored. One of the most outstanding advantages was found to be the increased sensitivity regarding the defect concentration in comparison to conventional EPR. This feature, in principle, opened new possibilities to investigate the core structure of the ther-

mal donors. This can be explained by the fact that for the investigation of early stages of oxygen precipitation with low donor concentrations the method of EPR was lacking the required sensitivity. Conventional EPR requires a minimum number of spins of $N \approx 10^{11}$ per cm^3 for a linewidth of 1mT [Spaeth 1992]. In comparison to this Stich presented EDEPR spectra with an estimated spin number of $N \approx 10^8$, leading to the statement of a sensitivity increase by 3 orders of magnitude [Stich 1997]. Therefore EDEPR was intended to investigate the early stages of TDD.

The preparation and characterisation of early stages of TDD in oxygen-rich silicon is illustrated first . The results of detailed EDEPR studies and the conclusions drawn from these results are discussed and a re-interpretation of former findings is presented.

6.1.1 Preparation and FTIR-characterisation of Thermal Double Donors

For the preparation of samples with TDDs, p-type Cz-silicon starting material was used with a boron concentration of $n(\text{B})=3 \cdot 10^{15} \text{ cm}^{-3}$ and an oxygen concentration of $n(\text{O})=8.5 \cdot 10^{17} \text{ cm}^{-3}$. To allow a comparability of the results of this study and those obtained by Stich an identical starting material was chosen [Stich 1997]. Following the idea of a donor-acceptor recombination process being responsible for EDEPR, the acceptor behaviour of B in silicon should match the donor characteristic of the TDDs. The size of the samples was (2.5·2.5·8)mm and their surface was polished by wet chemical etching with CP4 ($\text{HNO}_3:\text{CH}_3\text{COOH:HF}$) in order to facilitate reliable optical measurements (FTIR).

The growth of silicon crystals takes place at elevated temperatures. During the subsequent cooling process of the crystal rod the temperature range where TDDs are created is passed and consequently oxygen precipitates are formed even though in small concentrations. An effective procedure to destroy these thermal donors is to anneal the specimen in an evacuated ampoule at 770°C for 30min. Control measurements with FTIR proved the efficiency of this approach in the limits of the detection limit of $n=1 \cdot 10^{12} \text{ cm}^{-3}$ (see also spectrum “0min” in figure. 6.1). The samples were placed in evacuated ampoules again and heat treated at 470°C for times ranging from (10–300)min. The concentration of TDDs was investigated with FTIR for each sample afterwards.

In figure 6.1 FTIR spectra of samples annealed for (0–60)min are given. The dominant absorption line at $\nu=1136\text{cm}^{-1}$ is due to the antisymmetric resonant vibration mode of interstitial ^{16}O [Hrostowski 1960]. This line is used to determine the ^{16}O concentration in the crystals. The ^{16}O concentration was estimated to $n(\text{O})=5\cdot10^{17}\text{cm}^{-3}$ and thus the value given by the manufacturer Wacker-Chemitronic could be verified.

The FTIR spectrum (“0min”) of the reference sample which was only preannealed at

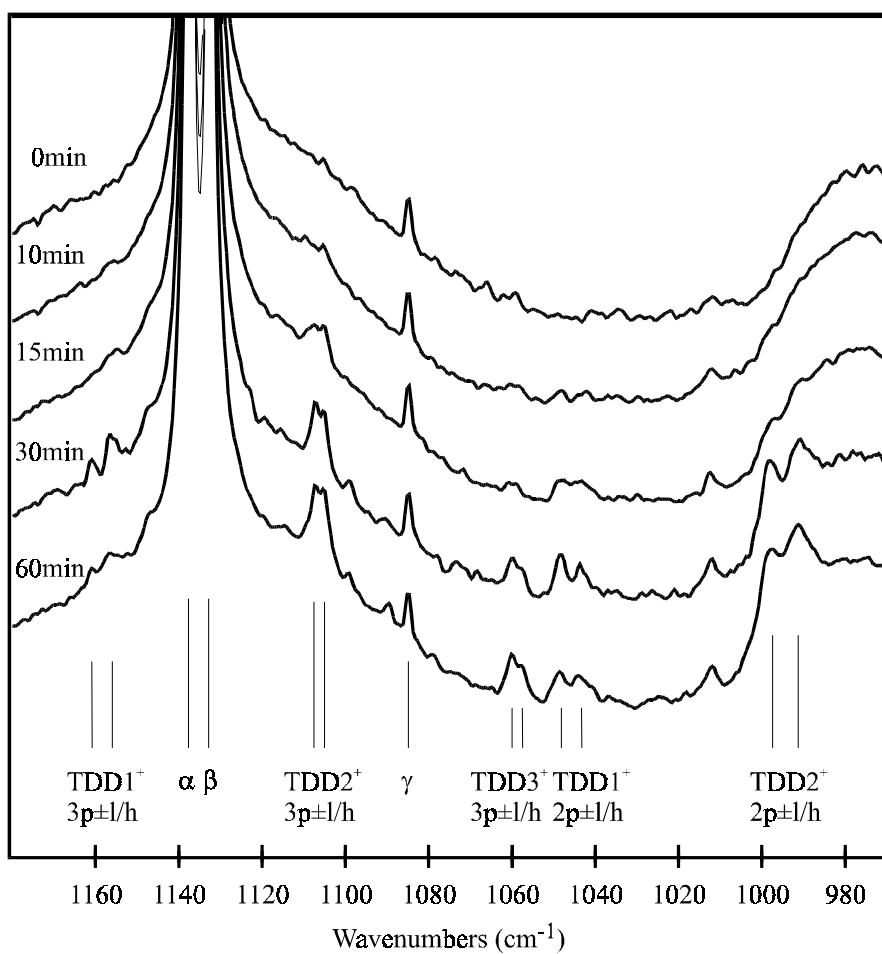


Fig. 6.1 FTIR spectra of Cz-silicon samples after annealing at 470°C in an evacuated ampoule in the range of (0–60)min. All samples had been preannealed at 770°C for 30min in order to destroy thermal donors being possibly present due to the crystal growth process. The Greek letters have the meaning:
 α : antisymmetrical resonant vibrational mode of interstitial ^{16}O ,
 β : first excited state of the rotational mode of $^{28}\text{Si}-^{16}\text{O}-^{28}\text{Si}$,
 γ : antisymmetrical resonant vibrational mode of interstitial ^{18}O .

Annealing time	Concentration of TDD (cm^{-3})		
	TDD1	TDD2	TDD3
0 min	-	-	-
10 min	$1 \cdot 10^{12}$	$2 \cdot 10^{12}$	-
15 min	$1 \cdot 10^{13}$	$6 \cdot 10^{12}$	$1 \cdot 10^{12}$
30 min	$8 \cdot 10^{12}$	$1 \cdot 10^{13}$	$7 \cdot 10^{12}$
60 min	$5 \cdot 10^{12}$	$1 \cdot 10^{13}$	$8 \cdot 10^{12}$

Table 6.1 Concentration of the TDD in Cz-silicon samples after annealing at 470°C for times as given, gained by analysis of the absorption lines due to $1s \rightarrow 3p_0$ ground to excited state electronic transitions.

770°C , reveals no absorption lines of TDDs, demonstrating the effectiveness of the pre-annealing procedure. The development of the absorption lines due to TDD(1–3) in the other spectra is easily followed.

The corresponding concentrations of the TDDs are listed in table 6.1. Note, that the signal intensity of the TDD1 absorption lines decreases after 60min annealing already, whereas those of TDD2 are at their maximum. With the aim to investigate the first two stages of TDD the annealing time has to be chosen in the range of (15–45)min. The achievable concentration of TDD(1–3) would be about $n(\text{TDD}) \approx 10^{13} \text{ cm}^{-3}$ after heat treatment for 30min.

6.1.2 EDEPR of Cz-Si heat treated at 470°C

In order to investigate the early species of the TDDs we re-measured a sample which had been prepared by Stich originally [Stich 1997]. This sample was heat treated for 60min at 470°C and the EDEPR spectrum was found qualitatively identical to the one presented by Stich. The author attributed the detected resonance lines to first species of TDDs.

In figure 6.2 EDEPR spectra of three samples already introduced in conjunction with the FTIR results are shown. Two resonances, which could not be found in EPR, are de-

tected. The line-shapes are similar to the ones found in the TDD-reference sample of Stich.

To achieve a sufficient signal-to-noise ratio for the individual spectra in figure 6.2, the magnetic field range had to be scanned numerous times and 42 spectra were accumulated during about 12h. Thus the resulting spectra are normalised to equal integration times. Very similar signal amplitudes are obtained, even for the sample that had not been annealed at all and for which no absorption lines due to TDDs could be detected in FTIR. Thus, similar spectra and similar signal-to-noise ratios were recorded independ-

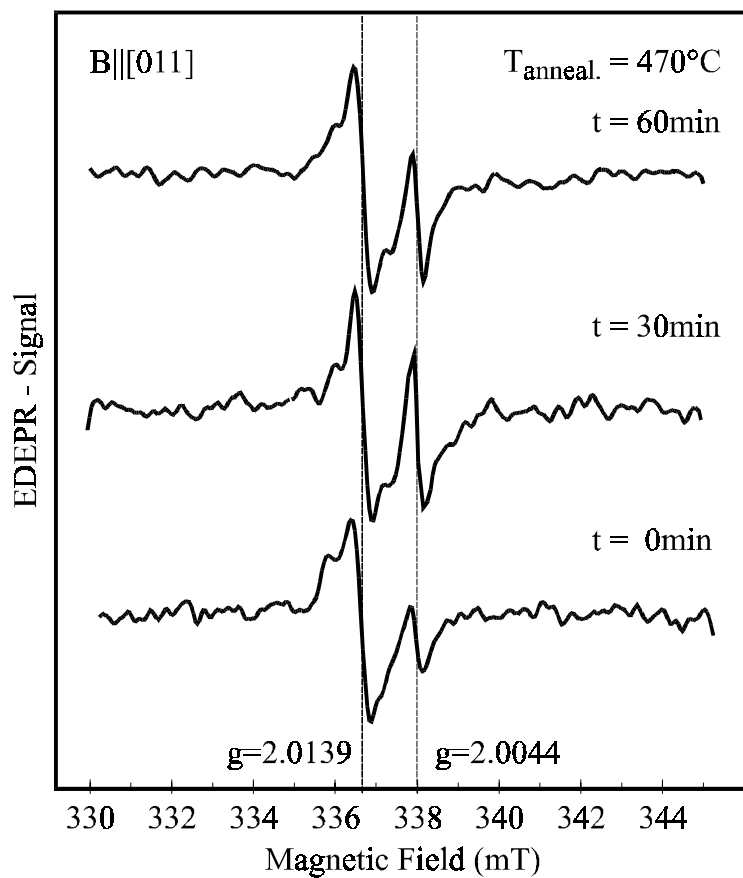


Fig. 6.2 EDEPR spectra of Cz-silicon samples annealed at 470°C for (0-30-60) min after preannealing at 770°C for 30min. Indicated are the g -values of the resonances which can be given with a certainty of $\Delta g = \pm 0.0001$. Measurements were performed at 10K with white light illumination of the samples. A sample current of $5\mu\text{A}$, magnetic field modulation of $5\text{kHz} / 0.2\text{mT}$ and a magnetic field step-width of 0.02mT was used.

ent of the annealing procedure of the samples. Thus, an identification of the resonances with TDDs has to be doubted.

Special care has been taken to study the *g*-value of the detected EDEPR lines. DPPH (2,2-diphenyl-1-pikryl-hydrazyl, $g=2.0036$) was used as a *g*-factor marker and tests of the magnetic field stability over a time period of 10h revealed a shift of the DPPH resonance line of only $\Delta\vec{B}=(0.009\pm0.002\text{mT})$. The *g*-values determined for the two resonance lines in figure 6.2 (2.0139 / 2.0044) can therefore be given with high precision ($\Delta g = \pm 0.0001$). Comparing these *g*-values with those of thermal donors listed in table 4.1 yields no agreement. An identification of the detected lines with TDDs has to be ruled out consequently.

Recalling the results presented in chapter 3 the dangling bond centre P_{bb} occurring at a (100) Si/SiO₂ interface is most likely to be the origin of the detected resonances in the heat-treated samples. This conclusion can be drawn taking into account the sample surfaces being a (100)-plane and the very similar *g*-values obtained for a sample orientation of $\vec{B} \parallel [011]$ in both cases. A characteristic change in line-shape upon rotation of the sample underlines the identification of the detected resonances with the P_{bb} centre. The intensity of the P_{bb} -resonances shown in chapter 3 was very weak, too.

As the resonances detected in the heat-treated samples presented in this chapter were of significantly less intensity compared to those presented in chapter 3 no further investigations were performed. Nevertheless, a very important conclusion can be drawn from the investigations of heat treated silicon presented above. Though two partners, boron and TDDs, are present in the samples, no resonances due to the TDDs nor boron can be detected with EDEPR. It implies that either the concentration of donors and / or acceptors is not suitable for the detection of a recombination process, or that the mechanism for EDEPR is not depending on a donor-acceptor recombination at all for these centres.

6.2 Presentation of further EDEPR experiments

To discuss the EDEPR mechanism further, several experiments performed by Stich are summarised [Stich 1997]. A sample only containing the shallow donor phosphorous were prepared by Stich and investigated with EPR. This sample showed the expected two hyperfine resonance lines of the dopant due to $I=1/2$ of ³¹P. No EDEPR signal could be recorded from this sample and it was concluded that the mechanism of EDEPR would not work with a donor only.

A further sample was prepared in which the shallow donor ^{31}P was compensated by the shallow acceptor boron, both being present in the sample with a concentration of $n(\text{P},\text{B})=1\cdot10^{16}\text{cm}^{-3}$. EPR lines of the ^{31}P could be detected again, but only weak signals of the ^{31}P hyperfine doublet were recorded with EDEPR. The value obtained for the conductivity change was only about $\Delta\sigma/\sigma \approx 9\cdot10^{-6}$. The result was astonishing as according to the donor-acceptor recombination mechanism a stronger EDEPR signal was expected. Surprising was in particular, that both recombination partners were present in the sample with equal, moderate concentrations.

To extend the range of samples a ^{31}P doped one was diffused with chromium (Cr) to a concentration of $n(\text{Cr}) \approx 1\cdot10^{16}\text{cm}^{-3}$. Cr is located as well on interstitial as on substitutional sites in the silicon lattice and shows several donor and acceptor levels. In EPR a spectrum showing Cr_i^+ resonance lines next to ^{31}P lines with a high signal-to-noise ratio was recorded. Again, in EDEPR only weak signals of the resonances could be detected.

Summarising the results by Stich and recalling the failure to detect resonances of the thermal double donors with EDEPR (previous paragraph) it has to be asked why EDEPR performed so badly in these experiments. In particular, as the method is claimed to be highly sensitive with respect to low defect concentrations and to be caused by a donor-acceptor recombination, a property found when studying the dangling bonds centres (P_{ba} and P_{bb}).

A straight-forward approach to answer this question would be to assume too low a concentration of the donor-acceptor pairs in the samples. Therefore, the concentrations of the donors and acceptors are compared. The samples presented in the previous paragraph had a concentration of boron and TDD of $n(\text{B})=3\cdot10^{15}\text{cm}^{-3}$ and $n(\text{TDD}) \approx 10^{13}\text{cm}^{-3}$, respectively. Thus, the averaged distance between two donor-acceptor pairs is determined by the concentration of the boron. It can be derived from the boron concentration and the number of 10^{23} atoms per cm^3 that one boron atom is placed amongst 10^8 silicon atoms. From this density it can be concluded that the distance between two boron atoms is approximately $\sqrt[3]{10^8} \approx 1000$ lattice parameters. Hence the distance between a TDD centre and a boron atom is of several 100 of lattice parameters. The value implies that the donors and acceptors are too far separated from each other to form D-A-pairs and that a recombination of these is very unlikely. In silicon-carbide (SiC) it is known that the luminescence based on donor-acceptor recombination works efficiently for concentrations of $(10^{17}-10^{18})\text{cm}^{-3}$ of the donors and acceptors. From the comparison of these values it might be concluded that the concentra-

tion of the TDDs and B is too low to detect donor-acceptor-recombination-based EDEPR.

The samples prepared by Stich had higher concentrations of $1 \cdot 10^{16} \text{ cm}^{-3}$ of the donor B and acceptors ^{31}P and Cr. Thus the distance between the recombination partners is reduced and the recombination should be more effective. Indeed weak signals of the donors are detected with EDEPR but the observed magnitude of conductivity change is still by far too low compared to the predictions of the KSM and/or donor-acceptor recombination model.

Although great efforts have been undertaken to achieve a luminescence from crystalline silicon, no results from Photoluminescence-EPR (PL-EPR) based on donor-acceptor recombination have been published so far, even so samples with very high donor/acceptor concentrations up to 10^{19} cm^{-3} have been studied. This fact together with the findings presented above can be taken as an evidence that it is not a non-adequate concentration of the donors/acceptors that inhibits the detection of EDEPR.

In none of the EPR or EDEPR spectra presented in this chapter, resonances of a possibly present shallow dopant boron were detected. It is a generally accepted fact that B can not be observed in EPR due to a dynamic Jahn-Teller-distortion [Ludwig 1962].

6.3 On the impact of electron-irradiation on the EDEPR signal

In this work and the one by Stich [Stich 1997] several EDEPR experiments have been presented with samples that had been irradiated with electrons as one of the preparation steps. The consequence of the irradiation on the recorded EDEPR spectrum was very much surprising. In figure 6.3 an EDEPR spectrum of a ^{31}P -doped Cz-Si sample, which had been electron-irradiated and annealed at 460°C is shown.

Next to the resonance lines due to the radiation defect SL1 strong signals of both the ^{31}P and the TDDs are detected. It is apparent that the radiation defects provide an efficient recombination channel in which additional donors can be detected as well. A situation like this is known from optically detected magnetic resonance (ODMR) where the defect providing the recombination channel is opening a “shunt” channel [Spaeth 1992].

As the radiation defects seem to enhance the detection of EDEPR, the reason for their impact must be considered. In chapter 4 the radiation-induced vacancy-oxygen (V-O) centre has already been introduced. The neutral $(\text{V-O})^0$ state of the (V-O) centre is not

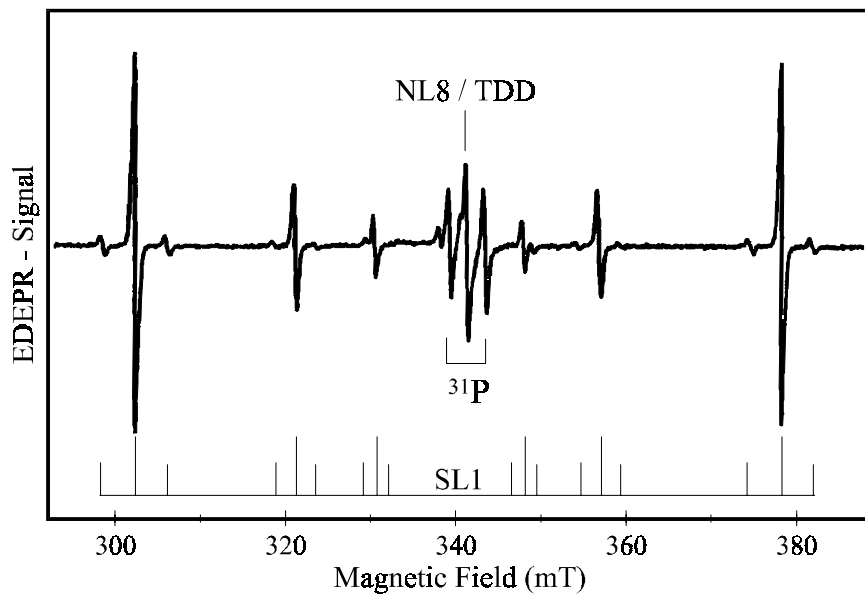


Fig. 6.3 EDEPR spectrum of a phosphorous-doped Cz-silicon sample after electron-irradiation and annealing at 460°C for 60min. The spectrum was recorded in X-band (9.54GHz) at 10K with white light illumination of the sample. A sample current of $5\mu\text{A}$ and magnetic field modulation with 5kHz was used.

paramagnetic. Since the defect can change to a paramagnetic state for two reasons, two different spectra of the (V-O) can be recorded. In the case of an additional electron being caught by the (V-O), the defect with $S=1/2$ is called A-centre and can be described as the negatively charged state $(\text{V-O})^-$ [Watkins 1961]. A second way to transform the (V-O) to the paramagnetic state is to create excess charge carriers by illumination of the sample with above-band-gap light. The charge carriers recombine via the neutral $(\text{V-O})^0$ to the neutral excited triplet state $(\text{V-O})^{0*}$ with an electron spin $S=1$. In this way the $(\text{V-O})^0$ acts as an recombination centre [Vlasenko 1984]. The $(\text{V-O})^{0*}$ can be detected in EPR and EDEPR and is called SL1-centre. The neutral triplet state $(\text{V-O})^{0*}$ with spin $S=1$ is metastable, since electronic transitions to the singlet ground state are spin-forbidden. The spin selection rule is 100% valid only as long as no additional orbital momenta are present in the sample. In reality, however, the orbital momenta of a paramagnetic defect are not completely quenched by the electrical crystal field of the lattice. This leads to a weakening of the selection rule and electron-hole recombinations via a transition of the excited triplet state $S=1$ to the singlet ground state $S=0$ are possible.

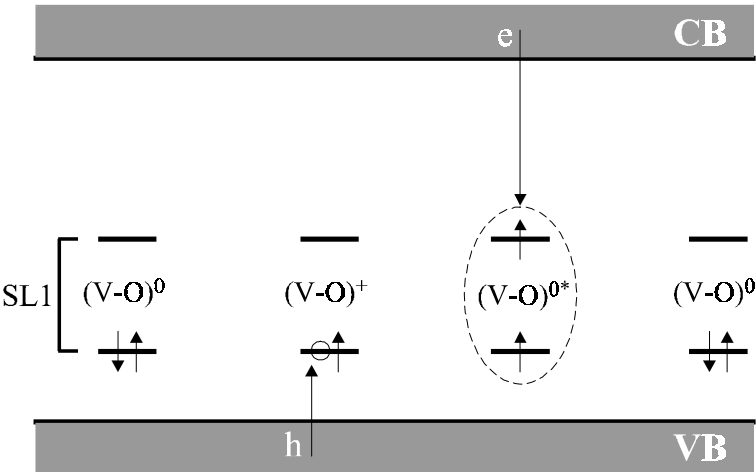


Fig. 6.4 Schematic illustration of an electron-hole recombination via the triplet state of the radiation-induced SL1 defect. $(V-O)^0$ is for the singlet ($S=0$) and $(V-O)^{0*}$ for the triplet state ($S=1$) of the SL1. The meaning of the arrows is explained in the text. Further, “e” is for electrons and “h” for holes.

It is assumed that the three m_s -states of the SL1-centre are equally occupied. Yet the recombination probability is different for the three states. To facilitate the following considerations it is assumed that the recombination probability R_0 of the triplet state $|m_s = 0\rangle$ significantly larger compared to the one of the other triplet states, $|m_s = +1\rangle$ and $|m_s = -1\rangle$, which are called R_{+1} and R_{-1} , respectively. Thus, $R_0 \gg R_{+1}, R_{-1}$ is assumed. Similar to a donor-acceptor pair recombination the different recombination probabilities of the m_s -states enables the electrical detection of EPR via a spin-dependent recombination. The triplet states of the recombination centre can be created by the capture of charge carriers (created by illumination) with a generation rate G , but can be destroyed with the dissociation rate W_D when emitting the charge carriers. Due to the assumed higher recombination probability R_0 of the triplet state $|m_s = 0\rangle$, a lower occupation density of this state compared to the $|m_s = \pm 1\rangle$ states is found. In the case of EPR transitions being induced according to the selection rule $\Delta m_s = \pm 1$, additional electron-hole pairs are transferred to the $|m_s = 0\rangle$ state, which leads to an increased number of recombining charge carriers. The increased recombination results in a conductivity decrease of the sample and can be detected in EDEPR. In the figures 6.4 and 6.5 the processes are illustrated.

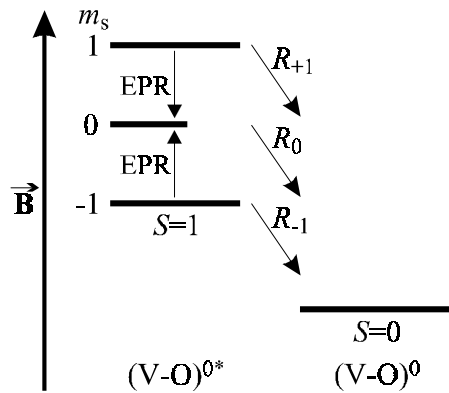


Fig. 6.5 Schematic illustration of the singlet, ($S=0$) and $(V-O)^0$, and the triplet state, ($S=1$) and $(V-O)^{0*}$, of the radiation-induced SL1 defect. The $R_{(-1,0,+1)}$ indicate the recombination probabilities from the excited triplet to the singlet ground state for the corresponding m_s .

For the model presented above it is assumed that the neutral singlet state $(V-O)^0$ captures a hole from the valence band and an electron from the conduction band. In the case that the spins of the hole and the electron are parallel, the triplet can be formed. However, if additional donors like ^{31}P or TDDs are present in the sample, the electron to form the triplet state of the SL1 can come from the donor level as well. It can be assumed that the $(V-O)^0$ captures a hole from the valence band and changes to paramagnetic state, similar to an acceptor.

In the case that the donor is in its neutral state due to the capture of an electron, both the hole from the $(V-O)^0$ state of the SL1 (the “acceptor”) and the electron from the donor can recombine via the triplet state if the spins are parallel. The spin orientation of the donor can be changed with the microwave with certain probability of the EPR transition W_{EPR} . With the requirement of parallel spins for the recombination a spin selection rule is found which explains the detection of the donors with EDEPR. Thus, the EDEPR detection of the additional donors can be explained by an “amplified” donor-acceptor pair recombination via the SL1-centre. The recombination of electrons and holes with the participation of additional donors is displayed schematically in figure 6.6.

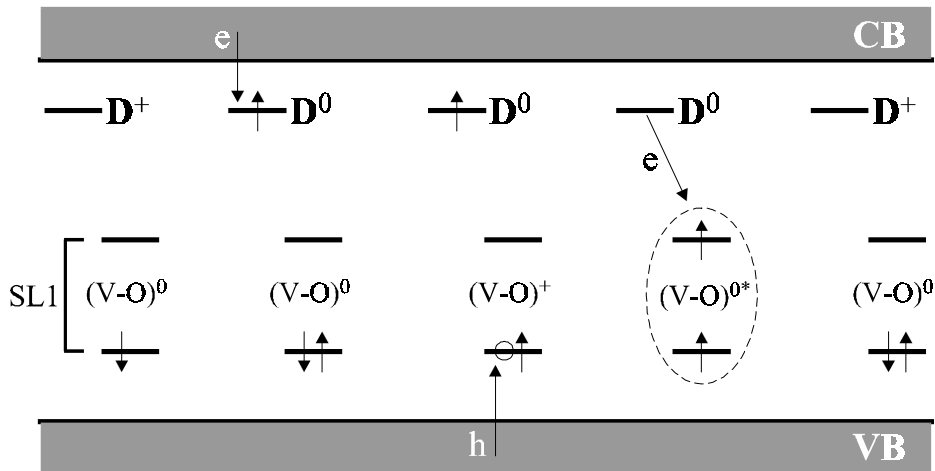


Fig. 6.6 Schematic illustration of an electron-hole recombination via the triplet state of the radiation-induced SL1 defect with an additional donor present in the sample. $(V-O)^0$ is for the singlet ($S=0$) and $(V-O)^{0*}$ for the triplet state ($S=1$). The meaning of the arrows is explained in the text. Further, “e” is for electrons and “h” for holes.

From the EDEPR investigation sample with radiation defects and TDDs it was measured that the samples conductivity decrease is about $\Delta\sigma/\sigma \approx 4 \cdot 10^{-3}$. The relative sign and the magnitude of the conductivity change are in good agreement with the values predicted by the modified donor-acceptor recombination mechanism. For a detailed explanation of the procedure to determine the values the reader is referred to Stich [Stich 1997]. Since the SL1 signals could be detected in EPR as well as in EDEPR an investigation of the power dependence of the signals was performed with both methods. The results are displayed in figure 6.7. The solid lines have been calculated according to the formulae presented in chapter 1, equations 1.15 and 1.18, which describe the characteristic EPR and EDEPR power dependencies. The latter is based on the D-A-recombination model. The amplitude and curve parameters used to calculate the EDEPR power dependence are $C=55$ and $T_R=0.025\text{s}$, respectively. Both parameters C and T_R are assembled of values of the generation rate (G), the dissociation rate (W_D) and the recombination probabilities R_i of the three m_s -states of the triplet. For a detailed explanation of the parameters C and T_R the reader is referred to Stich [Stich 1997]. A good agreement of the calculated curves with the experimental data is obvious. Seen

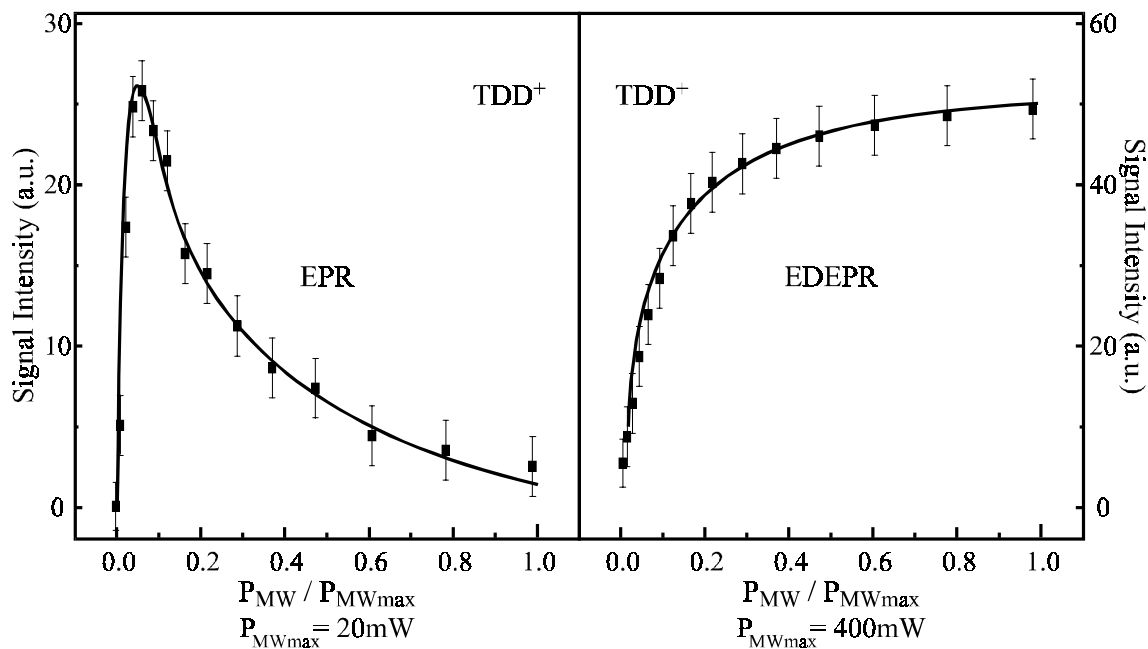


Fig. 6.7 Microwave power dependence of the TDD^+ signal of the sample presented in figure 6.3. The spectra were recorded at $T=10\text{K}$ in X-band for both EPR and EDEPR and the sample was illuminated each time. Magnetic field modulation was used with 100kHz and 5kHz , respectively. The solid lines are calculated according to equations 1.15 and 1.18, respectively.

together with the fact that both the sign and the magnitude of the observed conductivity change can be predicted correctly (explained in detail by [Stich 1997]), three arguments have been found to prove the proposed donor-acceptor recombination model to be correct.

6.4 On the mechanism responsible for the EDEPR detection of P_{ba} and P_{bb}

So far the mechanism responsible for the EDEPR detection of P_b -centres has been discussed controversially in the literature. In this study the EDEPR signals of P_{ba} and P_{bb} correspond to a decrease of the sample conductivity of approx. $\Delta\sigma/\sigma = 7 \cdot 10^{-4}$. The *decrease* of the conductivity is in agreement with both the Lépine-model and the donor-acceptor (D-A)-pair recombination mechanism by Stich [Stich 1997]. However, the magnitude of the conductivity change can only be explained by the latter model. For the

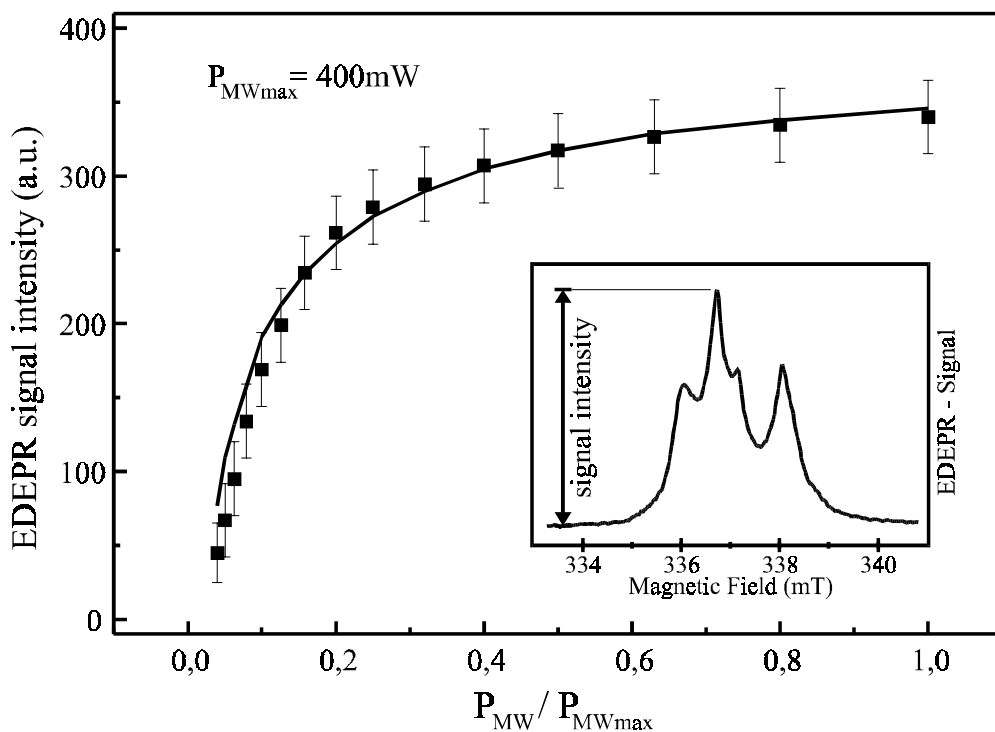


Fig. 6.8 Microwave power dependence of the P_{ba} EDEPR signal of a sample implanted with Mo with 7MeV. The sample is presented in detail in chapter figure 3. The spectra were recorded at $T=10\text{K}$ in X-band EDEPR and the sample was illuminated during the measurement. Magnetic field modulation was used with 100kHz and 5kHz, respectively. The solid lines are calculated according to equations 1.15 and 1.18, respectively.

D-A-recombination mechanism donors and acceptors have to be present in the sample. From the g -factor values obtained for P_{ba} and P_{bb} which are higher than that of the free electron (2.0023), it can be concluded that both P_{ba} and P_{bb} act as donors. As the samples were prepared from p-type (boron) FZ-silicon boron can be assumed to be the corresponding acceptor. Thus both partners for recombination are present in the sample.

A study of the power dependence reveals a further argument for the applicability of the D-A recombination mechanism. In figure 6.8 the observed signal intensities of the dominant line of the P_{ba} centre in dependence of the microwave power are shown. Additionally, a curve calculated with equation 1.15 is inserted in the figure. Equation 1.15 describes the power dependence of an EDEPR signal according the D-A mechanism. A good agreement of the curve with the experimental data points is found. The power de-

pendence has been calculated with values of $C=380$ (amplitude parameter) and $T_R=0.04\text{s}$ (curve parameter). The parameter C limits the maximum value of the calculation is therefore dependent on the signal intensity of the experiment. It is noted that the parameter TR , which is responsible for the shape of the curve, is very similar for the calculated dependencies in the figures 6.7 and 6.8. This indicates that the recombination efficiency for both defect systems the SL1-centre and the dangling bonds are similar. Hence, a further argument is found to support the assumption that a donor-acceptor recombination process is responsible for the EEPR detection of the dangling bonds.

From SDR measurements by Henderson et al. it was concluded that the dangling bonds on the trivalent Si-atoms act as centres for electron-hole recombination processes [Henderson 1984]. As the recombination results in a conductivity change in a surface-near region of the sample, the P_b centres can be detected with EDEPR. The suggested SDR mechanism is developed upon the Lépine model but lacks the correct evaluation of the magnitude of the SDR effect. The model predicts an SDR effect of $\Delta\sigma/\sigma = 10^{-6}$ [Lépine 1972] whereas Henderson et al. observed $\Delta\sigma/\sigma = 10^{-4}$. The authors could not explain the derivation of $\Delta\sigma/\sigma$ between experiment and theory.

With the predicted power dependence, the sign and the magnitude of the conductivity change, three arguments can be found to support the D-A-recombination model for the EDEPR detection of P_{ba} and P_{bb} . However, the validity of the mechanism remains somewhat speculative.

6.5 Peculiarities of EDEPR

Figure 6.9a depicts an EPR spectrum of an electron-irradiated p-type (boron-doped) Si-sample. The resonance line near 330mT ($g=2.0699$) represents an iron contamination of the sample, which is known to be an interstitial centre in silicon [Ludwig 1962]. It can be regarded as the dominant peak in the EPR spectra whereas it is not detectable in the EDEPR spectrum in figure 6.9b. The phenomenon can be explained by the fast recombination behaviour of the iron. Its recombination time is shorter compared to the spin-flip-rate for a spin-dependent transition. The available microwave power is not high enough to induce sufficient spin transitions during the recombination time.

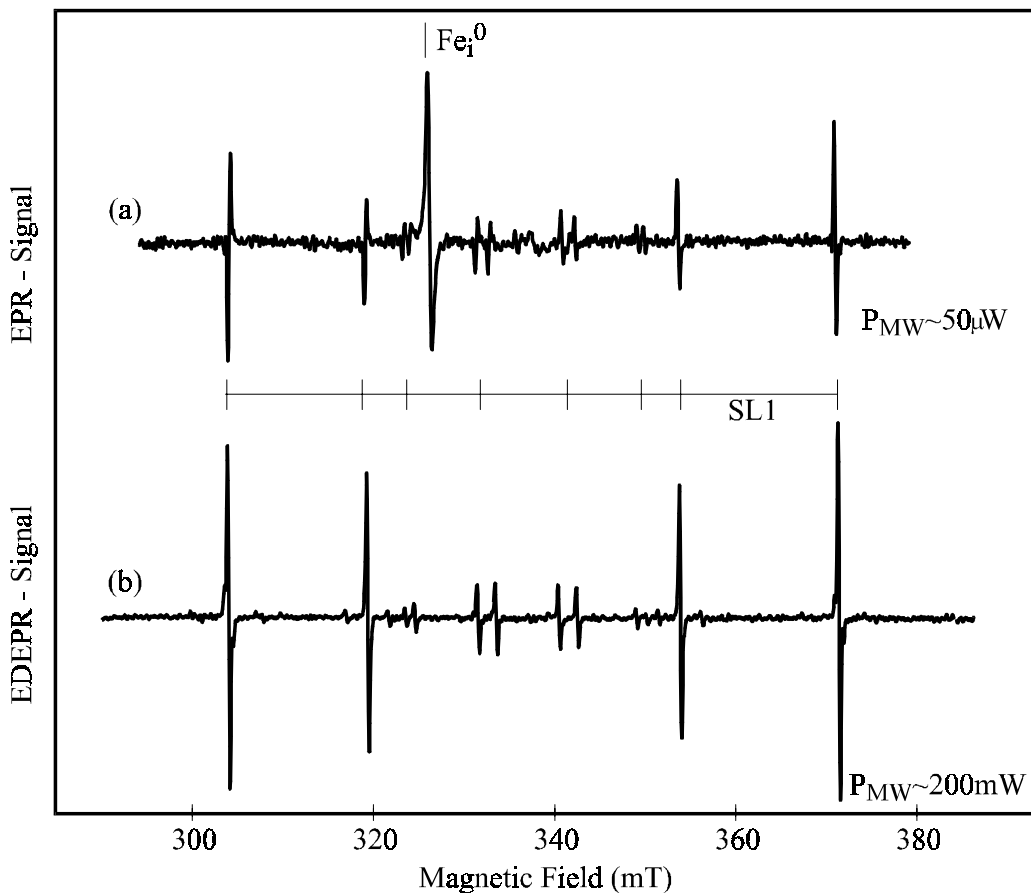


Fig. 6.9 EPR (a) and EDEPR (b) X-band spectrum of an electron irradiated p-type Si-sample with a strong Fe-contamination at $B \sim 330\text{mT}$. The Fe_i^0 -signal can be detected in EPR only.

As an essence of figure 6.9 it has to be kept in mind that the applicability of EDEPR has to be considered carefully. Defect centres detected in EPR may not be detectable in EDEPR as the mechanism for the two techniques appears to be a different one.

6.6 Conclusions

Summarising the results of this chapter it can be concluded that EDEPR is a qualitative method for the spectroscopy of point defects in semiconductors. For low defect concentrations and moderate donor-acceptor recombination times the methods provides spectral information and signal-to-noise ratios equal to those obtained by EPR. For selected

defect systems, EDEPR can be more sensitive with respect to the spin concentration per cm^3 by up to 4 orders of magnitude. The method is especially suitable for state-of-the-art thin layers and surface/interface defects. The EDEPR signals of point defects can be strongly increased by irradiation of the sample, as the radiation defects act as “shunts” which are known from ODMR. The recombination via the triplet state of the radiation-induced SL1-centre provides an efficient channel to detect additional shallow donors as well. It can be estimated that if the recombination time of a defect is comparable to the spin-lattice relaxation time a strong EDEPR signal should be observed.

Summary

The simultaneous detection of two dangling bond centres at and below a (100) Si/SiO₂ interface is reported for the first time. It is noted that the detected dangling bond centre P_{ba} is very similar to the P_{b0} defect reported in the literature. The P_{b0} centre is related to implantation damage below the Si/SiO₂ interface, leading to dangling bonds within the bulk material. Assuming a positive identification of P_{ba} with P_{b0} the result underlines the observation that the P_{b0} centre is generated by particle radiation. However, the identification of the P_{ba} centre found here with the known P_{b0} centre must remain somewhat uncertain.

The more anisotropic P_{bb} centre can be attributed to dangling bonds at the (100) Si/SiO₂ interface, occurring after annealing or low energy particle implantation. The Electrical Detection of Electron-Paramagnetic Resonance (EDEPR) signal of the P_{bb} centre can be increased by annealing in an oxygen containing atmosphere. The P_{bb} centre has been detected for the first time due to the increased sensitivity and low noise figure of low temperature EDEPR measurements.

Angular dependent EDEPR spectra of the dangling bond centres P_{ba} and P_{bb} have been recorded with improved spectral resolution and signal-to-noise ratio. The calculation of the angular dependence reveals a threefold symmetry of both defects. It can be concluded that the dangling bonds are aligned along a [111] direction in the crystal. The P_{ba} centres are thought to be due to silicon vacancies in the bulk created by radiation damage leaving the [111] dangling bond at one neighbour. The radiation damage is also believed to stabilise the vacancies against diffusion.

Shallow thermal donors which were prepared according to a recently developed procedure, comprising hydrogenation and electron-irradiation prior to annealing, were investigated with optical and magnetic resonance spectroscopy. Thus, three species (D1-D3) of these shallow donors can be created selectively by choosing a specific temperature in the range of (300–500)°C for the annealing step. The electronic properties of the D_n

were determined by means of Fourier Transform Infrared Absorption (FTIR) measurements. Evidence for an identification of D2 and D3 with two species of hydrogen-related shallow thermal donors (STD(H)) reported in the literature was found from the FTIR data. It is shown that the D1 is a precursor or the first species of the STD(H), undiscovered before.

EPR studies of the D_n centres revealed an isotropic ($g = 1.9987$) D1 signal upon rotation of the sample and orthorhombic-I symmetry for D2 centres ($g_{x,y,z} = 1.99952, 1.99722, 1.99982, \Delta g = \pm 0.00002$). The high accuracy of the g -values was obtained from EDEPR spectra recorded with V-band microwaves (72GHz). The g -values of the D2 are very similar to those of the oxygen precipitate NL10 presented in the literature and an identification of the D_n with the early species of the NL10 is suggested. Hyperfine (hf) lines of D1 and D2 due to an interaction of the unpaired electron with ^{29}Si nuclei (nuclear spin $I=1/2$) are observed. From the intensity ratio of the hf lines to the central line ($\approx 5\%$) the incorporation of one silicon atom in the defect structure of the D_n is concluded. Similar hf interactions are observed for NL10 defects with the incorporation of hydrogen, NL10(H), and aluminium, NL10(Al) for the first time.

The detection of the individual D_n centres with both methods FTIR and EPR provides a clear link between the STD(H) and the NL10(H) centres, reported in the literature separately from measurements of FTIR and EPR, respectively.

From an Electron-Nuclear Double Resonance (ENDOR) study of D1 centres prepared with hydrogen (deuterium), the incorporation of one hydrogen (deuterium) atom in the D1 defect is found. The angular dependence of the ENDOR spectra can be understood assuming a low symmetric (triclinic) hf tensor of the hydrogen atom. From the hf interactions observed in ENDOR a very low spin density at the site of the hydrogen is derived. A comparison with published data reveals that with the investigation of the D1 centre the first species of the STD(H) / NL10(H) has been studied for the first time.

An atomic model for the STD(H) centre had been presented previously on the basis of theoretical calculations. All experimental findings of this study support the suggested $(\text{C-H})_i\text{-Si}_s\text{-O}_{2i}$ structure. Furthermore, as an interstitial site for the Al-atom in NL10(Al) was suggested in a previous study, a similar atomic model with the $(\text{C-H})_i$ exchanged by an Al_i can be proposed for the NL10(Al).

Finally, the results of the EDEPR measurements carried out for this thesis have been summarised. A previously suggested donor-acceptor pair (DAP) recombination model for the mechanism of EDEPR was used to explain the recorded spectra. An investiga-

tion of the characteristic microwave power dependence of the EDEPR signals and both the sign and the magnitude of the conductivity change support the assumption. Further, indications were searched for to explain an amplification of EDEPR signals after irradiation of silicon samples with electrons. It is concluded that by the creation of the radiation-induced defect SL1, which appears upon illumination of the sample, an efficient recombination channel is provided via the triplet state of the SL1. This recombination channel can be “used” similar to a “shunt” known from Optically Detected Magnetic Resonance by other defects in the sample and their EDEPR signal can be significantly increased.

Further it is shown that a variation of the modulation techniques for the detection of EDEPR can improve both the signal-to-noise ratio of the detected signals and the spectral resolution in the case of several overlapping resonance lines. The spectral resolution of EDEPR was further enhanced by the use of high microwave frequencies in a modified high-field spectrometer. EDEPR measurements with frequencies as high as 72GHz are reported for the first time.

References

- [Abragam 1986] A. Abragam and B. Bleaney, *Electron Paramagnetic Resonance of Transition Ions* (Dover Publications, New York, 1986)
- [Alonso 1988] M. Alonso and E.J. Finn, *Quantenphysik, Addison-Wesley, (Deutschland) GmbH*, 1988
- [Ammerlaan 1996] C. A. J. Ammerlaan, I. S. Zevenbergen, Yu. V. Martinov and T. Gregorkiewicz, in *Early Stages of Oxygen Precipitation in Silicon*, Edited by R. Jones, NATO ASI Series, High Technology, Kluwer Academic Publishers, Dordrecht, **17**, 61 (1996)
- [Archer 1957] R. J. Archer, *J. Electrochem. Soc.*, **104**, 619 (1957)
- [Awadelkarim 1989] O. O. Awadelkarim, W.M. Chen, H. Weman, and B. Monemar, *Phys. Rev. B*, **41**, 1019 (1989)
- [Barklie 1994] R. C. Barklie, C. O’Raifeartaigh, L. Bradley and A. M. Hodge, *Mat. Sci. For.*, **143-147**, 195 (1994)
- [Bayerl 1998] M. W. Bayerl, M. S. Brandt, H. Angerer, O. Ambacher and M. Stutzmann, *phys. stat. sol. (b)*, **210**, 389 (1998)
- [Bean 1972] A. R. Bean and R. C. Newman, *J. Phys. Chem. Solids*, **33**, 255 (1972)
- [Bemski 1959] G. Bemski, *J. Appl. Phys.*, **30**, 1195 (1959)
- [Brower 1971] K. L. Brower, *Phys. Rev. (B)*, **4**, 1968 (1971)
- [Brower 1983] K. L. Brower, *J. Appl. Phys.*, **43**, 1111 (1983)
- [Brower 1986] K. L. Brower, *Phys. Rev. (B)*, **33**, 4471 (1986)

- [Brown 1988] A. R. Brown, M. Claybourn, R. Murray, P. S. Nandhra, R. C. Newman, and J. H. Tucker, *Semicond. Sci. Technol.*, **3**, 591 (1988)
- [Cantin 1995] J. L. Cantin, M. Schoisswohl, and H. J. van Bardeleben, *Phys. Rev. (B)*, **52**, R11599 (1995)
- [Caplan 1979] P. J. Caplan, E. H. Poindexter, B. E. Deal, and R. R. Razouk, *J. Appl. Phys.*, **50**, 5847 (1979)
- [Carrington 1967] A. Carrington and A. D. McLachlan, *Introduction to magnetic resonance*, Harper & Row, New York, 1967
- [Carlos 1997] W. E. Carlos and S. Nakamura, *Appl. Phys. Lett.*, **70** (15), 2019 (1997)
- [Chadi 1996] J. Chadi, *Phys. Rev. Lett.*, **77**, 861 (1996)
- [Chen 1991] W. M Chen, B. Monemar, and E. Janzén, *Phys. Rev. Lett.*, **67**, 1914 (1991)
- [Deák 1992] P. Deák, L. C. Snyder and J. W. Corbett, *Phys. Rev. B*, **45**, 11612 (1992)
- [Dirksen 1999] R. Dirksen, T. Gregorkiewicz and C. A. J. Ammerlaan, *phys. stat. sol. (b)* **210**, 539 (1999)
- [Ewels 1996] C. P. Ewels, R. Jones, and S. Oberg, in: *Early Stages of Oxygen Precipitation in Silicon*, ed. R. Jones (Kluwer Academic Publishers, Dordrecht 1996; NATO ASI Series, 3.High Technology, Vol. 17), pp. 141-162
- [Feher 1959] G. Feher, *Phys. Rev.*, **114**, 1219 (1959)
- [Fuller 1955] C. S. Fuller, J. A. Ditzenberger, N. B. Hannay and E. Buehler, *Phys. Rev.*, **96**, 833 (1954) and *Acta. Met.*, **3**, 97 (1955)
- [Gao 2000] F. Gao and J. Weber, *Phys. Rev. B*, **63**, 054101 (2000)
- [Gaworowski 1985] P. Gaworowski and E. Hild, *phys. stat. sol. (a)*, **92**, 129 (1985)
- [Ghandhi 1983] S. K. Ghandhi, *VLSI Fabrication Principles, Silicon and Gallium Arsenide*, Wiley, 25 (1983)

- [Götz 1992] W. Götz, G. Pensl and W. Zulehner, *Phys. Rev. B.*, **46**, 4312 (1992)
- [Götz 1998] W. Götz, G. Pensl, W. Zulehner and S. A. McQuaid, *J. Appl. Phys.*, **84**, 3561 (1998)
- [Grasa-Molina 2000] M.-I. Grasa-Molina, *Doctoral thesis, University of Paderborn* (2000)
- [Gregorkiewicz 1987] T. Gregorkiewicz, D. A. van Wezep, H. H. P. Th. Bekman and C. A. J. Ammerlaan, *Phys. Rev. B*, **35**, 3870 (1987)
- [Gregorkiewicz 1988] T. Gregorkiewicz, H. H. P. Th. Bekman and C. A. J. Ammerlaan, *Phys. Rev. B*, **38**, 3998 (1988)
- [Greulich -Weber 1995] S. Greulich-Weber, B. Stich, J.-M. Spaeth, *Mat. Sci. Forum*, **196-201** 1509 (1995)
- [Hall 1952] R. N. Hall, *Phys. Rev.*, **87**, 387 (1952)
- [Hallberg 1996] T. Hallberg and J. L. Lindström, *Appl. Phys. Lett.*, **68**, 3458 (1996)
- [Hartung 1994] J. Hartung and J. Weber, *Phys. Rev. B*, **48**, 14161 (1994)
- [Hatakeyama 1997] H. Hatakeyama and M. Suezawa, *J. Appl. Phys.*, **82**, 4945 (1997)
- [Hellwege 1974] K. H. Hellwege, *Einführung in die Physik der Atome*, Springer Verlag, Heidelberg (1974)
- [Henderson 1984] B. Henderson, *J. Appl. Phys.*, **44**, 228 (1984)
- [Henderson 1989] B. Henderson, M. Pepper, and R. L. Vranch, *Semicond. Sci. Technol.*, **4**, 1045 (1989)
- [Hölzlein 1984] K. Hölzlein, G. Pensl, and M. Schulz, *Appl. Phys. A*, **34**, 155 (1984)
- [Honig 1966] A. Honig, *Phys. Rev. Lett.*, **17**, 186 (1966)
- [Hrostowski 1960] H. J. Hrostowski and B. J. Adler, *J. Chem. Phys.*, **33**, 980 (1960)
- [Jones 2000] *private communications*
- [Kaiser 1957] W. Kaiser, P. H. Keck and C. F. Lange, *Phys. Rev.*, **101**, 1264 (1956)

- [Kaiser 1957] W. Kaiser and P. H. Keck, *J. Appl. Phys.*, **28**, 882 (1957)
- [Kaplan 1978] D. Kaplan, I. Solomon and N. F. Mott, *J. Phys. (Paris)*, **39** L51 (1978)
- [Kuzmany 1989] H. Kuzmany, ‘*Festkörperspektroskopie: Eine Einführung*’ *Springer-Verlag*, (1989)
- [Langhanki 1996] B. Langhanki, *Diploma thesis, University of Paderborn* (1996)
- [Lenahan 1982] P. M. Lenahan and P. V. Dressendorfer, *Appl. Phys. Lett.*, **41**, 542 (1982)
- [Lépine 1970] D. J. Lépine and J. J. Prejean, *Proc. of the 9. ICPS, Boston*, 805 (1970)
- [Lépine 1972] D. J. Lépine, *Phys. Rev. B*, **6**, 436 (1972)
- [Ludwig 1962] G. W. Ludwig and H. H. Woodbury, *Sol. Stat. Phys.*, **13**, 223 (1962)
- [Maier 1996] A. Maier, A. Grupp, M. Mehring, *Sol. Stat. Comm.*, **99** (9), 623 (1996)
- [Mao 1993] J. C. Mao, Y. Q. Jia, F. S. Fu, E. Wu, B. R. Zhang, L. Z. Zhang, and G. G. Qin, *Appl. Phys. Lett.*, **62**, 1408 (1993)
- [Markevich 1994] V. P. Markevich, M. Suezawa, K. Sumino and L. I. Murin, *J. Appl. Phys.*, **76**, 7347 (1994)
- [Markevich 1996] V. P. Markevich, I. F. Medvedeva, and L. I. Murin, in: *Early Stages of Oxygen Precipitation in Silicon*, ed. R. Jones (Kluwer Academic Publishers, Dordrecht 1996; NATO ASI Series, 3.High Technology, Vol. 17), pp. 103-122
- [Markevich 1997] V. P. Markevich, T. Mcchedlidze, and M. Suezawa, *Phys. Rev.B*, **56**, R12695 (1997)
- [Markevich 1998] V. P. Markevich, T. Mcchedlidze, M. Suezawa, and L. I. Murin, *phys. stat. sol.(b)*, **210**, 545 (1998)
- [Martynov 1995] Yu. V. Martynov, T. Gregorkiewicz, and C. A. J. Ammerlaan, *Phys. Rev. Lett.*, **74**, 2030 (1995)
- [Maxwell 1966] R. Maxwell and A. Honig, *Phys. Rev. Lett.*, **17**, 188 (1966)

- [McQuaid 1994] S. A. McQuaid, R. C. Newman and E. C. Lightowlers, *Semicond. Sci. Technol.*, **9**, 1736 (1994)
- [Medrano 1984] C. P. Medrano, H. S. Murrieta, and J. O. Rubio, *Journal of Luminescence* **29**, 223 (1984)
- [Meilwes 1993] N. Meilwes, *Doctoral thesis, University of Paderborn* (1993)
- [Mendz 1980] G. Mendz and D. Haneman, *Sol. Stat. Comm.*, **33**, 657 (1980)
- [Mendz 1981] G. Mendz and D. Haneman, *Appl. Phys. A*, **26**, 87 (1981)
- [Michel 1989] J. Michel, J. R. Niklas, and J.-M. Spaeth, *Phys Rev. B*, **40** 1732 (1989)
- [Mima 1980] L. S. Mima, V. I. Strikha and O. V. Tretyak, *Sov. Phys. Semicond.*, **14**, 1328 (1980)
- [Morton 1977] J. R. Morton and K. F. Preston, *Journal of magnetic Resonance*, **30**, 577 (1977)
- [Muller 1978] S. H. Muller, M. Sprenger, E. G. Sievert, and C.A.J. Ammerlaan, *Solid State Comm.* **25**, 987 (1978)
- [Munoz 1975] E. P. Munoz, J. O. Rubio, H. S. Murrieta, G. S. Aguilar, and J. O. Boldu, *J. Chem. Phys.* **62**, 3416 (1975)
- [Murin 1998] L. I.Murin, T. Hallberg, V. P. Markevich, and J. L. Lindstrom, *Physical Review Letters*, **80**, 93 (1998)
- [Navarro 1986] H. Navarro, J. Griffin, J. Weber, and L. Genzel, *Sol. Stat.Comm.*, **58**, 151 (1986)
- [Newman 1990] R. C. Newman, in: *Proc. of the 20th Int. Conf. on the Physics of Semiconductors* Vol.1, ed. E.M. Anastassakis and J. D. Joannopoulos (World Scientific, Singapore, 1990) p. 525
- [Newman 1996] R. C. Newman, J. H. Tucker, N. G. Semaltianos, E. C. Lightowlers, T. Gregorkiewicz, I. S. Zevenbergen and C. J. Ammerlaan, *Phys. Rev. B*, **54**, R6803 (1996)
- [Newman 1998] R. C. Newman, M. J. Ashwin, R. E. Pritchard, and J. H.Tucker, *phys. stat. sol. (b)*, **210**, 519 (1998)
- [Pajot 1967] P. Pajot and J. P. Deltour, *Infra-red Phys.*, **7**, 195 (1967)

- [Poindexter 1978] E. H. Poindexter, E. R. Ahlstrom, and P. J. Caplan, *The Physics of SiO₂ and its Interfaces*, 227, edited by S. T. Pantelides (Pergamon, New York, 1978)
- [Poindexter 1981] E. H. Poindexter, P. J. Caplan, B. E. Deal, and R. R. Razouk, *J. Appl. Phys.*, **52**, 879 (1981)
- [Poindexter 1983] E. H. Poindexter and P. J. Caplan, *Prog. Surf. Sci.*, **14**, 210 (1983)
- [Poole 1983] C. P. Poole, Jr., *Electron Spin Resonance*, 2nd ed., Dover ed., Wiley-Interscience Publication, New York, 1983
- [Pritchard 1995] E. Pritchard, S. A. McQuaid, L. Hart, R. C. Newman, J. Makinen, H. J. von Bardeleben, and M. Missous, *Journal of Applied Physics*, **78**, 2411 (1995)
- [Rohatgi 1980] A. Rohatgi, R. H. Hopkins, J. R. Davis, R. B. Campbell, and H. C. Mollenkopf, *Solid-State Electronics*, **23**, 1185 (1980)
- [Schmidt 1966] J. Schmidt and I. Solomon, C. R. Acad. Sci. Paris, **t.263**, 169-172 (1966)
- [Schockley 1952] W. Schockley and W. T. Read Jr., *Phys. Rev.*, **87 (5)**, 835 (1952)
- [Seidel 1961] H. Seidel, *Z. Phys.* **165**, 239 (1961)
- [Series 1982] R. W. Series and K. G. Barracough, *J. Cryst. Growth*, **60** ,212 (1982)
- [Sieverts 1983] E. G. Sieverts, *Phys. Stat. Sol. (b)*, **120**, 11 (1983)
- [Slichter 1989] C. P. Slichter, *Principles of Magnetic Resonance*, Springer Series in Solid State Sciences **1**, 3rd Edition (Springer, Berlin, 1989)
- [Solomon 1976] I. Solomon, *Sol. Stat. Comm.*, **20**, 215-217 (1976)
- [Spaeth 1992] J.-M. Spaeth, J. R. Niklas, and B. H. Bartram, *Structural Analysis of Point Defects in Solids*, Springer Series in Solid State Sciences **43** (Springer, Berlin, 1992)
- [Spaeth 1996] M.-J. Spaeth, in *Early Stages of Oxygen Precipitation in Silicon*, Edited by R. Jones, NATO ASI Series, High Technology, Kluwer Academic Publishers, Dordrecht, **17**, 83 (1996)

- [Stathis 1991] J. H. Stathis and L. Dori, *Appl. Phys. Lett.*, **58**, 1641 (1991)
- [Stathis 1994] J. H. Stathis and E. Cartier, *Phys. Rev. Lett.*, **72**, 2745 (1994)
- [Stesmans 1986] A. Stesmans, *Appl. Phys. Lett.*, **62**, 1408 (1986)
- [Stich 1993] B. Stich, S. Greulich-Weber, J.-M. Spaeth, and H. Overhof, *Semicond. Sci. Technol.*, **8**, 1385 (1993)
- [Stich 1995] B. Stich, S. Greulich-Weber, and J.-M. Spaeth, *J. Appl. Phys.*, **77**, 1546 (1995)
- [Stich 1997] B. Stich, *Doctoral thesis, University of Paderborn* (1997)
- [Suezawa 1983] M. Suezawa, K. Sumino, and M. Iwaizumi, *J. Appl. Phys.*, **54**, 6594 (1983)
- [Szkielko 1978] W. Szkielko, *phys. stat. sol. (b)*, **90**, K81 (1978)
- [Tobin 1985] S. P. Tobin, A. C. Greenwald, R. G. Wolfson, D. L. Meier, and P. J. Drevinsky, *Mater. Res. Soc. Symp. Proc.*, **36**, 4 (1985)
- [van Kemp 1986] R. van Kemp, E.G. Sieverts, and C.A.J. Ammerlaan, 14th ICDS, Paris, France, Materials Science Forum, vol.10-12, pt.3, 1986, pp.875-80. Switzerland
- [Vlasenko 1984] L. S. Vlasenko, I. M. Zaritskii, A. A. Konchitis and B. D. Shanina, *Sov. Phys. Solid State*, **26** (1), 66 (1984)
- [Vlasenko 1986] L. S. Vlasenko and V. A. Khramtsov, *Sov. Phys. Semicond.*, **20** (6), 688 (1986)
- [Vranch 1988] R. L. Vranch, B. Henderson, and M. Pepper, *Appl. Phys. Lett.*, **52**, 1161 (1988)
- [Wagner 1989] P. Wagner and J. Hage, *Appl. Phys. A.*, **49**, 123 (1989)
- [Watkins 1959] G. D. Watkins, J. W. Corbett and R. M. Walker, *J. Appl. Phys.*, **30**, 1198 (1959)
- [Watkins 1965] G. D. Watkins, *Radiation Damage in Semiconductors*, 97, Editor P. Purcel, Dunod, Paris (1965)
- [Watkins 1974] G. D. Watkins, *Lattice defects in Semiconductors*, 1974, edited by F. A. Huntley, IOP Conference Proceedings No. 23, Institute of Physics, Bristol (1973)

- [Weber 1996] J. Weber and D. I. Bohne, in: *Early Stages of Oxygen Precipitation in Silicon*, ed. R. Jones (Kluwer Academic Publishers, Dordrecht 1996; NATO ASI Series, 3.High Technology, Vol. 17), pp. 123-140
- [White 1977] R. M. White and J. F. Goujet, *Phys. Rev. B*, **16**, 3596 (1977)
- [Wörner 1985] R. Wörner and O. F. Schirmer, *Phys. Rev. B*, **34**, 1381 (1985)
- [Wojsinski 1976] T. Wojsinski, T. Figielski and A. Makosa, *phys. stat. sol.(a)*, **37**, K57 (1976)
- [Wojsinski 1977] T. Wojsinski and T. Figielski, *phys. stat. sol.(b)*, **83**, 93 (1977)

Mein besonderer Dank gilt Herrn Prof. Dr. J.-M. Spaeth für die freundliche Aufnahme in seine Arbeitsgruppe. Kritische Diskussionen waren stets ergebnisorientiert und brachten die entscheidenden Hinweise zur Deutung der experimentellen Daten.

Herrn PD Dr. S. Greulich-Weber danke ich für die Einführung in die magnetischen Resonanzmethoden und seine stete Hilfe bei experimentellen Problemen aller Art.

Ich danke Herrn Dr. habil. S. Schweizer für seine Hilfe, die auch über fachliche Probleme hinaus stets freundschaftlich war.

Ich danke allen, die für eine vortreffliche Infrastruktur im Fachbereich sorgten,
für das Rechnernetz Herrn Dr. Ch. Hoentzschen,
für die mechanische Werkstatt Herrn F. Risse,
für die Versorgung mit Kältemitteln Herrn Dr. F. Lohse und Herrn J. Pauli und
für das Kristallzuchtlabor mit Herrn D. Niggemeier und Herrn R. Winterberg.

Dank gilt allen Mitgliedern des Institutes für die gute Zusammenarbeit und ein hervorragendes Arbeitsklima.